Delivering antimicrobial peptides through polymer complexation – creating efficient nanocarriers to fight resistant bacteria

Lelaw Jalal Ali

Thesis for the Master´s Degree in chemistry
60 study points

Department of Chemistry
Faculty of Mathematics and Natural Sciences

UNIVERSITY OF OSLO

Spring 2022

Delivering antimicrobial peptides through polymer complexation – creating efficient nanocarriers to fight resistant bacteria

Master´s thesis in Chemistry

Lelaw Jalal Ali

© Lelaw Jalal Ali

2022

Delivering antimicrobial peptides through polymer complexation – creating efficient nanocarriers to fight resistant bacteria

Lelaw Jalal Ali

http://www.duo.uio.no/

Printed at Reprosentralen, Universitetet i Oslo

Preface

First and foremost, I would like to begin this preface by expressing my deepest gratitude and love to my father, Jalal Ali Aziz, who passed away on 04.01.2023. It is with a heavy heart and immense appreciation that I dedicate this thesis to him. My father's unwavering support and belief in my abilities have been instrumental in making this journey possible. His encouragement and sacrifices have shaped me into the person I am today, and I will forever cherish the memories and lessons he shared with me. Dad, I love you, and I am eternally grateful for everything you have done for me.

The work presented in this thesis has been carried out at the Department of Chemistry, University of Oslo under the supervision of Prof. Reidar Lund. The work presented in this thesis was a collaborative effort between Roskilde University and the University of Oslo. Where the last part of the project was conducted in Dr. Håvard Jenssen's lab at Roskilde University, Department of Science and Environment/ Center for Molecular Interactions. Additionally, a cooperative collaboration was done with Harald Røsand Moe from the Department of Bioanalytical Chemistry, University of Oslo.

After many difficult years at the university and many months of intensive effort on this project, I want to dedicate this page to those who have been a source of encouragement along the road. First and foremost, I would like to thank my thesis advisor, Prof. Reidar Lund, for his enormous support and guidance throughout this work and for giving me the freedom to pursue my scientific ambitions. During my thesis, I have been able to visit large-scale research facilities for X-rays in Grenoble and gotten the chance to conduct further research work at Roskilde University. These experiences have been invaluable to me and would not have been possible without you. You have always encouraged me and supported me, and the door to your office was always open whenever I ran into a difficult spot or had a question about my research. I am truly grateful to have had you as my supervisor.

Additionally, I would like to express my heartfelt gratitude to Prof. Håvard Jenssen for taking me in so warmly during my stay at Roskilde University. I truly appreciate this great opportunity,

where I had the chance to evolve as a scientist and meet many aspiring scientists from your group. It has been really great to get to know you.

Furthermore, I want to thank all my fellow students at the group for Soft Matter whose emotional and social support I couldn't have been without. A special thank you to PhD candidate Thomas Voogelaar for giving me an amount of support at the finish line of my thesis. I would also like to thank PhD candidate Victoria Ariel Bjørnestad who was able to provide me with extensive help with difficult SAXS data during my work and that was a great companion during our trip to ESRF in Grenoble.

Finally, I must express my very profound gratitude to my parents and to my siblings for providing me with unfailing support and continuous encouragement throughout my years of study and through the process of researching and writing this thesis.

Thank you for everything!

Abstract

Because of the limited number of antibiotics available and the similarities in their activity and mode of action, considerable nonclinical and clinical research is being spent in the discovery and development of new and non-conventional anti-infective medicines. Interestingly, the polymyxins have piqued the interest of researchers as promising new antibiotics to control infectious pathogens arising from MDR Gram-negative bacteria [1, 2]. In reality, only a few polymyxins have been utilized in "real-world" application, with the most clinically relevant being colistin. While efficacious in the clinical setting, there were subsequent studies that reported severe toxicities with use of colistin as a therapeutic option, especially nephrotoxicity and neurotoxicity as uncommon adverse event

The disadvantages associated with colistin can be mitigated by encapsulating the peptide in nanocarriers like block copolymer micelles. However, there is a scarcity when it comes to core-shell assemblies by peptide-polymer conjugates, and in particular the assemblies of peptides assembled with neutral-polyanion DHBC. Moreover, the relation between the release of the peptide and the nanocarrier structure and dynamics is lacking. Therefore, the overall aim of the research presented in this thesis was to develop novel nanomedicines based on the peptide colistin. This includes a systematically investigation of the phase diagram of colistin/PEO-b-PMAA mixtures as a function of pH, charge ratio and total concentration. The overall goal will be to find optimal conditions under which stable core-shell colistin-polymer complexes are formed. In the second part of the project, different formulations of colistin-polymer nanoparticles where investigated in vitro for their bacterial killing activity against few multidrug-resistant Gram-negative bacteria isolates, which were compared to that of free colistin.

Table of content

1 Introduction

Because of the limited number of antibiotics available and the similarities in their activity and mode of action, considerable nonclinical and clinical research is being spent in the discovery and development of new and non-conventional anti-infective medicines. Interestingly, the polymyxins have piqued the interest of researchers as promising new antibiotics to control infectious pathogens arising from MDR Gram-negative bacteria [1, 2]. In reality, only a few polymyxins have been utilized in “real-world” application, with the most clinically relevant being colistin. Colistin, also known as polymyxin E, is one important member of the polymyxin family, and is a cationic peptide-based antibiotic produced as a secondary metabolite of the Gram-positive soil bacterium Paenibacillus polymyxa subsp. Colistinus. Colistin was first identified in 1947 for its in vitro activity against several MDR gram-negative pathogens, in particular Klebsiella pneumoniae, Acinetobacter baumannii and Pseudomonas aeruginosa[3]. Later on, colistin was used in clinical settings as an antimicrobial agent against Gram-negative bacteria due to its efficient bactericidal activity for treatment of various types of infections, including infectious diarrhoea and urinary tract infections. While efficacious in the clinical setting, there were subsequent studies that reported severe toxicities with use of colistin as a therapeutic option, especially nephrotoxicity and neurotoxicity as uncommon adverse event [4, 5]. In the 1970s, colistin ended up with being phased out in favor of newer agents that were thought to be 'less toxic' at the time. As a result, colistin has been consigned to the status of a last-resort antibiotic, to be used only when all other therapeutic alternatives have failed. However, in the 1990s clinicians was forced to reintroduce the clinical use of colistin due to an escalating prevalence of infections caused by MDR Gram-negative bacteria P. aeruginosa, A. baumannii and Klebsiella pneumoniae which are showing resistance to most commercially available antibiotics [6, 7]. Management of these “super bugs” with newer antibiotics is not a viable option as few antibiotics are in the drug development pipeline as a consequence of industry consolidation, challenging regulatory guidelines and increase in research and development (R&D) costs [8, 9]. This has been highlighted in the USA over past decade showing a drastic decrease in newly approved antibiotics by the Food and Drug Administration (FDA) regulatory body; as of 2020, there were only three new antibiotic agents that were approved for clinical use [10]. Therefore, as mentioned previously, clinicians are having to reappraise the clinical value of colistin which maintains significant in vitro activity against these MDR Gram-negative bacteria.

However, this does not change the reality that there are still biological hurdles to overcome before colistin can be used in clinical settings. To ameliorate those issues, there has been a considerable interest in developing topical delivery systems for colistin, where a targeted delivery to the site of infection would enable colistin to achieve a higher local concentration, hence increasing its antibacterial effectiveness. Additionally, this method of delivery avoids "first-pass" metabolism, which may help reduce the toxic side effects associated with systemic administration of the drug. These novel therapeutic approaches to improve the drugability of colistin will be discussed further in this thesis.

1.1.1 Chemical structure of polymyxins

Polymyxins are a group of polypeptide antibiotics that includes several chemically different compounds (polymyxins A-E, M, etc.). Of these, only polymyxin B and polymyxin E (also known as colistin sulfate) are used in clinical settings [11]. Generally, the polymyxins have a fairly similar structure, consisting of a cyclic heptapeptide ring with a linear tripeptide sidechain that is connected to an N-terminal fatty acid tail, this is also shown in Figure 1 [11, 12]. However, the specific composition of amino acids in the peptide portion and fatty acid group can vary. From the ten amino acids presents, the ones in position 3, 6 and 7 may vary. While the fatty acid group can range from seven to nine carbon atoms in length, they can also be methylated, hydroxylated, or sulphonated [13]. Despite the fact that the specific composition of each polymyxin varies, the amphipathic structure of polymyxins is maintained. All of the hydrophobic properties of polymyxins are conserved, including their hydrophobic properties in the fatty acid group and the hydrophobic characteristics of the variable amino acids in position 6 and 7. Polymyxin´s hydrophilic nature is due to the hydroxyl side-chains of L-Threonine (Thr) in position 2 and 10, and also the polar amine side-chains of L-2,4-diaminobutyric acid (Dab) groups in position 1, 3, 5, 8 and 9 [13]. The primary amines are crucial residues in polymyxin because they cause the net-charge of the polymyxin molecules to be positive at physiological pH. The hydrophobic and hydrophilic features of the polymyxin molecule allows the molecule to fold into an amphipathic form, which is important for the molecule´s mechanism of action.

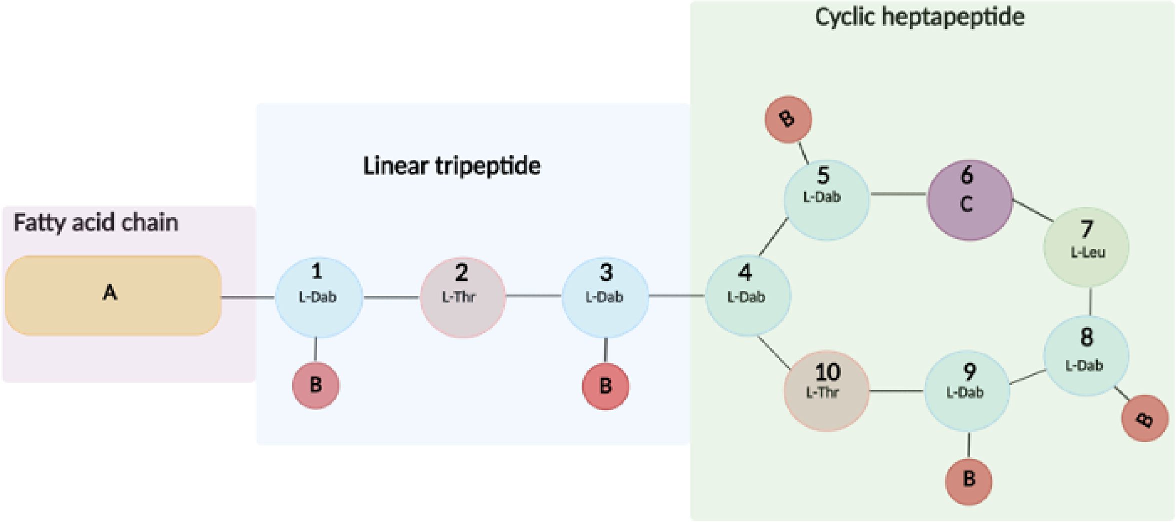

	Substance	Alteration
A	polymyxin B1 / colistin A (E1)	6-methyloctanoic acid (6-MOA)
	polymyxin B2 / colistin B (E2)	6-methylheptanoic acid (6-MHA)
B	polymyxin B and colistin	amino group (-NH_2)
	colistimethate (CMS)	NH-CH_2-SO_3H
C	polymyxin B	D-Phenylalanine
	colistin	D-Leucine

Figure 1: General polymyxin molecule composition. Polymyxins have a cyclic heptapeptide ring (amino acid 4-10) with a linear tripeptide sidechain (amino acid 1-3) that is connected to an N-terminal fatty acid tail. The main differences between the polymyxins are attributed to the different component of polymyxin B and colistin, and also another commercial available form of colistin, which is sodium colistin methanesulfonate (CMS). The differences are caused by the listed amino acid or side chain alternation (A-C). The abbreviations used in the illustration are as follows; L-Dab: 2,4-diaminobutyric acid, D-Phe: Phenylalanine, L-Thr: Threonine, D-Ser: Serine *This figure is created by the author of this document using BioRender.*

In terms of their primary sequences, colistin shares the same central structure as the other polymyxins. However, it is essential to note that colistin refers not to one singular structure but rather a set of structures. In total, colistin is recognized as a mixture of thirteen highly similar compounds, with only significant difference being the composition of amino acids and the fatty acid. Two of the major active components of colistin are colistin A (polymyxin E1) and colistin B (polymyxin E2), compromising approximately 85% of the total mixture. The only difference is on the N-terminal fatty acid group; colistin A is acylated by 6-methyl-octanoic acid (6-MOH) and colistin B is acylated by 6-methylheptanoic acid (6-MHA). As depicted in Figure 1, term A denotes the variation in fatty acid chain between the distinct components of. By virtue of the five L-Dab residues situated around the heptapeptide ring and on the tripeptide side chain, colistin is cationic at physiological pH due to protonation of these amino groups. Colistin is amphipathic due to the fatty acid chain and the five free γ-amino groups which gives colistin both hydrophobic and basic characteristic, respectively; this enables colistin to distribute into polar and non-polar environments in the body i.e., water, blood and eukaryotic, prokaryotic lipid membranes. Figure 2 shows a more thorough representation of the compound colistin A.

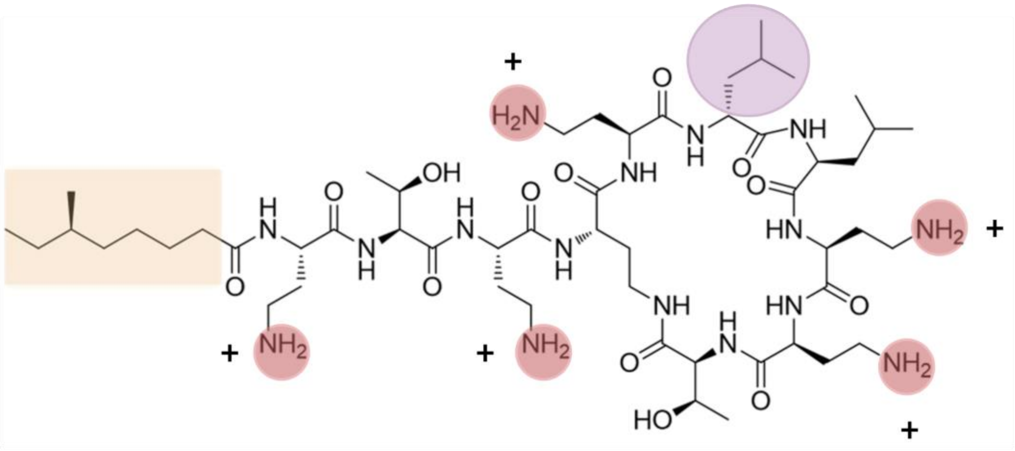

Colistin A

Figure 2: Chemical structure of Colistin A. Where the fatty acid tail is acylated with 6-MOH, and illustrated in the color orange. Position 6 that differ from polymyxin B, is highlighted in the color purple. Colistin also cationic at physiological pH with a net charge of +5. This figure is created by the author of this document using BioRender is based on information retrieved from [14].

The high prevalence of colistin-induced nephrotoxicity and neurotoxicity necessitated the introduction of the inactive prodrug colistin methanesulfonate sodium (CMS) into the market. Colistin is administered intravenously as the inactive prodrug CMS, which undergoes transformation to a variety of partially sulfomethylated derivatives before being converted to colistin, which is the entity that is responsible for the killing of bacteria [15]. CMS is formed when the free γ-amino groups of L-Dab residues in colistin are reacted with formaldehyde and sodium bisulfite, resulting in the attachment of a sulphomethyl group to the primary amines of colistin [16]. This is also highlighted under Figure 1 as term B. In comparison to colistin, the inclusion of sulphomethyl groups in CMS results in an anionic state at physiological pH. Several studies have discovered that polymyxin antibiotics lose their antimicrobial activity when more than one amino group has been subjected to the sulphomethylation procedure. Bergen et al. recently established that the formation of colistin following CMS administration is necessary for antimicrobial activity [17].

1.1.2 Mechanism of antimicrobial activity of colistin

While it is well established that colistin exhibits rapid in vitro bactericidal activity against major MDR gram-negative pathogens, nevertheless, the precise mechanism by which colistin exerts its antimicrobial activity is still being debated. The gram-negative bacteria consist of two layers of protection against the outside world: an outer cell membrane and an inner cell membrane (Figure 3). To kill the Gram-negative bacteria, colistin must punch holes in both of them. It was very soon established that the antibacterial properties colistin displayed originated from its ability to disrupt the outer membrane (OM) by selectively binding to the negatively charged lipid A portion of the lipopolysaccharide (LPS) on the surface of the Gram-negative bacteria, but it is unclear how this results in cell lysis and bacterial death. It is hypothesised that damage to the LPS monolayer enables colistin to traverse the OM via a process of 'self-promoted uptake', although this has not been demonstrated experimentally. It has been proposed that the surfactant activity of colistin conferred by the positively charged peptide ring and hydrophobic tail, is sufficient to compromise the phospholipid bilayer of the OM via a detergent-like effect.

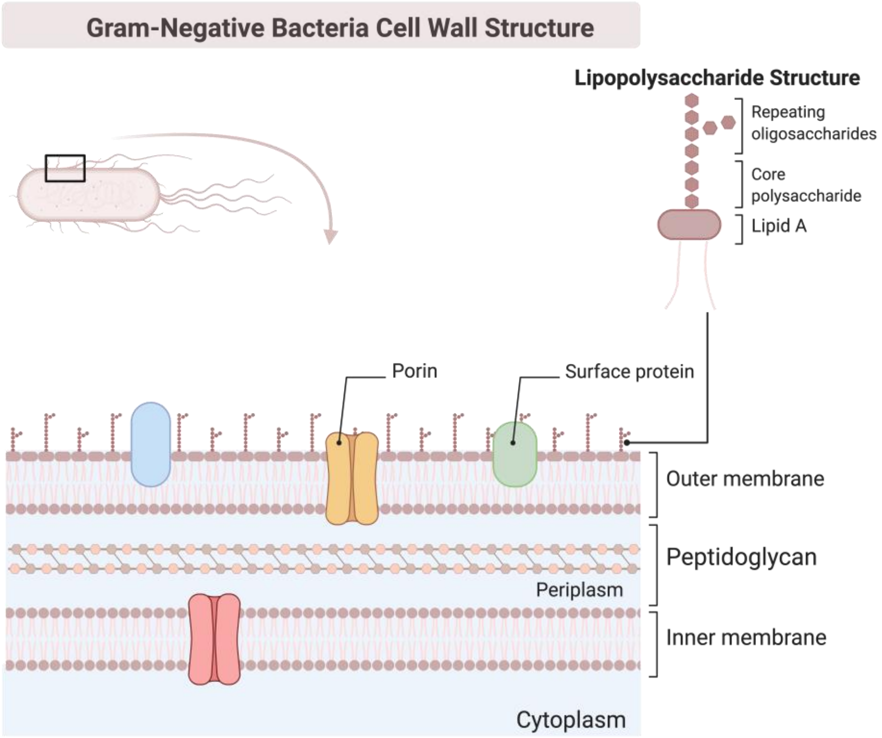

Figure 3: Illustration showing the structure of the Gram-negative bacteria membrane. The Gram-negative bacteria consist of two layers of protection: an outer cell membrane and an inner cell membrane. The outer membrane is composed of an inner phospholipid leaflet and an outside leaflet that contains LPS, lipoproteins, and integral outer membrane proteins. Where the LPS is made up of a repetitive polysaccharide O-antigen chain, an inner core of 2-keto-3-deoxyoctonoic acid (Kdo), and a conserved lipid A moiety. This figure is created by the author of this document using BioRender and is based on information retrieved from [18, 19].

Clausell published a paper in 2007 demonstrating the relevance of the lipopeptide's two hydrophobic domains (N-terminal acyl chain and D-Phe-Leu region), as well as the five positive charges of Dab in colistin via polymyxin B analogs. Polymyxin B and colistin are almost identical, with the exception of the amino acid at position 6 (see Figure 1), which is D-Phe in polymyxin B and D-Leu in colistin. It was argued in the article that a polymyxin B analog lacking an acyl tail exhibited no antimicrobial activity despite its ability to bind to LPS. In contrast, it was demonstrated that another polymyxin B analog containing D-Phe6-L-Dab7 instead of D-Phe6-Leu7 did not bind to the LPS, which was most likely caused by the hydrophobic domain being replaced by the L-Dab residue. These significant findings show that the hydrophobic domains of colistin, as well as the acyl tail and the D-Leu6-L-Leu7 region, are required for colistin to be able to disrupt the OM.

Once across the OM, colistin permeabilise the cytoplasmic membrane (CM), which is required for bacterial lysis and killing. However, the precise mechanism by which colistin damages the CM is unclear. The vesicle-vesicle contact pathway has been proposed as a possible explanation for the surfactant activity of colistin. This mechanism suggests that once colistin penetrates the OM, the hydrophobic fatty acyl tail and cationic L-Dab residues engage with the periplasm-facing leaflets of both the OM and the IM, promoting vesicle interaction between the two. It is anticipated that this interaction will promote phospholipid interchange between the membranes, resulting in a reduction in the specificity of the phospholipid composition. If this occurs, it has the potential to result in an osmotic imbalance, which can ultimately result in cell death.

An alternative mechanism by which colistin kills bacteria is through a mechanism called membrane lysis. According to this idea, once colistin enters the periplasmic region, it disrupts the IM's physical integrity by straddling the interface between the phospholipid head groups and fatty acyl chains (the region where the phospholipid head groups are attached to the fatty acyl chains), resulting in a decrease in IM thickness, cytoplasmic content leakage, and consequent cell death. However, to the best of our knowledge, this theory has not been explicitly established and does not explain colistin's inhibitory activity against Gram-positive bacteria which also has CM formed of a phospholipid bilayer.

Recently, another explanation of how colistin impacts the IM was proposed, and this theory is based on the lipid A biosynthesis pathway. Briefly stated, lipid A is generated in the cytoplasm from a precursor molecule known as UDP-N-acetyl-glucosamine, which goes through a series of sequential transformations before reaching its ultimate form, which is lipid A. In the following step, the core of LPS attaches to the final lipid A, then the MsbA transporter transports the entire lipid A-LPS core to the IM's outer leaflet. A simultaneous production of the O antigen occurs in the cytoplasm, which is then flipped to the outer leaflet of the IM, where it attaches to the lipid A-LPS core. The newly synthesized LPS, which is now on the periplasmic side, is transported across the periplasm and inserted into the outer leaflet of the OM by the Lpt (LPS transporter) complex. Sabnis et al. (2021) reasoned that, despite colistin's affinity for lipid A in the OM, it might also target lipid A in the IM prior to its transit to the OM. This assumption was supported by additional research that confirmed the high presence of lipid A in the IM and also established that the interaction between lipid A and colistin in the IM is required for colistin antimicrobial activity. With this theory in place, we can begin to understand why colistin is particularly successful against Gram-negative bacteria but ineffective against Gram-positive bacteria that lacks an outer membrane.

Beyond killing bacteria directly as antibiotics, colistin have also been linked to having other host defence effects that potentially are important for their therapeutic activity towards infectious diseases in patients. The release of LPS (also termed 'endotoxins') from Gram-negative bacterial cells stimulated a series of inflammatory responses that are a major contributing factor in the onset of bacterial infection. As noted above, colistin molecules have been shown to bind to LPS via a specific interaction with the phosphate groups on the lipid A region of the molecule. The binding of the colistin molecule to LPS neutralizes the endotoxic effects of LPS, thereby minimizing fever and inflammation associated with the onset of infections.

As discussed in this section, a variety of models for the antimicrobial mode of action for colistin have been proposed. Stating a universal mode of action hypothesis is therefore difficult and probably unrealistic. The effect of colistin seems to be highly complex where both membrane disruption and intracellular targets may play important roles in the full picture. However, while these alternative mechanisms of action are all considered, it is possible that alle these phenomena occur as downstream consequence of colistin-mediated CM disruption. As such, there is a need to further study the colistin-membrane interactions to provide the foundations for novel approaches to enhance therapeutic outcomes.

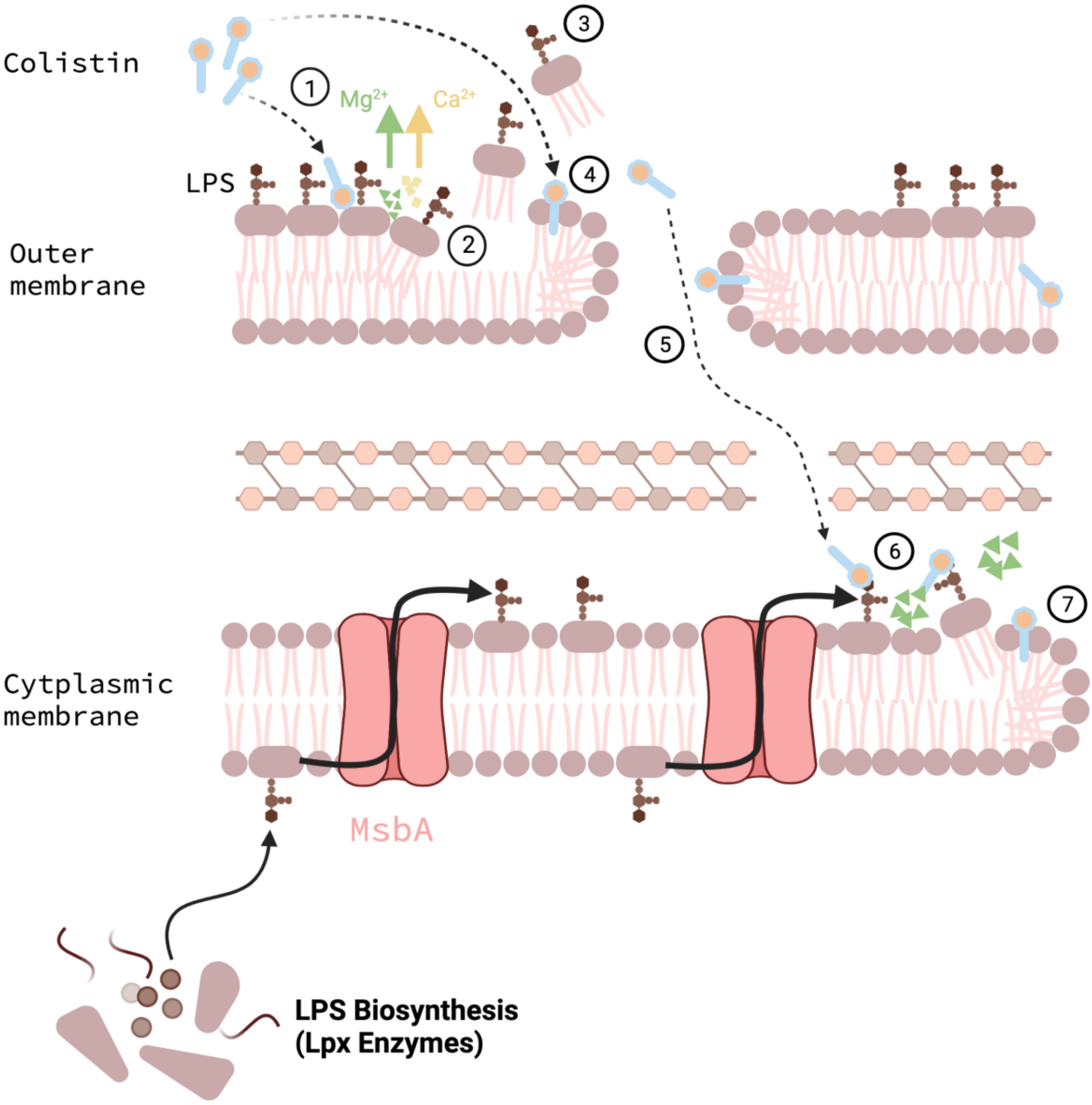

Figure 4: **Colistin kills gram-negative bacteria by disrupting the outer membrane of the bacterium by selectively targeting LPS**. The proposed mechanism of action for colistin is depicted in the following diagram: (1) Colistin binds to the LPS on the outer membrane, (2) where there is displacement between Mg2+ and Ca2+ and colistin, which leads to a destabilization of the outer membrane. (3) Because of the weakening of the intermolecular connections in the LPS, it will be able to break free from the leaflet's outer membrane. (4) The hydrophobic moites included in colistin will interact with the outer membrane, causing more harm. (5) Disruption in the membrane causes colistin to reach the periplasmic region and interacts with the LPS in the periplasmic membrane. (6) As with the outer membrane, colistin binds to the LPS, causing cations to be displaced, and disrupts the cytoplasmic membrane, (7) causing the membrane to become permeabilized and the contents of the cell to leak out, resulting in cell death. *This figure is created by the author of this document using BioRender and is inspirated by illustration retrieved from [20].*

1.1.3 Potential adverse side effects

The efficacy of colistin against antibiotic-resistant strains from gram-negative bacteria is unquestioned. Nevertheless, well-controlled clinical trials conducted over the last 50 years have documented systemic adverse effects of CMS following its intravenous administration, implying that current clinical use is likely suboptimal. The most frequently seen adverse effects are neurotoxicity and nephrotoxicity, with acute renal failure being the most serious consequence of this drug. However, the term “renal failure” is very ambiguous term, so many nephrologists use the alternative “acute kidney injury (AKI),” based on the RIFLE (risk, injury, failure, loss, and end-stage kidney disease) classification. Understanding the propensity of colistin to cause nephrotoxicity requires a full recognition of it disposition in the body and particularly its handling by the kidneys.

1.1.3.1 Drug-induced kidney injury

The kidney is often the key organ that limits antimicrobial therapy. Kidney damage due to antimicrobials often manifest as AKI, which can be monitored by measuring the creatinine levels in the patient’s serum. Several factors play a role in microbial-induced renal impairment, including increased cardiac output that intensifies the blood flow through the kidneys. This can result in enhanced exposure of the kidneys to significant amounts of soluble drugs in the blood.

Renal elimination is the end result of three processes: the glomerular filtration, tubular reabsorption, and tubular secretion (Figure 5). Both reabsorption and secretion occur by a variety of facilitative transport systems that drive vectorial transport of solutes and drugs across the tubular epithelium. While many transporters are expressed in the proximal tubule cells, most can be generally classified into the organic anion transporter (OAT) and the organic cation transporter (OCT) families, which function as polypeptide transporters (PEPT1/2) or efflux pumps (MRP). These transporters are finely tuned to maintain the homeostasis of water, nutrients, and electrolytes. However, when it comes to the polymyxins like colistin, suboptimal transport by these transporters often causes tissue injury. For instance, when CMS is filtered through the glomerulus into the primary urine, water reabsorption must be accompanied by a partial reabsorption of the converted active colistin entity or the concentration of the colistin might become sufficiently high to be detrimental during passage through the loop of Henle and the distal tubules. The resulting intracellular accumulation can activate apoptotic pathways or cause irreversible cell damage, leading to apoptosis or necrosis. These processes are suspected to play a role in the renal nephrotoxicity of colistin.

1.1.4 Colistin-induced nephrotoxicity

Colistin primarily accumulates in the renal cortex regions, and its toxic effects at the cellular level include heavy damage to the kidney cell mitochondria. One suspected mechanism of kidney damage involves the colistin chemical structure, specifically the γ-amino L-Dab residues and fatty acid chains that have detergent-like qualities and may induce cell membrane leakage. Studies on bacteria, whose cell membranes are comparable to human cellular membranes, have shown that these detergent-like materials can be inserted into the cell membrane, leading to disruption of the lipid bilayer. A low cytoplasmic content of colistin might be tolerated by eukaryotic cells, as it is in bacterial cells, and any membrane disruption could be compensated by cellular repair mechanisms. However, high cytoplasmic drug levels would likely put too much stress on the structure of the lipid bilayer and cause the membrane to disintegrate. The subsequent uncontrolled passage of ions across the membrane would then disrupt the delicate osmotic homeostasis of the proximal tubular kidney cells and probably serve as a trigger that would invoke a cascade of signals leading to apoptosis or necrosis of the cell. Nevertheless, this hypothesis does not yet have experimental support and is based solely on the assumption that colistin can destroy the eukaryotic plasma membrane as well as it does with the bacterial membrane. The theoretical and experimental limitations of this hypothesis are: (i) bacterial membranes and eukaryotic membranes differ greatly in their lipid composition, as bacterial membranes consist largely of phosphatidylethanolamine and negatively charged lipids, whereas eukaryotic membranes contain large amounts of cholesterol; (ii) colistin is selectively toxic to proximal tubular cells; and (iii) red blood cells treated with colistin show no signs of hemolysis. Yun and colleagues used fluorescently labeled polymyxins to show that the renal damage induced by polymyxins occurs upon drug entry into the kidney cells. However, the mechanism of cell damage cannot be identified definitively without knowing the ways by which colistin enters the cells.

Colistin is administered intravenously as the inactive pro-drug CMS, as mentioned in the previous section. A small quantity of the CMS that is excreted through the kidneys is retrieved in the urine as the active colistin entity, implying that at least some of the CMS-to-colistin chemical conversion happens in the renal tubule. In reality, due to avid reabsorption by the proximal tubule epithelial cells, only a small amount of the colistin that is filtrated into the renal tubule is excreted by the kidneys. Colistin is positively charged; therefore, it diffuses only weakly across the plasma membrane. Consequently, its movement necessitates the employment of facilitative transport systems. Improved colistin clearance has been demonstrated following co-incubation with other cations, such as tetraethylammonium (TEA) and the dipeptide glycine-glycine (Gly-Gly), implying that OCTs and peptide transporters may be involved in the renal reabsorption of colistin. Lu and colleagues recently found that the oligopeptide transporter 2 (PEPT2, SLC15A2) could transport [3H]-polymyxin B1 and that this uptake was reduced by co-incubation with colistin. Another group recently identified the carnitine and organic cation transporter 2 (OCTN2, SLC22A5) as a novel transport system that recognizes colistin as a substrate and may contribute to colistin reabsorption at the apical side of the proximal tubule cell (2).

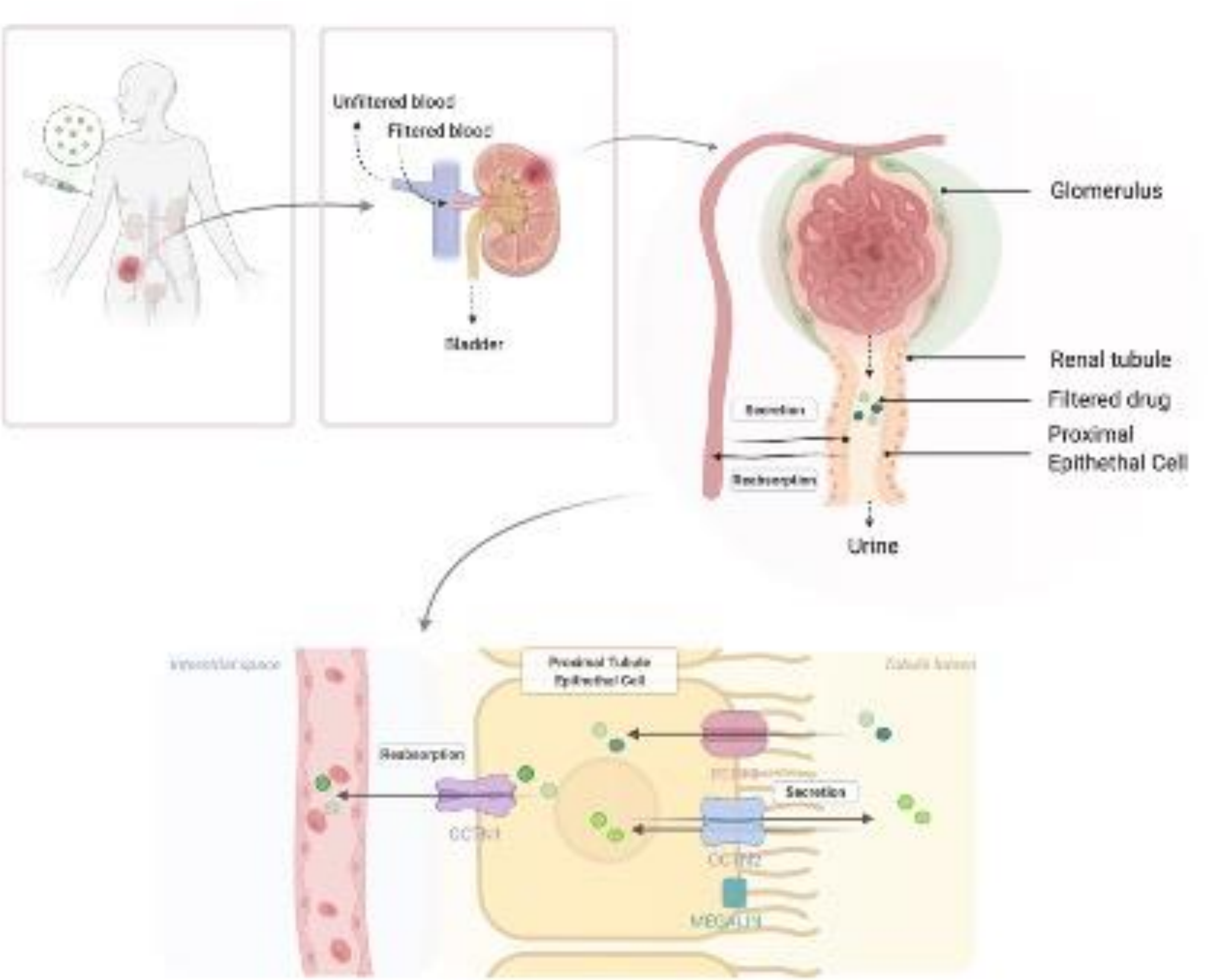

Figure 5 : A simplified representation of renal excretion of colistin. Filtration occurs as the renal artery approaches the glomerulus, allowing mostly small molecules to pass through and enter the renal tubule. Colistin falls within this category as well. The nephrotoxic effects result from colistin being reabsorbed into the blood artery and accumulating within the epithelial cells, where the permeability of the epithelial cell membrane increases, resulting in an increase in cation, anion, and water influx, which leads to cell swelling and death of the epithelial cell, also known as tubular necrosis. This figure is created by the author of this document using BioRender and is based on information retrieved from.

1.1.4.1 Colistin-induced neurotoxicity

Unlike the well-known nephrotoxicity of colistin, its neurotoxicity is a relatively under-documented but highly relevant side effect. The overall incidence of colistin neurotoxicity is less than 7%, and even multiple recent studies have not reported any cases. Among the wide range of neurotoxic side effects, paraesthesia has been the most frequently reported (7% to 23%). Reports of other neurotoxic effects are scarce, with only three cases of respiratory/ventilatory failure reported since 1970. This low number of reports could be linked to difficulties of objectively interpreting neurological symptoms, so that clinical nephrotoxicity and neurotoxicity reports may have overlooked potential associations with colistin.

Colistin-induced neurotoxicity is thought to arise due to drug interactions with neurons in the central nervous system (CNS). The accumulation of colistin in the brains of mice after multiple injections demonstrates that this low-molecular-weight compound is capable of crossing the blood–brain barrier (BBB) and then being absorbed by the neuronal cells in the brain tissue. By contrast, single-dose colistin injections yield negligible neuronal cell concentrations, implying that colistin absorption is still minimal. Large hydrophilic molecules cannot pass through the BBB because of the tight junctions of the interendothelial regions, and this is thought to be the primary explanation for polymyxins restricted BBB penetration (the molecular masses of colistin and polymyxin B are 1155 Da and 1,203 Da, respectively). Organic cation transporters are also found in the BBB, which regulates the flow of chemicals into and out of the CNS. OCTN1 and PEPT are the two of these proteins that are strongly thought to be the key mediators of colistin absorption. These are expressed in both kidneys and the BBB, supporting the suspicion that these two proteins play a significant role in the side effects colistin produces. However, these are still only speculations that need to be confirmed by additional research. Nevertheless, the mechanism by which colistin operates on brain cells is not fully understood, as neurological symptoms usually last temporary. While various theories about how colistin affects brain cells have been offered, no consensus has yet been achieved.

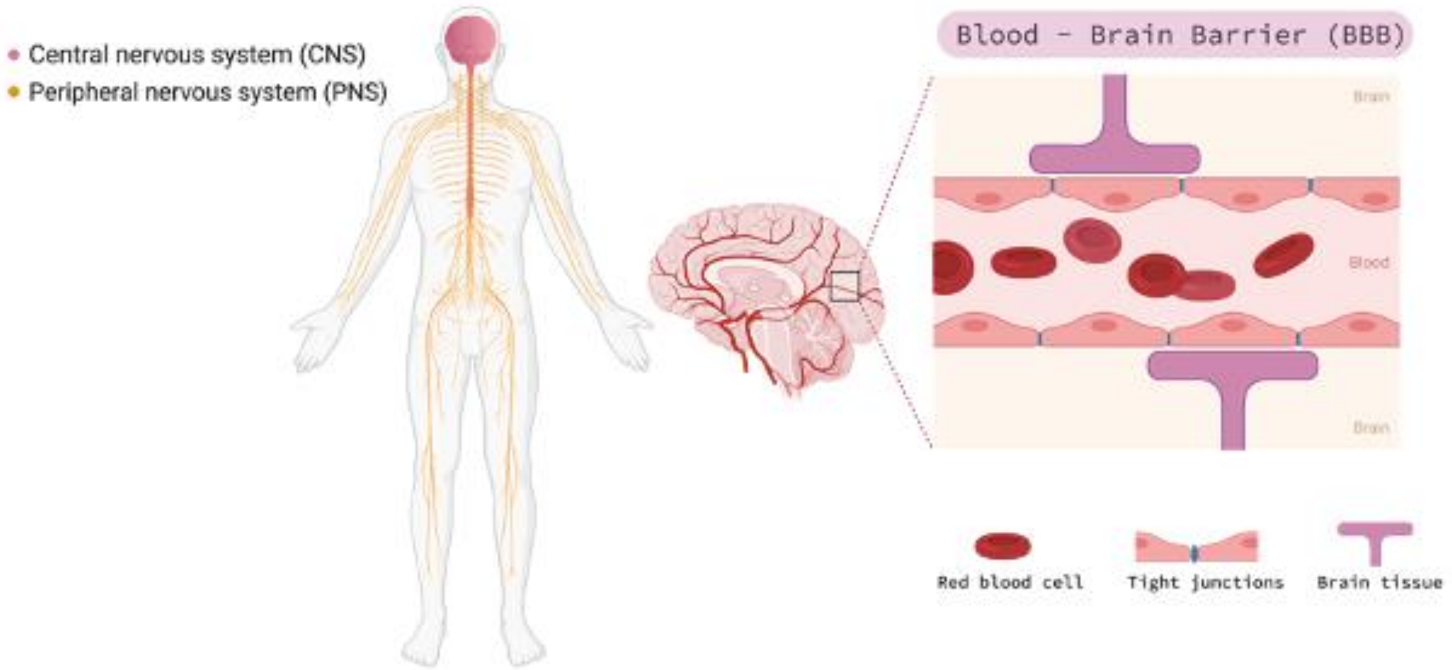

Figure 6: A simplified illustration of the central nervous system (CNS), peripheral nervous system (PNS), and blood brain barrier (BBB), where neurotoxicity is mostly associated. Colistin is absorbed into neuronal cells in the brain tissue via the blood-brain barrier (BBB). Only tiny, hydrophilic molecules can get across the membrane's tight junctions. Where colistin's molecular weight is insufficient to penetrate through. *This figure is created by the author of this document using BioRender and is based on information retrieved from.*

1.2 Therapeutic approaches to overcome challenges

As discussed so far, the efficacy of colistin as a therapeutical drug against infections arising from MDR gram-negative pathogens is unquestionable. Nevertheless, the drug's side effects of nephrotoxicity and neurotoxicity pose safety concerns that have led to limitations for its usage in clinical settings. As colistin is a last-line antimicrobial against MDR gram-negative bacteria, researchers started to look for alternative methods that would improve the safety of colistin while preserving its efficacy [21]. The common approach was to use the knowledge regarding the relationship between the structural features of colistin that are responsible for its bactericidal activity and the postulated colistin-induced nephrotoxicity to design drug variants with reduced toxicity and enhanced activity. This prompted researchers to reduce the number of cationic residues and their amphiphilic character or to synthesize pro-drugs in which the cationic groups of colistin are masked to form negatively charged derivatives [22, 23]. However, this approach has turned out to be rather slow, and only CMS has been so far clinically approved to treat MDR gram-negative infections [6]. Additionally, it has some drawbacks that have been briefly mentioned in the previous sections. While the reduction in charge helps to reduce the toxicity by minimizing the possibility of CMS interacting with internal targets, it is also accompanied by significantly reduced antimicrobial activity [24, 25]. Second, the slow and variable rate of release of colistin from the prodrug also complicates its pharmacokinetics, resulting in variable therapeutic outcomes for patients [24, 25]. This has led to a shortage and confusion in dosing regimens, leaving clinicians unable to make evidence-based decisions regarding dosing and route of administration to achieve optimal therapeutic efficacy. This is of great concern because subtherapeutic doses of colistin are not only inadequate but may also contribute to the development of bacterial resistance. Although the incidence of colistin resistance is relatively low at present, there is concern that it may increase in the future, potentially rendering this drug of last resort ineffective [22]. To address these issues, alternative and improved therapeutic approaches have been proposed [26].

In recent years, the development of topical delivery systems such as polymeric nanoparticles has emerged as an interesting solution to the challenges conventionally associated with the clinical utility of colistin [27]. Among the many possible drug delivery strategies, complex coacervate core micelles have been the one of particular interest. It was first observed that proteins with a high degree of opposing charges could form tight complexes where the protein remained flexible and accessible for its biological functions. This phenomenon has been studies as well for macromolecular assembly in the form of coacervation, in which opposingly charged polyelectrolytes electrostatically complex into micelles. Given the polycationic characteristic of colistin, it can easily go through coacervate complexation with an oppositely charged polyanion, where the resulting nanocomplex serves as a carrier for delivery of colistin to the targeted site[28]. It has been revealed that by loading colistin into drug delivery systems such as nanocomplexes, the therapeutic index of the drug can be significantly improved [29]. Lie et al. showed that when comparing loaded nanocomplexes of colistin with its corresponding free drug, the antimicrobial activity was increased substantially in the nanocomplex. Additionally, *in vivo* evaluation of a mice model revealed prolonged circulation times and decreased liver toxicity for the colistin nanocomplex [23]. Beyond the assembled nanocomplexes effect on antimicrobial activity and toxicity, it may also affect the pharmaceutical properties of the drug. It has been proposed that the nanocomplexes may be tuned to provide targeting properties and can be engineered to have a stimuli-responsive mechanism for control-triggered release of the drug [27]. For instance, Lane et al. demonstrated that a pH-sensitive depot system for the antibiotic ceftazidime was effectively retained until acidification of the endosomes led to spontaneous disassembly in which the drug was explosively released, and the endosomes broke. This reduced systemic exposure and enriched antibiotic activity at the site of infection [30]. These favorable attributes support the coacervation-induced nanoassembly approach for colistin delivery and catapult their use for treating MDR gram-negative bacterial infections without the concern of inducing toxicity upon administration.

In the next section, we will discuss the mechanism behind the encapsulation of colistin, which is the origin of the work presented in this thesis.

1.2.1 Nanoparticles by self-assembly of double hydrophilic block – copolymers

Two major classes of self-assembled nanoparticles are lipid nanoparticles, which offer simplicity and familiarity with cell membranes, and polymeric nanoparticles, that provide precise control over physical and chemical characteristics and surface modification for targeting [31]. Polymeric nanoparticles can be many shapes but are typically polymersomes or micelles that are assembled from diblock copolymers that are either amphiphilic or polyelectrolytes [32]. While the aforementioned assemblies are remarkable for many applications, however, they rely on the use of organic solvent and additionally the synthetic hydrophobic moieties are not very biocompatible [33]. Therefore, a particular polyelectrolyte block copolymer that has attracted more and more attention is a class of material known as double hydrophilic block copolymers (DHBCs), which consists of at least two different water-soluble polymer blocks [34]. Although the chemical nature of the two blocks can be diverse, most classical DHBCs consist of one permanently hydrophilic block to promote solubilization in water and a second hydrophilic block that is more generally pH responsive [34]. Because of their hydrophilic and charged nature, DHBCs offer delivery capabilities that differ from hydrophobically driven assemblies, as they can sequester different molecules and travel more freely throughout the body [35]. This has shown advantageous for delivering charged molecules such as the drug colistin to target the desired infected cell without harming any host cells [26, 36].

The main question arising now is how block copolymers formed by charged-neutral hydrophilic blocks can act as a transport system for the delivery of colistin. The first study on this type of drug delivery system was done in the 90's by Harada and Kataoka where they discovered that by mixing to oppositely charged polymer in an aqueous solution, they would electrostatically interact to form colloids, which is another word for nanoscale sized particles [37]. On the microscopic level, the attractive forces drive the polyelectrolyte complex to aggregate spontaneously to form charge-neutralized aggregates that have a droplet like structure [38]. However, on the macroscopic level, these aggregates will coalesce with time to form two immiscible liquid phases, a polymer-dense phase and a polymer-dilute “supernatant” phase. Where the dense, polymer-rich phase is simply referred to as the coacervate (*Figure 7*) [38, 39] .

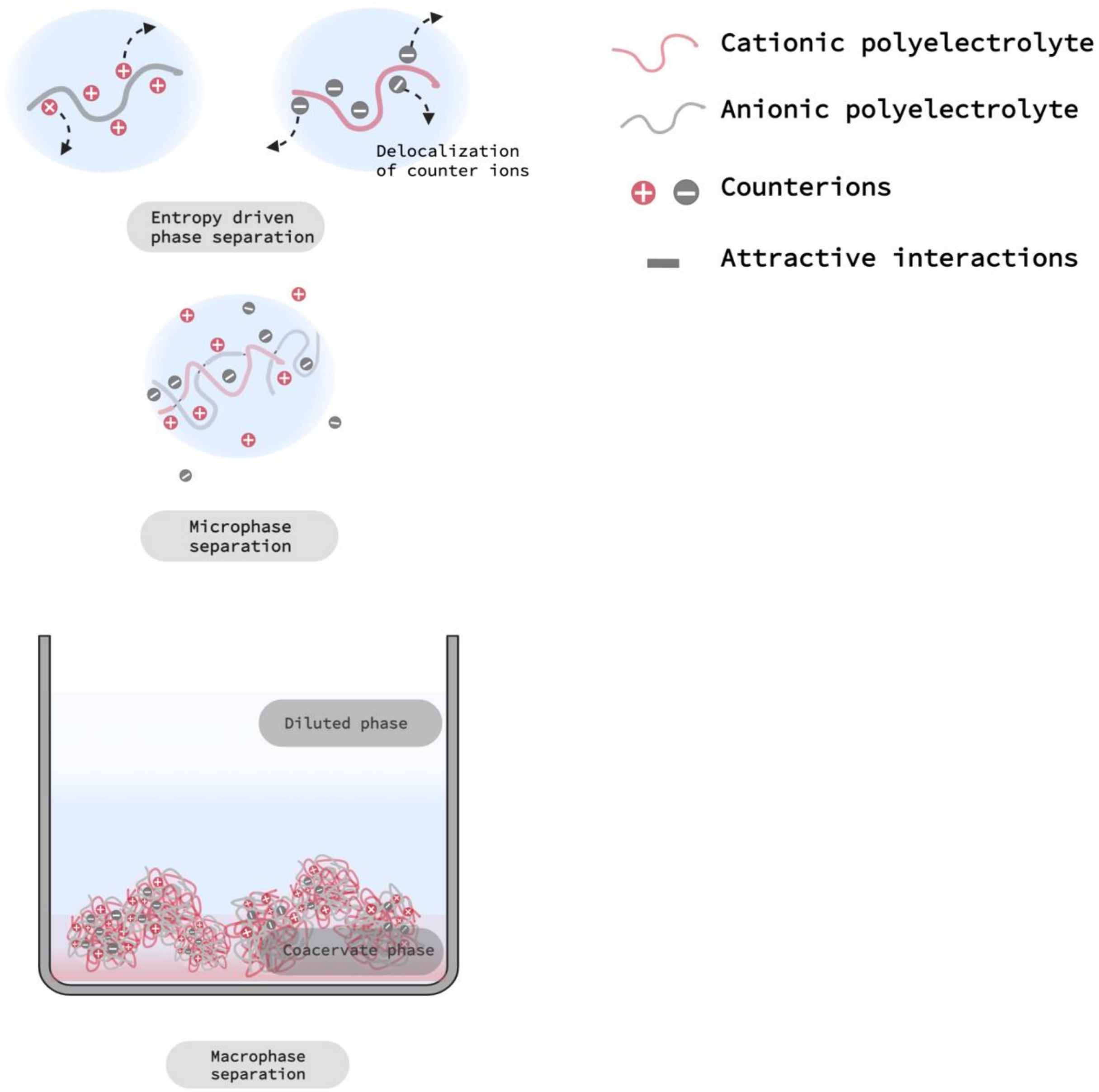

Figure 7: Schematic presentation of complex coacervation. The resultant coacervation liquid-liquid phase separation is depicted on both microscopic level (forming liquid droplets) and macroscopic level (droplet aggregates together) creating a dense phase. *This figure is created by the author of this document using BioRender and is based on information retrieved from [38-40].*

Coacervates spontaneously assemble due to a combination of several factors [39]. Essentially, it was believed that the only driving force for complexation was due to cooperative electrostatic interactions between the two oppositely charged polyelectrolyte [41]. However, it has since been shown that the thermodynamic driving force lies with the counterion species that are initially located near the backbone of the involved polyelectrolytes. These are generally highly soluble low molecular ions such as sodium and chloride. Before the two polyions with opposing charges are mixed together, their counterions bind themselves electrostatically to the chains of the polyelectrolyte, which results in the chain being more stable. The counterions are replaced by the oppositely charged polyelectrolyte during complexation, destabilizing the chains as the counterion contacts are lost and then re-stabilizing by the polyion [38, 39]. Because the counterions are constrained in there movement and position before complexation, they will upon complexation gain a significant entropy when they are released into the solution [36, 39] (*Figure 7*). Additionally, since water is highly polar, water molecules in the solution could interact with the ions and form a shell of water molecules around them [36, 41]. Therefore, the driving force for complexation derives not only from the increase in entropy during the release of the counterions from the polyelectrolytes, but also the release of water molecules from the hydrogen shells during complexation. In this case, the coacervates contains not only the oppositely charged polymers, but also a significant amount of "hydration" water from the original solution .

Aside from complexes of synthetic polyelectrolytes, these attributes for spontaneous coacervate assembly are also accessible to complexes of block copolymers with charged segments, as well as pharmaceutical molecules. Therefore, this phenomenon can be applied to DHBCs, where the charged polyelectrolyte block of a neutral-ionic DHBC can electrostatically interact with an oppositely charged molecule to form small complex coacervates in solution [36]. They have a core-corona spheroidal morphology, where the nonionic segment of the block copolymer will form a hydrophilic corona around the complexed core that is composed of the two oppositely charged segments [42, 43]. The coacervates that are formed by using DHBCs, resembles the amphiphilic response in an aqueous solution, and is therefore called complex coacervate core micelles (C3Ms) [42, 44]. The size of these coacervates is limited by repulsion between the neutral polymer blocks at the periphery of the complexes and are stabilizing the coacervates towards large-scale aggregation.

For this thesis, we propose such core-shell structures by complexation between a neutral-anionic diblock copolymer poly(ethylene oxide)-block-poly(methacrylic acid) (PEO-b-PMAA) and the cationic drug colistin. Coacervation is formed in a precise intermediate pH range, essentially at pH values lying between the pKa values of PEO-b-PMAA (pKa 5.5) and colistin (pKa 10-11), which is due to an increase in ionic strength on both PMAA and colistin at this pH-range [21, 34, 45]. However, as PMAA is a weak acid, it will change charges upon pH alterations causing the micelle to either assemble or disassemble in a pH-responsive manner [21, 46]. This feature can be taken advantage of given that the intracellular pH of cells is very low, which means that the drug can be released at the precise location of the infected cell. The effect of pH and other important factors on the C3Ms will be discussed in more detail in the next section.

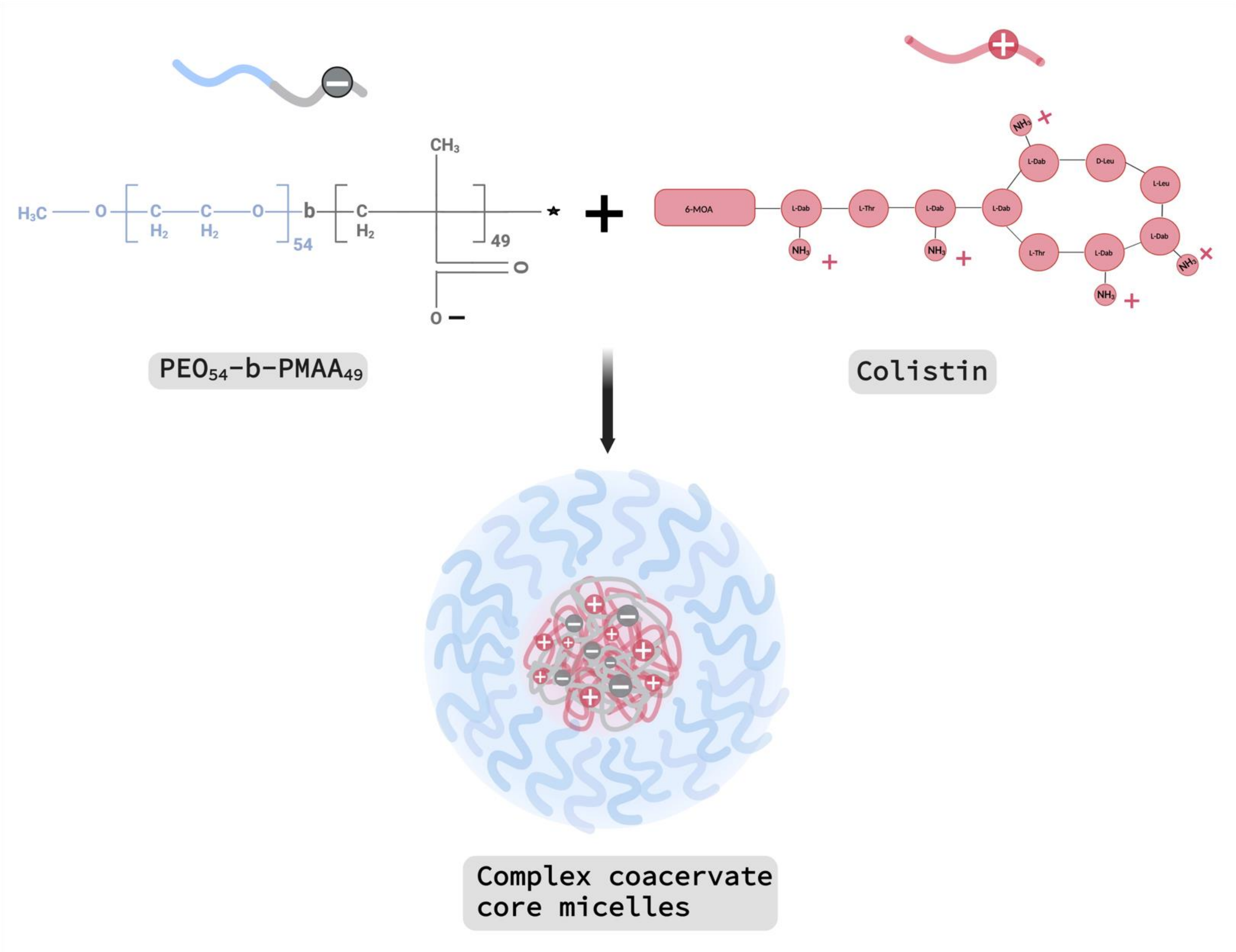

Figure 8: Simple illustration of the co-assembly of the DHBC PEO$_{54}$-b-PMAA$_{49}$ and colistin into C3Ms. The exact chemical composition of colistin can be found under Section 2.2.1 Figure 2. The neutral-anionic diblock copolymer used was PEO$_{54}$-b-PMAA$_{49}$, the subscription denotes the degree of polymerization for each block. The diblock copolymer and colistin associate to form C3Ms, where the neutral block forms a hydrophilic corona around the core. *This figure is created by the author of this document using BioRender and is based on information retrieved from [47].*

1.3 Kinetics for the formation of C3Ms

Since these coacervates are used for drug delivery purposes, understanding the driving forces behind the assembly of these C3M is important for controlling the exposure of the cargo. While initiation of C3Ms is known to be duo to the electrostatic interactions between the oppositely charged polyelectrolytes, however, the mechanism following this is in dispute. While there is a consensus that large-scale aggregates are initially formed due to spontaneous charge neutralization after mixing, the charge distribution and the size of these aggregates are unclear. The formation of large-scale aggregates is explained by the fact that they may not be charge neutral due to an inhomogeneous charge distribution in the complex core, which leads to excess of charges on the surface of the coacervate that can form aggregates by electrostatic interactions between the oppositely charged coacervates surfaces [48]. A study by Amann and co-workers suggested that the initial aggregation formation occurred within 2.6ms after mixing a charged-neutral diblock copolymer and an oppositely charged polyelectrolyte [48]. For another case study, Wu and co-workers reported formation of the assembled coacervates with spherical morphologies with a rather narrow size from the first 10ms to 5s, these grew rather over time due to merging clusters [49]. The different observations can be reasoned by the different polyanion used in each case, where Amann et al. used poly(styrene sulfonate) (pSS) and Wu et al. used poly(acrylic acid) (pAA), and for both these polyanions they were complexed with the same diblock copolymer poly(ethylene oxide)-block-poly(vinyl benzyl trimethylammonium chloride) (PEO-b-PVBTMA). It was shown PVBTMA+PAA would form liquid-like coacervates, while PVBTMA+PSS forms solid-like coacervates that are large aggregates at first but breaks apart into smaller spherical-core coacervates over time [48, 49]. Amann et al. reasoned this by two things: 1) a fast step involving internal charge neutralization that would lead to a homogenous charge distribution, where the coacervates from the aggregates would pinch off, and 2) a slow step where a continuous rearrangement would lead to form single core-shell coacervate complexes. The observations between Altmann et al. and Wu et al. suggest that the formation of the coacervates is highly dependent on the nature of the polyelectrolytes in the core of the coacervates. In addition, another point of view that was made was that the block length of the block polyelectrolytes may affect the rate at which the coacervate complexes forms aggregates and also the rate at which they will break apart from the larger aggregates to form single coacervate complexes.

1.4 Key parameters influencing polyelectrolyte complexation

The size and morphology of the C3Ms are vital for their success as a nanocarrier for therapeutical drugs. For instance, micelles that are smaller than 10 nm may be removed from the bloodstream by the kidneys, whereas micelles with a size above 200 nm are more prone to accumulate in the spleen and the liver [49, 50]. Additionally, the morphology of the micelle can have an impact on its distribution and cellular uptake [38, 40]. Therefore, control of the size and morphology is important in order to develop efficient C3Ms nanocarriers. Theoretical predictions show that the morphology of the coacervate complex depends on a variety of parameters such as the lengths of the neutral-charged diblock copolymer, the charge stoichiometry i.e., concentration, mixing ratio, salt concentration, temperature, and pH [21, 34, 40, 51]. For the sake of this thesis and factors that have been evaluated, we will only focus on the effects of stoichiometry and concentration, order of mixing, and pH.

1.4.1 Effects of block length on the structural properties

The length of the diblock copolymer chain plays a critical role in the formation and activity of colistin containing particles. It has been shown over the years that a critical length of the polymer is desired to efficiently bind colistin [52]. Additionally, the length of the diblock copolymer will determine the stability of the complex coacervate particle but also the dissociation and release of colistin [53, 54].

While there was little time to investigate different lengths of the diblock copolymer (PEO-b-PMAA) in our work, we had to choose between three block lengths of the charged block of the diblock copolymers: PEO54-b-PMAA9, PEO54-b-PMAA17, and PEO54-b-PMAA49. The choice of the length of the charged diblock was reliant on former theoretical predictions on the effect on the morphology [55]. Initial studies were done on the formation of C3Ms, which is AB + C system, where A is the neutral block and B is the charged block in the diblock copolymer and C is the oppositely charge homopolyelectrolyte [49]. These theories predicted that if the length of the neutral block A (NA) was roughly larger than the length of the charged block B (NB), it would form spherical micelles, while other elongated morphologies were observed if NA was shorter than NB. However, if NA was significantly shorter than NB it would rather lead to aggregation than stable complexes on the nanoscale[54]. These predications summed up are stating that a more symmetric DHBC is beneficial for the formation of micelles with spherical morphologies. Additionally, it was shown that the diblock copolymer length had an effect on the size and inner structure of the formed C3Ms. These studies observed that the radius of the core (Rcore) increased proportionally with NB, whereas NA had little effect on the Rcore. However, NA drives the thickness of the corona H, and thereby the hydrodynamic radius (RH) or the, which is a crucial component to the biodistribution. For instances, it was shown that if NB is short, smaller cores would form, which would increase the curvature of the core and thereby increasing the corona density since the C polymer chain will now be stretched outwards. The increase in the core curvature allows for spherical micelles to form [49, 53, 54]. Other experimental work suggested that the aggregation number or the number of chains in a given micelle (P) increased with increasing NB and decreased with increasing NA. The C polyelectrolyte length (NC) has shown to not influence any of the parameters, all agreeable with the theory given [54]. However, the charge ratio between the charges carried by polyelectrolyte C and polyelectrolyte B have a great impact on the formation and properties of the C3Ms. This will be discussed in more detail in the nest section.

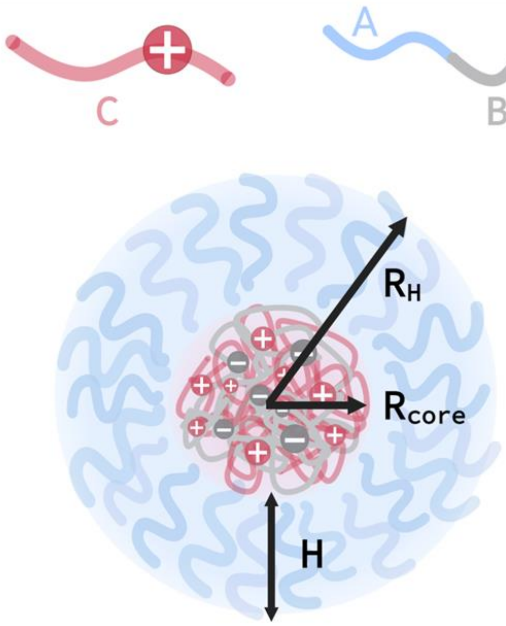

Figure 9. : Illustration of structural properties that can be effected by the different lengths of the block, where C represents the positively charged colistin and from the diblock copolymer we have A which is the neutral segment and B that is the negatively charged segment. The parameters of hydrodynamic radius (RH), radius of the core (Rcore) and corona thickness (H) will be evaluated in this thesis. This figure is created by the author of this document using BioRender and is based on information retrieved from [54].

The insight into this information gives us an idea about the relationship between each polymer block length and the morphology of the resulting micelles, which is beneficial when we are choosing the length of the diblock copolymer for our work. Based on these predictions, it was important to use a diblock copolymer where the neutral block (PEO) was briefly larger than the charged block (PMAA) to be able to form spherical micelles. For micelles of finite size, it was also kept in mind that NB should not be too long due to its correlation to Rcore, additionally to avoid formation of large clusters. Therefore, the diblock copolymer length used in this work was PEO54-b-PMAA49. It is important to note that these are only assumptions, and it is not given that we would form spherical micelles of finite sizes by complexation with colistin.

1.4.2 Effects of stoichiometry

The charge ratio between NH_2 groups carried by colistin and the COOH groups carried by the PMAA block is an important parameter in the micelle formation [47, 56]. The counter-polyion/copolymer charge ratio can be expressed as a mixing fraction Z, with

$$Z = \frac{[NH_2]}{[COOH]} \qquad (1)$$

where $[COOH]$ and $[NH_2]$ are the monomer concentrations of the negatively charged copolymer and the positively charged counter-polyion in the solution, respectively [56]. Typically, C3Ms forms at a relatively narrow composition window around the so-called preferred micellar composition (PMC), which corresponds to a mixing fraction of 1:1 where there is an equal amount of positive and negative charges of the polyelectrolytes [47]. Most studies have focused on this stoichiometric charge balance, but more recently non-stoichiometric conditions have also attracted attention due the formation of rather loose aggregates than micelles. Typically, aggregation into larger and more dense objects is because of an excess charge on these aggregates. In literature, these structures are called soluble complex particles (SCPs), and their charge sign is determined by the excess component. For instance, upon addition of the diblock copolymer consisting of a negatively charged block, there will be an excess of these negative charges ($Z < 1$), and anionic SCPs will be formed. By the addition of an oppositely charged molecule, the anionic SCPs will be consumed until PMC is reached (Z = 1) and now C3M is formed. It is believed by increasing, excessively, the positively charged molecule ($Z > 1$), the C3Ms dissociate into singular polyelectrolytes again. In this case, there will be an excess of positive charges and cationic SCP are formed [56]. It is important to note that these predictions are given for a system with a constant pH, ionic strength and mixing ratio. The reason behind these conditions will be explained in the nest sections.

1.4.3 Effects of pH and disassembly

In the case of C3Ms, the presence of controlled strong interactions between the charged segment of the diblock copolymer and the drug is the key to construct efficient system in terms of stability and controlled drug release. In order to form C3Ms, the pH-sensitive segment of the diblock copolymer and the drug have to be fully charged at a given pH to bind electrostatically to each other [21, 34]. Additionally, the disassembly of C3Ms is caused by interrupting the binding interactions, which occurs at a pH where the charges are "turned off". Therefore, pH is considered to be an important factor in both the assembly and disassembly of C3Ms.

A good example of this pH-responsive behavior of C3Ms was reported by Boudier et al., where the authors studied the complexation behavior between a weak polybase (oligochitosan, pKa 6.5) and a weak polyacid (PEO-b-PMAA, pKa 5.5) as a function of pH [35]. From this study, it was observed that micelles were first formed at pH 6.5, and they remained stable between pH 5 and 7 after changing the pH of the solution. Additionally, a disassembly of the complex was observed at pH<5 due to the decrease of charges on the copolymer, PMAA, preventing electrostatic interactions. A more recent study by Abouelmagd and co-workers was done for the complexation of tannic acid (TA) with colistin [21]. The phenolic hydroxyl groups on TA gives the characteristics of a weak acid (pKa 5 – 8.5), where it can facilitate hydrogen bonding and/or electrostatic interactions depending on the pH of the solution. Typically, at pH below pKa, weak acids are only deprotonated to a small extent so that more swollen and loose complexes are formed. Abouelmagd et al. observed that the interactions within the complexes at pH 5.2 were stabilized by additional hydrogen bonding between amine groups of colistin and the hydroxyl group of TA. Nevertheless, the complex completely dissociated upon exposure to pH 4.5. At this low pH-level, it was considered that the electrostatic interactions were completely lost within the complex. While the hydrogen bonding was not disturbed by lowering the pH, it might have not been strong enough on its own to maintain the assembled complex. This observation indicates the importance of cooperativity between the different modes of interactions for formation of stable complexes.

The theoretical aspects of these studies resemble the work in thesis and has been taken into consideration when attempting to form C3Ms. Coacervation is said to occur at pH values lying between the pKa values of PEO-b-PMAA (pKa 5.5) and colistin (pKa 10-11) due to an increase in ionic strength on PMAA and colistin at this pH-range [21, 34, 35]. However, as PMAA is a weak acid, it will change charges upon pH alterations causing the micelle to either assemble or disassemble in a pH-responsive manner.

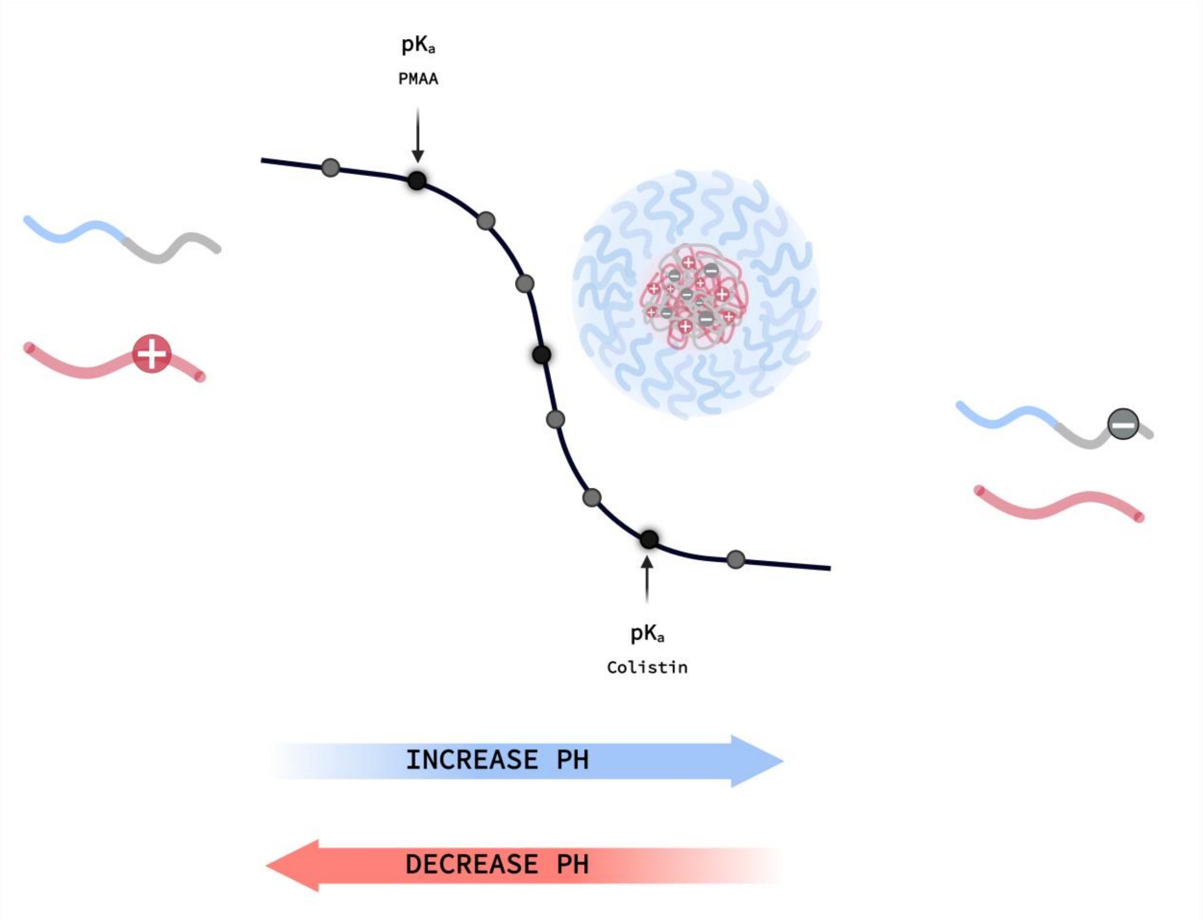

Figure 10: A schematic presentation of the effect of pH on C3Ms. Colistin is has a pK$_a$ value of 10-11 and is only charged at pH values that are lower than its pK$_a$. For PMAA that has a pK$_a$ value of 5.5, it is only charged at pH value that is above its pK$_a$ value. For the system we have investigated, colistin and PMAA are fully charged at pH 7.4, which is a pH between the two compounds pK$_a$ value, therefore at this pH they form C3Ms. This figure is created by the author of this document using BioRender and is based on information retrieved from [21]

First, since the pH of the solution has an important effect on the polyelectrolytes charge density, it can also impact the stoichiometry of the complexes formed, where the mixing ratio (Z) will vary for the same mixture of polyion at different pH values [57]. In order to control the degree of ionization, the complexation must occur in a buffer solution, where the desired pH value remains constant over the entire course of binding. Another aspect to consider regarding the solution of the complexation is the ionic strength . Where an increased ionic strength will screen the electrostatic interactions between the two polyelectrolytes and prevent the formation of C3Ms. Moreover, the salt concentration can cause the structure of the complexes to rearrange to form smaller particles at low salt concentration but aggregation at higher salt concentration [40]. Therefore, the ionic strength of the medium must be relatively low (< 100 mM) in order to successfully form C3Ms [58]. It is important to keep in mind that the ionic strength in biological media is typically very high and may lead to a decrease in the colloidal stability of the system leading to either aggregation or decomplexation. In this work, we mainly used phosphate-buffered saline (PBS) as the buffer solution at pH 7.4, which had an ionic strength of approximately 160 mM [59].

1.4.4 Effects of mixing order

Different ways of mixing the PEO-b-PMAA copolymer with colistin to form C3Ms are possible, and the variety of the mixing conditions used makes it difficult to rationalize their role on the morphology and properties of C3Ms [40].

As discussed under the kinetics, the association of the polyelectrolytes occurred within milliseconds after mixing a charged-neutral diblock copolymer and an oppositely charged polyelectrolyte. With this in mind, C3Ms are preferentially obtained with a fast mixing of the two components. Additionally, the mixing of the two components was performed under stirring to allow a good homogenization of the two solutions and avoid local over concentration during the complexation step. Unfortunately, this aspect is not always mentioned in the formulation process of C3Ms. It is also important to consider the order of which polyelectrolyte is added, since it will dictate what polyion is in excess at the beginning of the assembling process. For example, at a non-stoichiometric mixture($Z = 2$), if the polyanion is added to the polycation there will always be an excess of positive charges in the complexes, and the repulsive forces between them will help maintain the stability of the particle. However, if the polycation is added to the polyanion, the excess negative charge of the complex will be neutralized halfway through the addition of polycation, resulting in aggregates [57]. Therefore, the most reliable formulation pathway is when the component in deficit is added to the one in excess.

1.5 SAXS as a characterization technique

When characterizing such core-shell structures, two factors must be considered: 1) whether or not the complexation process between the diblock copolymer PEO-b-PMAA and colistin was successful, and 2) the physiochemical properties of the formed micelles, such as morphology and size, which play an essential role in the biological activity of the nanoparticles. Therefore, various characterisation methods have been introduced as valuable tools to probe these features. In this thesis, small-angle X-ray scattering (SAXS) is one of the key techniques employed to study the colistin-polymer interaction. In general, scattering techniques are some of the most powerful non-invasive methods used for structural characterisation of materials whose size is between 1-100 nm [60]. Because of the non-invasive nature of scattering techniques and the micelles diameter being in the order of 10-30 nm, scattering techniques are a natural choice for studying the structure of micelles. The following sections will briefly discuss general scattering techniques before taking a closer look at small-angle scattering with X-rays. For detailed reviews and theoretical background, the reader is referred to standard textbooks [61-63].

1.5.1 General Theory of Small-angle Scattering

Scattering theory is a big field, and a large amount of techniques are based on these fundamental principles, including small-angle X-ray scattering (SAXS), which is used in this work. Figure 11 illustrates a general scattering event. The underlying principle of any scattering technique involves the radiation of an incident monochromatic beam with the wavevector k_i on a sample. In the case of SAXS, high energy X-ray photons will interact with the outer part of the electronic cloud of an atom. While most of the radiation is transmitted through the sample, some of the beam will be scattered away from the incident direction. The scattered intensity is recorded by a 2D detector at a given angel θ with respect to the incident radiation resulting in a scattering pattern on the detector. The scattered intensity is recorded by a 2D detector at a given angel θ with respect to the incident radiation resulting in a scattering pattern on the detector. The scattered intensity consist of different wavevectors, $\vec{\mathbf{Q}}$. By implementing Braggs equation, it can be shown that the wavevector has an inverse proportionality to the real length-scales (d), $\mathbf{d} = \frac{\mathbf{2\pi}}{\vec{\mathbf{Q}}}$. Where smaller wavevectors will hence correspond to larger structures. By radially averaging the scattering pattern from 2D to 1D pattern, we can subtract the scattering from the buffer with the sample. After this we are left with the scattering pattern of the structure we want to study. This scattering pattern can be compared to theoretical scattering from analytical models, and in this way, we can obtain valuable structural information.

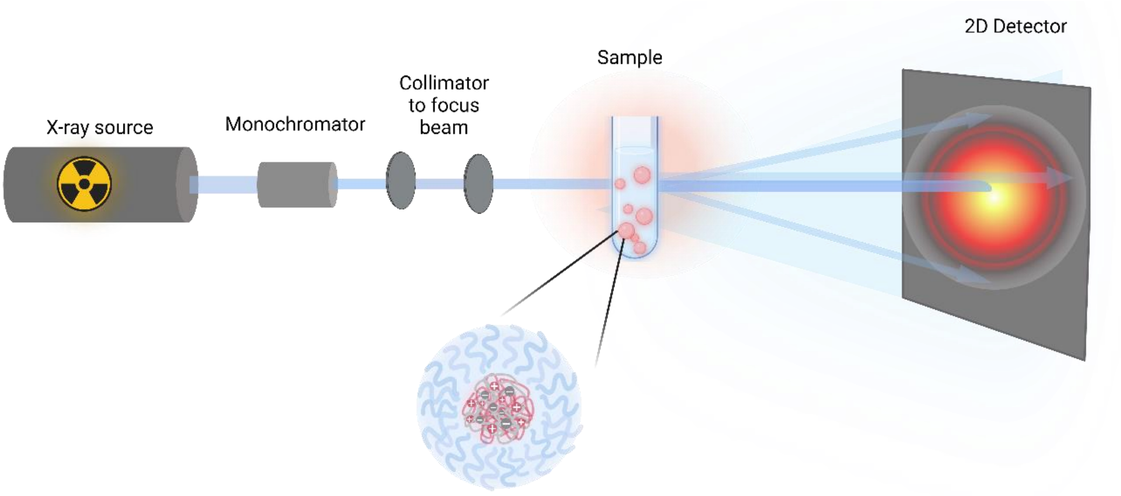

Figure 11. Illustration of a small angle X-ray scattering setup with an X-ray source and monochromator that gives a direct beam that scatters in a sample, giving a scattering pattern on the 2D detector.

1.5.2 Elastic small-angle scattering

An important feature to distinguish is if the scattering is elastically or inelastically. In inelastically scattering, the kinetic energy of the particles is not conserved, and typically it has less or more energy than before the scattering event. Elastic scattering occurs when there is no loss or gain of energy in the scattering event, meaning that the energy of the scattered waves and the incident beam is equal, $E_i = E_s$. When it comes to X-rays, the electric field caused by the incoming wave of photons makes the electrons in the sample oscillate and emit photons. If the emitted photons have a spherical electric field with the same energy as the incoming photons which is caused the oscillation, the scattering process is said to be elastic. Therefore, we will only consider elastic scattering in SAXS.

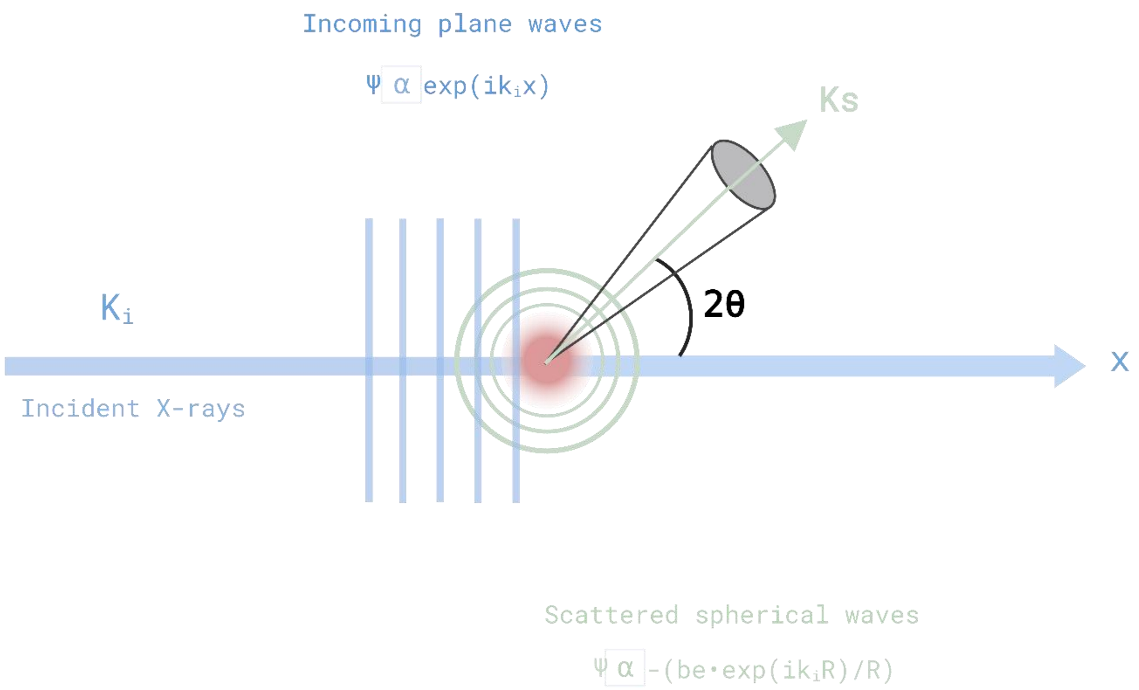

Figure 12. Illustration of the key elements in a basic scattering event. The cone represents the solid angle with area $d\Omega$. This figure is modified from [81].

A simplified sketch of the scattering geometry is depicted in Figure 12. In terms of scattering experiments, it is more practical to describe the radiation as waves instead of particles. We can therefor say that the incident and scattered beam wave have the same energy, and their interference will only affect the amplitude of the wave. The wavefunction is defined using the maximum amplitude A as

$$\psi(\vec{r},t) = A\ exp\left(i\left(\vec{k}_i\vec{r} - \omega t\right)\right) \tag{2}$$

where $\vec{k}_i$ is the wavevector of the incident wave, and ω is the angular frequency in the medium. In Figure 12, $d\Omega$ is the solid angle, which is the angle in which incoming particles with a cross-sectional area of $d\sigma$ are scattered into. The magnitude of the incident and the reflected waves are characterised by wave vectors, , $\overrightarrow{k_\iota}, \overrightarrow{k_s}$, respectively, which is given by:

$$\left|\overrightarrow{k_s}\right| = \left|\overrightarrow{k_\imath}\right| = \frac{2\pi}{\lambda} \tag{3}$$

where λ is the wavelength of the incident and scattered radiation [79]. These wavevectors however are dependent on different parameters like wavelength , detector distance, scattering angles and radiation type. To be able to compare results measured using different parameters, a more convenient parameter is used. The scattering vector, $\vec{Q}$, expresses the momentum transfer and is defined as the difference between the scattered wavevector (k_s) and the incident wavevector (k_i) [79]:

$$\left|\vec{Q}\right| = \left|\overrightarrow{k_s}\right| - \left|\overrightarrow{k_\imath}\right| = \frac{4\pi}{\lambda}\sin(\theta) \tag{4}$$

where θ is the scattering angle. From Equation (4) it is clear that the observed scale in a scattering experiment is inversely proportional to the wavelength. Figure 13 displays a simple scattering event and the corresponding scattering vector.

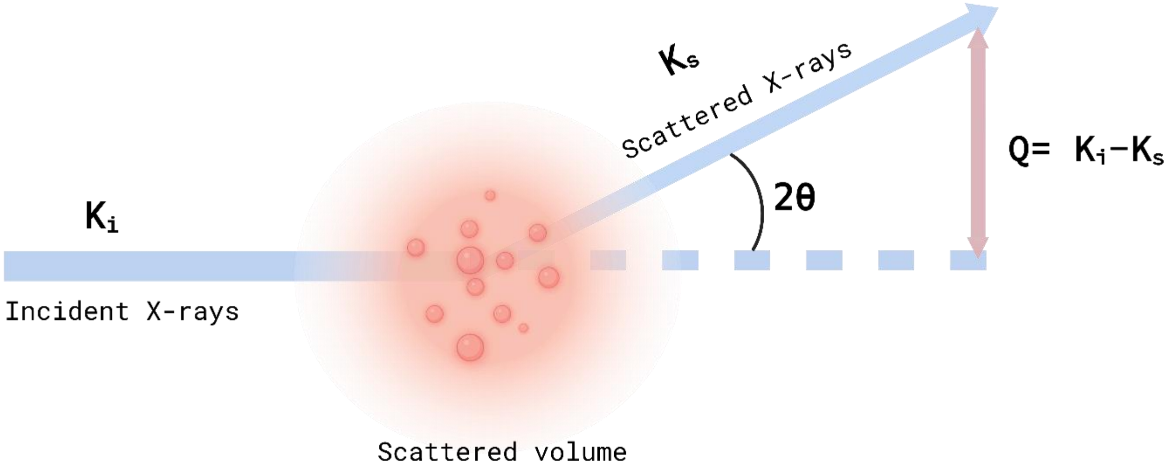

Figure 13. Illustration of a simple scattering event in a sample volume. The scattering vector Q, which is the momentum transfer in the scattering event. The vector is not illustrated in this sketch, for correct see Equations (2) and (3).

For an assembly of N particles at individual positions $\vec{r}$ with fixed orientations (for example colloids or micelles), the scattering pattern recorded arises from the incident monochromatic plane waves interacting with the particles in the solution. The amplitude of the plane waves at position $\vec{D}$ are expressed as:

$$A_i(\vec{D}) = A_0 \exp(i\vec{k}_s\vec{D}) \tag{5}$$

where A_0 is the amplitude of the incidental wave. The interaction leads to the emission of spherical secondary at position $\vec{D}$ with wave functions A_i. But since the sample and the detector distances are large compared to the dimensions of the sample, the detected waves can be considered to be planar. This distance is referred to as the scattering length (b_i), and is a measure of the interaction strength that describes how well a given material scatters the probing waves. Which also determines the amplitude of the scattered waves at position $\vec{D}$, and can be given as:

$$A_s(\vec{D}) = A_0 \exp(i\vec{k}_s\vec{D}) \cdot \frac{b_i}{\vec{D}} \tag{6}$$

In comparison the incident beam, the scattered beam will have a number of particles i per unit area that will decrease with distance D, hence the $1/D$ dependency. The scattering length b_i

depends also on the type of radiation source and electron density of the nuclei of the sample, and is therefore proportional to the atomic number. The scattering length b_i is defined as

$$b_j(\overrightarrow{q}, t) = \int_{V_j} \Delta\big(r_j, t\big) \exp\big(-i\overrightarrow{q}\overrightarrow{D}_j\big)\, d^3 \cdot \vec{r}_j \tag{7}$$

where the integrations is run over the entire sample volume that contains all scattering particle *j*. This is because for realistic samples, containing free particles, there will be a large amount of scatterers, and the amplitude measured at the detector distance $\overrightarrow{D}$ will rather be an average of all of these scattering amplitudes. Additionally, it will also be interactions between other scatterers and the scattered waves. Therefore, for assemblies of micelles, a more relevant quantity used is $\rho(r_i, t)$, which is also described as the total scattering length of the atoms per unit volume and can be thought of as the local density of scattering material. If there is no change in the dielectric constant or no difference in the scattering pattern between the sample and solvent, $\Delta\rho(r_i, t)$ and b_i will be zero, and no scattering event occurs.

However, by using Born approximation, which is an assumption that only single scattering processes occur, and that the incoming field is not perturbed by the sample such that the scattered field can be assumed to equal to the incoming field. The total scattering event can be considered as a superposition of each individual scattering amplitudes This can be described as:

$$A\big(\overrightarrow{Q}\big) = \sum_i b_i \exp\,(-i\,\overrightarrow{Q}\, r_i) \tag{8}$$

where r_i is the position of each scattering particle.

Unfortunately, there is no experimental access to the scattering wave vector amplitude. The detector is only able to measure the scattered intensity, I_s. The relation between these two parameters are

$$I_s\big(\overrightarrow{Q}, t\big) = \big|A_s\big(\,\overrightarrow{Q}, t\big)\big|^2 \tag{9}$$

Therefore the scattered intensity is:

$$I_s(\overrightarrow{Q},t) = \frac{A_0^2}{D^2}\sum_{j,k=1}^{N} b_j\left(\overrightarrow{Q},t\right)\ \exp\left[-i\overrightarrow{Q}\left[\overrightarrow{r_j}(t)\right]\right] \cdot b_k(\overrightarrow{Q},t)\exp\left[-i\overrightarrow{Q}\left[\overrightarrow{r_k}(t)\right]\right] \quad (10)$$

where $\overrightarrow{r_{j,k}} = \overrightarrow{r_j} - \overrightarrow{r_k}$. The term before the sum is merely an instrumental constant, and the intensity depends only on the scattering lengths and positions of the scatterers.

In dilute samples where the interactions between particles are negligible, they experimental scattering intensity can be written as:

$$\langle I_s(\overrightarrow{Q},t)\rangle = N\left\langle\left|b_j(\overrightarrow{Q})\right|^2\right\rangle = N\langle|b(0)|^2\rangle\, P(Q) \quad (11)$$

where P(Q) is the form factor defined so that $P(Q) \rightarrow 1$ as $Q \rightarrow 0$. The form factor is also dependent on the distribution of the scattering material, is therefore expressed as

$$P(Q) = \frac{\left\langle\left|b_j(\overrightarrow{Q})\right|^2\right\rangle}{\left\langle\left|b_j(\overrightarrow{0})\right|^2\right\rangle} \quad (12)$$

Given that the density of the scatterer depends on the samples morphology, the form factor is used to determine the structural information of the sample, meaning the size and shape of the particle. Not all particles will have the exact same size but a range of different sizes. This will cause a smearing of the oscillations in the P(Q), where the form factor of each Q-value will rather be an average of the form factor of differently sized particles. To take in account the polydispersity in the form factor, a integration is run over a normalised size distribution, D(N), and is given by:

$$\overline{P(Q)} = \int D(N)P(Q,N)dN \quad (13)$$

The detector measures the intensity by counting the flux of photons hitting the detector. The intensity is proportional to the differential scattering cross-section $d\sigma/d\Omega\ (Q)$, which represents the probability of a X-ray photon of the incident beam being scattered out from unit sample volume into the solid angle $d\Omega$. One can than normalise with respect to the number of transmitted photons since some of the incident beam will be absorbed in the material. The scaled absolute intensity is

$$I_{abs} = \frac{I}{V}\frac{d\sigma}{d\Omega}(Q) = \frac{C}{C_0 \Delta\Omega \mathrm{Te_s}} \tag{14}$$

where C and C_0 represents the flux collected at the detector and of the incident beam, T is the sample transmission, e_s is the sample thickness and $d\Omega$ is the area of the solid angle the wave is scattered into. Higher electron density will give stronger scattering, meaning that heavier atoms have larger scattering lengths.

The scattering cross-section per particle at small angle can also expressed using

$$\frac{d\sigma}{d\Omega}(Q) = \frac{1}{N}\left[\sum_i b_i \exp(iQD)\right]^2 \tag{15}$$

where b_i is the scattering length of the particle at position D in the sample and N is the number of particles. Another alternative is to use the scattering length density (SLD) $\rho(r) = \sum \rho(r)_i b_i$ to express the previous equation:

$$\frac{d\sigma}{d\Omega}(Q) = \frac{1}{N}\left[\int_V \rho_i(r)\exp(iQD)\, d^3r\right]^2 \tag{16}$$

For X-ray scattering the scattering length density is defined as

$$\rho(r) = \left(\frac{e^2}{mc^2}\right) n_{el}(r) \tag{17}$$

where e^2/mc^2 is the Thompson scattering length of an electron and $n_{el}(r)$ is the electron number density in the sample which for SAXS is the number of electrons divided by the volume of a scatterer: $n_{el} = \frac{Z}{V}$.

The term contrast or excess scattering length can also be introduced and is defined as the difference in scattering length density of the sample and the solvent, $\Delta\rho = \rho - \rho_0$. This excess scattering gives scattering intensities sensitive to the sample studied. For a binary system (i.e. solvent and micelles only), the scattering intensity is a function that depends on Q, the number density of scatterers (n_z), the contrast, the volume of the single particle of component 1 (V_1), the inter-particle structure factor $S(Q)$, the form factor $P(Q)$, and a constant background (B) originating from solvent and incoherent scattering:

$$I(Q) = n_z \Delta\rho^2 V_1 P_1(Q) S_1(Q) + B \tag{18}$$

The form factor $P(Q)$ can be expressed in terms of the form factors $P_i(Q)$ and form factor amplitudes $A_i(Q)$ of the different components in the sample.

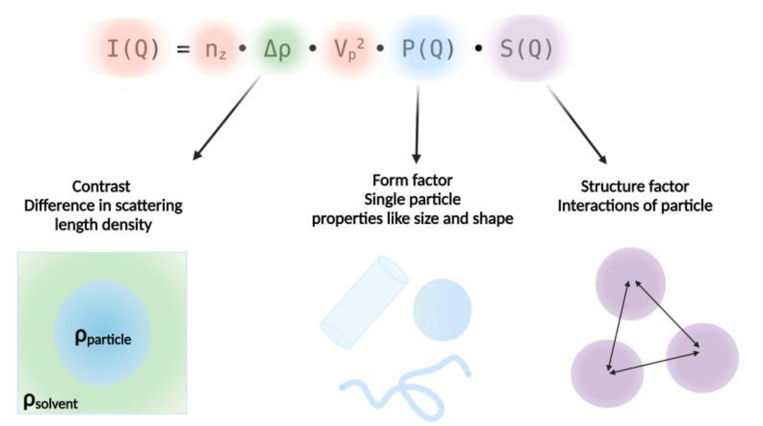

Figure 14. Schematic illustration of the different parameters for the scattering intensity I(Q) on an absolute scale. The equation is given by $I(q) = n_z \Delta\rho V_p^2 P(q) S(q)$. Where the n_z is the density number, V_p is the volume of the particle, $\Delta\rho$ is the contrast, P(q) is the form factor and S(q) is the structural factor.

The intensity of the measured radiation depends on whether the scattering process is constructive or destructive. The interference, in turn, depends on the phase difference between the incoming and scattered radiation. By superposition of the scattering from each nucleus, the average effect of the phase difference is given in the form factor amplitude:

$$A(Q) = \frac{I}{N} \sum_{j=1}^{N} \langle \exp\left(-iQ \cdot r_j\right) \rangle \tag{19}$$

where $Q \cdot r_j$ is the length of the path of the scattered radiation compared to the incoming radiation and $\langle . \rangle$ is the average over alle orientations of the particle. The amplitude cannot be measured independently. Instead, the form factor $P(Q) = A(Q)A^{*}(Q)$, where $A^{*}(Q)$ is the complex conjugate of $A(Q)$, is measured. The form factor can now be written as

$$P(Q) = \frac{I}{N^2} \sum_{j=1}^{N} \sum_{k=1}^{N} \langle \exp\left[-iQ \cdot (r_j - r_k\right] \rangle \qquad (20)$$

For non-uniform objects with multiple possible configurations a probability distribution must be applied to describe the density distribution.

The correlations between the positions of the scattering particles in the sample is included in the structure factor $S_1(q)$. The interactions become less prominent with fewer particles, $S_1(q) \rightarrow 1$ as the concentration approaches zero. For dilute samples, one can assume the form factor and contrast to be the only contributors to the scattering curve.

The scattering data analysis can be done by both using models and by model-independent analysis. In this thesis, the analysis were performed using analytical models. The analytical model used will be presented in the next section, and the idea is to fit the analytical function to the obtained data to fin structural information.

1.6 Theoretical modeling for SAXS data

To comprehend the workings of the world around us, we require suitable tools to describe it accurately. A model should strike a balance between being detailed enough to represent the real-world behavior we are investigating and not being too complicated to interpret the results effectively.

For C3Ms systems, the choice of model and how we describe them using analytical models is a delicate balance between representing the relevant properties of the micelles and the actual scattering data. To understand the interactions occurring in the complexation process, it is essential to gather as much information as possible about the drug colistin itself and the diblock copolymer PEO-b-PMAA. This includes determining the size and shape of the individual components in solution. However, when it comes to particles that contain two or more components, the scattering observed is usually not easily described. Therefore, a more sophisticated model is needed to find the correct structural parameters. Initially, it was assumed that the micelles obtained from the complexation between colistin and PEO-b-PMAA were spherical, and a model for spherical core-shell particles was used. However, this model did not fit our data, and thus, we had to resort to using a more general model from the software PRIMUS, which will not be described in this thesis.

In the following section, we will explain the form factors employed in various models, followed by the presentation of the analytical model for free chains. As mentioned in Section 1.5.2, the scattering intensity for a dilute sample can be expressed as follows:

$$I(Q) = n_z \Delta\rho^2 V_1 P_1(Q) S_1(Q) + B \tag{20}$$

In order to describe the scattering behavior from the sample, it is important that the analytical model can accurately describe the density and the SLDs, and also they must have the correct form factor.

1.6.1 Scattering model for unmixed polymer and colistin solution

The scattering from an unmixed polymer and colistin solution can be analyzed by using the analytical model for free chains, called the Beaucage model, to determine the R_g. This model is developed by Greg Beaucage and is used to fit experimental data obtained from SAXS to describe the intensity scattered in the Guinier regime [64]. The model contains three parameters: a Guinier scaling factor G, a radius of gyration R_g and a fractal dimensions d_f. The form factor $P_{polymer}$ (Q), for a random, unstructured polymer and peptide chain is given by the Debye expression for Gaussian chains:

$$P(Q)_{polymer} = \exp\left(-\frac{Q^2 \cdot R_g^2}{3}\right) + \frac{d_f}{\left(Q \cdot R_g\right)^{d_f}} \Gamma\left(\frac{d_f}{2}\right) \cdot \left(\frac{[erf\left((Q \cdot Rg)/\sqrt{6}\right)]^3}{Q}\right)^{df} \qquad (21)$$

where Q is the scattering vector, R_g is the radius of gyration and Γ(x) is the gamma function. The d_f is the fractal dimension, which can be 1.7 for a polymer in a good solvent condition or 2 for a theta solvent. Since the Guinier regime applies at low Q and Porod form applies at high Q (given by the Porod exponent d), the term erf(x) which is an error function provides a smooth transition between the two regions. The scattering length density ρ_0 and ρ_p for the solvent and polymer, respectively, was calculated accordingly to the given equation:

$$\rho = \frac{N_A \sum_i Z_i}{M/d} r_0 \qquad (22)$$

where N_A is Avogadro's number, M is the molecular weight of the average polymer repeat unit or solvent molecule, d is the corresponding density of respective (d_0 and d_p is the density of the solution and polymer, respectively), Z_i is the number of electrons of element i and r_0 is the radius of the electron.

Assuming that the free diblock copolymer forms coacervates was modeled as a spherical object of mean size <R_p> with the idea that the coacervate had an “fuzzy” outer surface (typically the PEO shell) that was characterized by a roughness parameter, σ_R. This parameter is taken into consideration, and also the fact that it is assumed that the nanoassemblies size have a Gaussian distribution. Therefore, the total scattering intensity is given by:

$$\langle I(Q)\rangle_{NA} = \frac{\varphi}{\langle V\rangle}(\rho_P - \rho_0)^2 \int_0^\infty V(r)^2 f(r) P(Q,r)_{NA} dr \tag{23}$$

where φ is the volume fraction of the polymer given by $\varphi = c/d_0$, and the d_0 is the density of the solution and c is the concentration in $g\, mL^{-1}$. The form factor P(q) for the individual spheres with a given radius, r, is given by:

$$P(Q,r)_{NA} = \left[\frac{3\cdot(\sin(Q\cdot r) - Q\cdot r\cdot \cos{(Q\cdot r)}}{(Q\cdot r)^3}\right]^2 \cdot \exp^{(-Q^2\cdot \sigma_R{}^2)} \tag{24}$$

The corresponding size distribution, f(r), is:

$$f(r) = \frac{1}{\sqrt{2\pi\cdot\sigma_{PD}}} exp\left(-\frac{\left(r - \langle R_p\rangle\right)^2}{2\sigma_{PD}{}^2}\right) \tag{25}$$

Where $\langle R_p\rangle$ is the mean size of the nanoassembly and σ_{PD} is the Gaussian width of the particle distribution. The volume of the nanoassembly is then:

$$\langle V\rangle = \int_0^\infty V(r) f(r) dr \tag{26}$$

Where V(r) is volume that is occupied by the diblock copolymer within the nanoassembly, that has a radius, r, of $V(r) = V(r) = 4\pi r^3/3\cdot$ (1-Φ_0). For the sake of simplicity, the model will not consider the effect of the solvent within the assembly, we assumes that it is independent of the size. The amount of the solvent is given by:

$$\Phi_0 = \Phi_0 = 1 - \frac{M_{NP}}{\langle V\rangle d_p} \tag{27}$$

Where M_{NP} is the average molecular weight of the nanoassembly and d_p is the density of the diblock copolymer. Moreover, the density of the nanostructure can be calculated:

$$n(r) = (1 - \Phi_0)\int_0^\infty \theta\left(r - r' - R_p\right)\frac{1}{\sqrt{2\pi\sigma_R^2}}\exp\left(-\left(r' - R_p\right)^2/2\sigma_R^2\right)dr \tag{28}$$

where the r′ is only considered as a dummy variable. The excluded volume interaction is a common effect for coacervates, where there is a competition between the electrostatic attraction between the oppositely-charged blocks and the local fluctuations within each blob (see Figure 14 for illustration) [65]. Additionally, given the hydrophilic PEO-shell, there are also repulsive forces present between the shells of the nanoassemblies minimizes contact between them and stretches the polymer block outwards. This has a significant effect on the overall confirmation of the nanoassemblies which causes it to swell. By considering the swelling, we include the internal polymer-like scattering phenomenon by adding a “blob scattering” term:

$$I\,(Q) = \langle I(Q)\rangle_{NA} + I(Q)_{blob} \tag{29}$$

We can describe the blob scattering by a polymer-like contribution at high Q and parametrized by a Lorentzian term:

$$I(Q)_{blob} = \frac{I_0}{(1+Q^2\xi^2)} \quad (30)$$

where I_0 a prefactor given with the units of cm^{-1} and ξ is described as a "mesh" size and is given by:

$$\xi \sim f\ x\ g \quad (31)$$

where g is number of repeating units of the charged block inside the blob and f is the charge fraction.

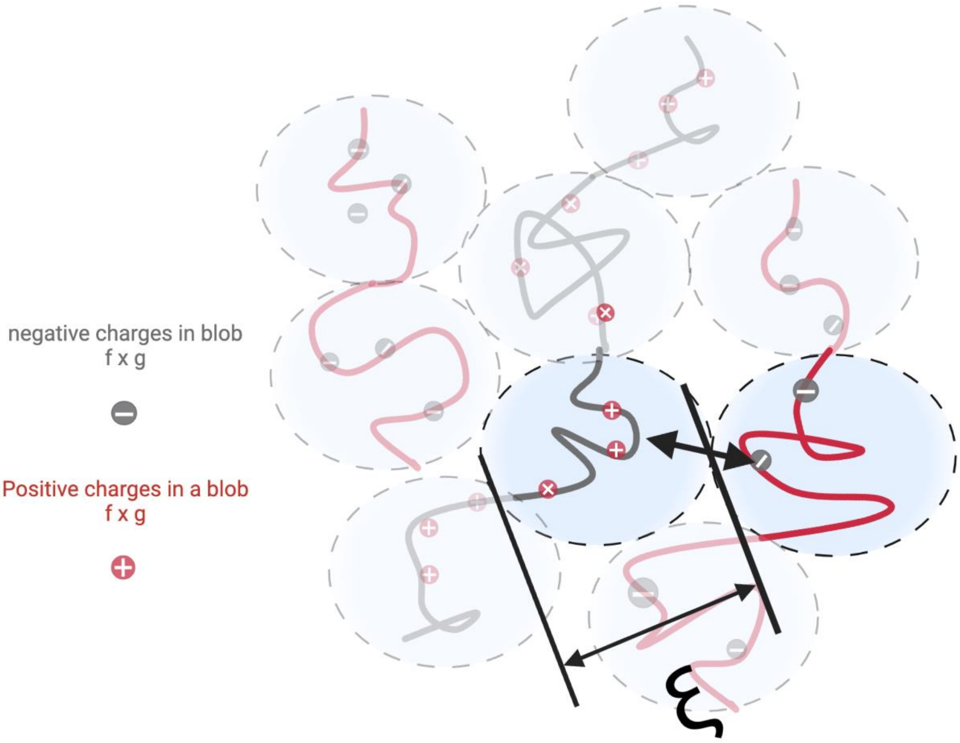

Figure 15. Illustration of the «blob», where the length scale of each blob consist of $f\ x\ g$ charges (i.e., is number of repeating units of the charged block inside the blob and the charge fraction, respectively). This figure is created by the author of this document using BioRender and is based on information retrieved from [65]

2 Aims of the thesis

As described in the introduction of this thesis, the disadvantages associated with colistin can be mitigated by encapsulating the peptide in nanocarriers like block copolymer micelles. However, there is a scarcity when it comes to core-shell assemblies by peptide-polymer conjugates, and in particular the assemblies of peptides assembled with neutral-polyanion DHBC. Moreover, the relation between the release of the peptide and the nanocarrier structure and dynamics is lacking. Therefore, the overall aim of the research presented in this thesis was to develop novel nanomedicines based on the peptide colistin. This includes a systematically investigation of the phase diagram of colistin/PEO-b-PMAA mixtures as a function of pH, charge ratio and total concentration. The overall goal will be to find optimal conditions under which stable core-shell colistin-polymer complexes are formed. In the second part of the project, we will analyze the release and stability of the nanoparticles by using liquid chromatography-mass spectrometry (LCMS). In a collaboration with the department of Bioanalytical Chemistry, the analytical LC method was developed by Harald Røsand Moe. Lastly, the different formulations of colistin-polymer nanoparticles where investigated *in vitro* for their bacterial killing activity against few multidrug-resistant Gram-negative bacteria isolates, which were compared to that of free colistin. This part of the project was conducted in Dr. Håvard Jenssen's lab at Roskilde University, Department of Science and Environment/ Center for Molecular Interactions.

The specific aims were as following:

- Preparation of the nanocomplexes based on the interaction of double hydrophilic block copolymer PEO_{54}-b-$PMAA_{49}$ with the oppositely charged cationic drug colistin.
- Investigate the conformation and nanostructure using small-angle X-ray scattering (SAXS). This includes a systematical investigation of the influence of pH, charge ratio and total concentration on the properties of the co-assembled nanocomplex.
- Investigate the release of colistin from nanoparticles using analytical methods (dialysis and LC-MS).

- Investigate the in vitro antimicrobial activity of the different formulations of colistin-polymer nanoparticles against multidrug-resistant Gram-negative bacteria isolates, such as *Pseudomonas aeruginosa* and *Escherichia coli*.

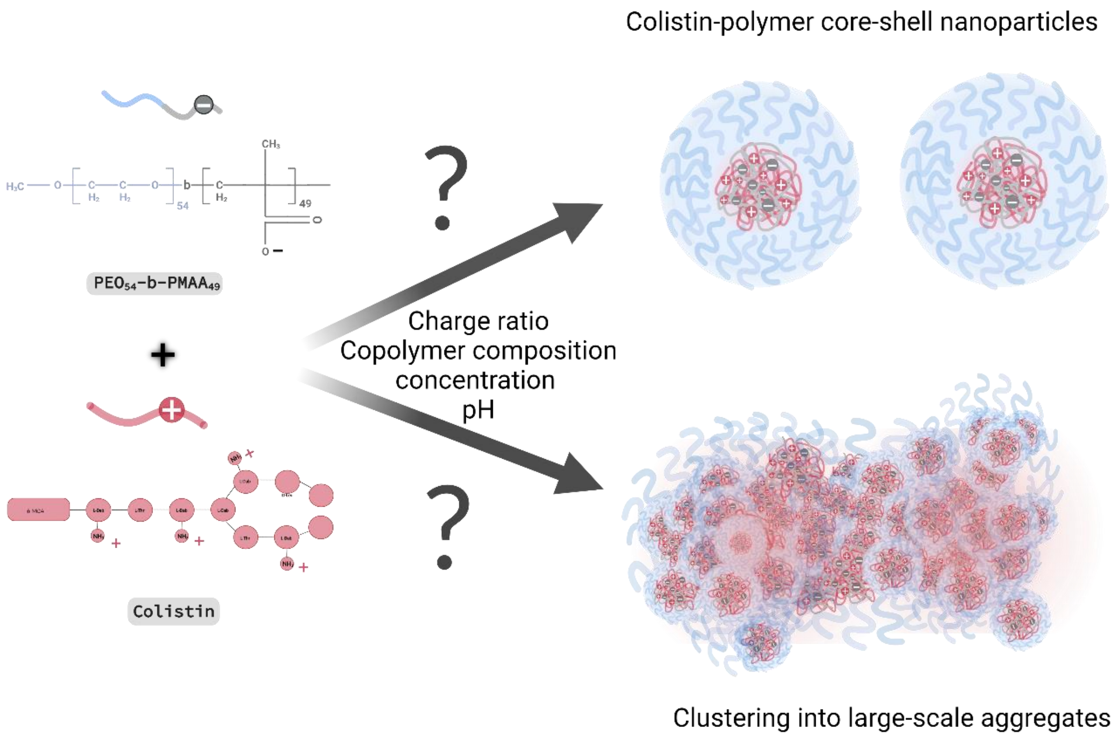

Figure 16. illustration of the self-assembly of cationic antimicrobial peptide and a polyanion-PEO block copolymer into core-shell nanoparticles. The screening of the phase behavior depends on the charge ratio, copolymer composition and concentration

3 Experimental section

3.1 Chemicals, materials, ad equipment

Materials

The copolymer Poly(ethylene oxide)-block-methacrylic acid) (PEO-b-PMAA) with molecular weight PEO_{2000}-b-$PMAA_{1300}$ were purchased from Polymersource Inc (Quebec, CANADA) and stored at -20°C. The copolymer was characterized by a polydispersity index, PDI, of 1.1 (MN/MW = 1.1), where the asymmetry degree was determined by calculating the ratio between the molecular weight of the PEO block and that of the PMAA block of the copolymer. Hence for the PEO_{2000}-b-$PMAA_{1300}$, it was equal to 2000/1300 i.e., 1.53.

Polymyxin E1 sulfate (10 mg, 96.1% purity) were purchased from TOKU-E (Gent, Belgium) and stored at -20°C. Phosphate Buffered Saline (PBS) pH 7.4 (1X) modified, without calciumchloride and magnesiumchlorid, liquid, sterile-filtered was purchased at ThermoFisher Scientific (Oslo, Norway). Type 1 water was obtained from a Milli® Integral water purification system from Merck Millipore (Billerica, MA, US).

For the antibacterial activity, minimum inhibitory concentration

The bacterial strains used where *Escherichia coli* ATCC 25922, *Pseudomonas aeruginosa* H102 Canada (wild type), and *Staphylococcus Aureus* ATCC 25923. Ultrapure water (18MΩcm) was obtained from a Milli-Q® integral water purification system from Purelab flex, Denmark. The broth used was Mueller Hinton II (MH-II) broth (Becton Dickinson BV, Vianen, The Netherlands). The Agar was purchased at Sigma-Aldrich (Lot: BCCD6501).

Consumables

The 96-well polypropylene microtiter plates (Cat. No. 3879, COSTAR) and 96-well Greiner plate were purchased from Sigma Aldrich. Sterile pipette tips, Test tubes (1.5 mL), Falcon tubes (10, 15, 50 mL) and syrringe filter (w/0.2 µm Cellulose Acetate membrane) were purchased from VWR. F1 Finnpipettes with delivery volume ranges of 100-100 µL, 20-200 µL, and 5-40 µL from Thermo Scientific were used. 1000 µL and 200 µL pipette tips were purchased from Sarstedt (Oslo, Norway).

3.1.1 Buffer preparation protocol

Buffer solutions used where Tris (50mM, pH 7.2), citric acid/phosphate (50mM, pH 5.5) and PBS (50mM, pH 7.4). For the citric acid/phosphate buffer (50 mM), 3.55 g sodium phosphate dibasic (Na_2HPO_4) was dissolved in 500 mL Milli-Q water, where 5.75 g citric acid was added afterwards to the solution. The pH was then adjusted by adding small amounts of the buffer component. The approximate pH was determined using the pH strips described in section 4.1. The same procedure where done for the Tris buffer, the amounts of the buffer components required is given in Table 1.

Table 1. The amounts of the buffer components to make citric acid/phosphate buffer (50mM pH 5.5) and Tris buffer (50mM, pH 7.4).

Component	Amount (g)
Sodium phosphate dibasic $\mathbf{Na_2HPO_4}$ (mw: 141.96 g/mol)	3.55
Citric acid monohydrate $\mathbf{C_6H_8O_7 \cdot H_2O}$ (mw: 210.14 g/mol)	5.76
Tris $\mathbf{C_4H_{11}NO_3}$ (mw: 121.14 g/mol)	30.29
Hydrochloric Acid HCl (mw:36.46 g/mol)	7.66

3.1.2 Preparation of pure polymer and colistin solutions, and encapsulated colistin solutions

Solutions of the free PEO_{2000}-b-$PMAA_{1300}$, free colistin and their complexe PEO_{2000}-b-$PMAA_{1300}$/colistin, were prepared at different charge ratios which corresponds to their total charge at given pH. For the first sample PEO_{2000}-b-$PMAA_{1300}$ copolymer solutions were prepared at 3.3 mg/mL and the colistin concentration was either 2.8, 5.7 or 11.3 mg/mL (see Table 2). Total charge was calculated on the basis of the copolymers and colistin's molecular weight, pKa and number of carboxylic groups of TA and amines of colistin at given pH (Table 2). The mixture was prepared by two different methods, 1) the polymer was dissolved in a 1 mL PBS solution, and 5.7 mg colistin was added directly to the solution, and 2) the two components were dissolved separately in a 1 ml PBS, and where mixed together after 2 hours of being shaken at room temperature. For both methods the mixtures were prepared by adding the same volume of the two components to have a ratio of charges, R = [NH2]/[COOH], of 1. This charge ratio was changed by decreasing and increasing the concentration of colistin (2.83 mg/mL and 11.4 mg/mL, respectively). The final concentration of the PEO_{2000}-b-$PMAA_{1300}$ and colistin in the micellar suspensions was 9, 6.1, 14.6 mg/mL). All of the suspensions were gently shaken at room temperature overnight in a rotator (Labroller®, Labnet, USA) and stored at 4 ◦C until use.

Table 2. Calculations that were used when making polymer-drug samples for colistin and PEO-b-PMAA. For pH 7.4, the charge ratio Z, corresponds to 1:1 for a concentration of 9 mg/mL.

	compound	m (mg).	MW	n (mmol)	eq	Charge	Number of charges	charge ratio, Z
Solvent	PBS pH7.4 1M	N/A	N/A	N/A	N/A	N/A		
Polymer	PEO_{54}-$PMAA_{49}$	3,3	6600	0,0005	1	(-1)	49	
Sample 1	Colistin sulphate	0	1155	0	0	(+5)	0	
Sample 2	Colistin sulphate	5,66	1155	0,0049	9,8	(+5)	49	1
Sample 3	Colistin sulphate	2,83	1155	0,00245	4,9	(+5)	24,5	2
Sample 4	Colistin sulphate	11,32	1155	0,0098	19,6	(+5)	98	0,5

3.2 Small Angle X-ray Scattering

Most of SAXS experiments carried out in relation to this work were conducted at beamline BM29 BioSAXS, located at the European Synchrotron Radiation Facility (ESRF) in Grenoble, France. In the following sections, a comprehensive overview of the instrument set-up, specifications, and the data treatment procedures will be presented.

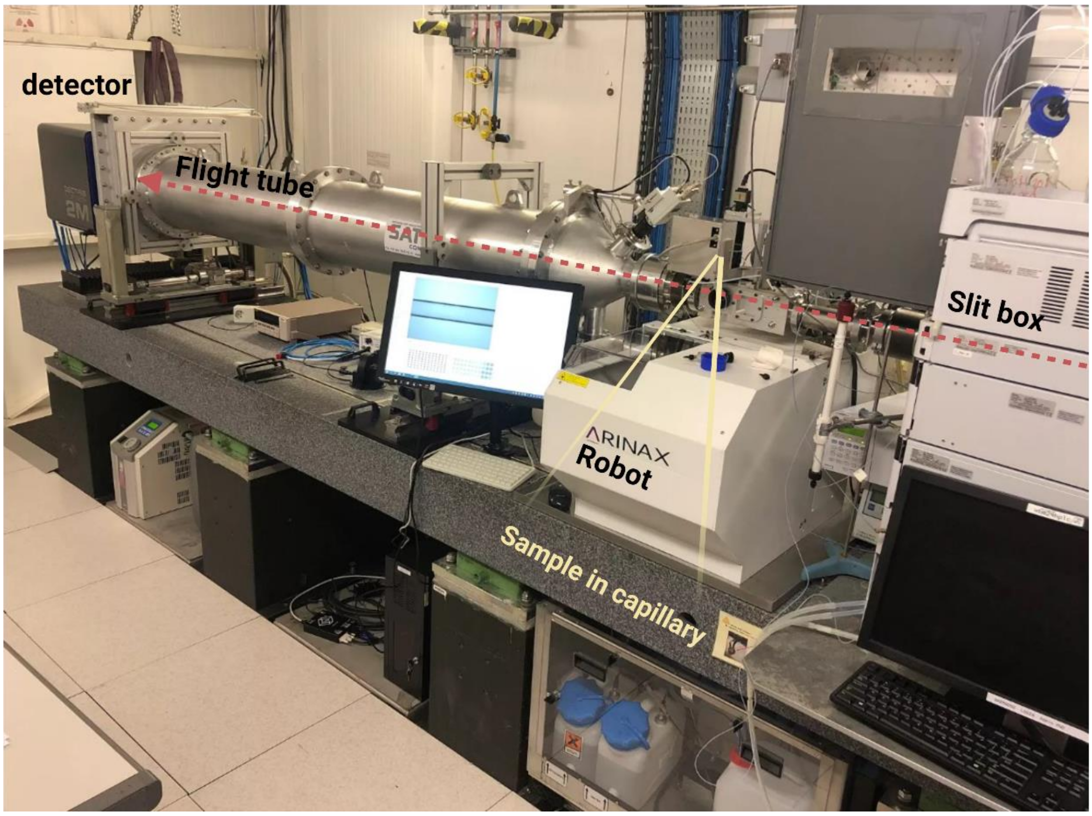

Figure 17. Picture of the setup for the BM29 BioSAXS instrument at ESRF, the image is depicted from the ESRF website. The image shows an overview of the optics.

The setup of the beamline is shown in Figure 18. The synchrotron produces a high X-ray beam that goes through multiple slits with different purposes to create highly monochromated beam with a pinhole configuration. The spacing between the sample and detector is a fixed distance of 2. 96 nm. The instrument possesses a moveable detector with three sample-to-detector distances yielding a combined q-range of $0.025 - 6\,nm^{-1}$ which corresponds to a maximum detectable size of 200 nm. This makes it ideal for studying the structures of micelles, which have a size of roughly 10-30 nm. The sample handling system automatically injects the samples into the exposure cell, which is a 1.8 mm thick quartz glass capillary. The sample continuously flows through the capillary during the measurements, where 10 frames of 0.02 s was performed for each samples. This was to minimise radiation damage, and therefore the 10 obtained frames was tested and detected by changes in the scattering pattern which exceeds a calibrated threshold, relative to the first frame. Alle frames with radiation damage were neglected for further analysis. In case of strong radiation damage, the exposure time, flow speed and attenuation were changed accordingly. The PEO-b-PMAA/colistin samples were run at 20^{o}C, and the buffer was measured before and after each sample.

3.2.1 Data analysis

The primary data obtained from a scattering experiment is the 2D detector image. There are several treatment steps which are common for the instruments that must be performed on the raw detector images before the data can be used in analysis. First, the pixel data must be scaled according to the data collection, transmitted intensity and incident beam intensity. Unwanted pixels such as beamstop, intermodulus gaps, and hot pixels are removed by using a mask, leaving only the scattered beam. Typically, this is achieved by calibrating with a homogeneous scatterer such as glassy carbon.

The 2D pattering contains more data than necessary, and can be reduced by azimuthal integration (radial averaging) of every frame, yielding a 1D image. This is done by taking an average of all pixels at a given radius $r_{det} = d_{detector} \cdot \tan\theta$, where $d_{detector}$ is the detector distance and θ the scattering angle, the average of every pixel in that area is taken. This expression is found from geometrical considerations, and the center of the radius is found from direct beam measurements. The average scattering vector ⟨Q⟩ is calculated for each radius and is given by

$$\langle Q \rangle = \frac{4\pi sin\langle \theta \rangle}{\langle \lambda \rangle} \tag{31}$$

As seen from this equations, one needs the calibrated wavelength of the X-rays, beam position and sample-to-detector distance. These steps yields the scattered intensity from the sample as a function of Q.

After the radial averaging, one must convert the data to an absolute scale to obtain the absolute intensity of the sample. For this, the data must be background corrected by subtracting the background and normalising the date. The background scattering comes from the buffer, capillary and other sources. After subtraction we are only left with scattering coming from the particles of interest and the excluded volume. Normalisation of the flux and the instrumental setup is done by using a internal standard with a known differential scattering cross-section $\frac{d\Sigma}{d\Omega}$ and thickness d_{st}. During our measurement at BM29, the internal standard used is water at 20°C, which has a differential scattering cross-section of

$$\frac{d\Sigma}{d\Omega}(Q) = (Q = 0) = 1.632 \cdot 10^{-1} \tag{32}$$

By measuring the scattering from the empty cell with and without water, we can calculate an absolute intensity which is independent of the instrument used and allows for the comparison of scattering data with data obtained from other instruments. The differential scattering cross section per unit volume is given by

$$\frac{d\Sigma}{d\Omega}(Q) = \frac{\frac{d\Sigma}{d\Omega}(\vec{Q})}{\left(\frac{I_{st}(\vec{Q}) - BG_{st}}{d_{St} T_{st+cell}}\right)} \cdot \frac{I_{st}(\vec{Q}) - BG_{s}}{d_{s} T_{s+cell}} \tag{33}$$

where I_s and I_b are the measured intensity of the sample and standard respectively, d_s and d_{st} are the thicknesses of the sample and standard, T_{s+cell} and $d_{st+cell}$ are the transmissions of the sample and standard in the cell respectively, and BG_{st} and BG_s are the background scattering.

At last, since the sample are measured at several frames, radiation damage may occur causing altered scattering, especially at low q-values. The software at BM29 compares the frames, and detects radiation damage. Frames that deviates with more than a certain amount from the average are removed. The final scattering data was obtained by subtracting the scattering from the buffer with the sample. The software at BM29 was used to remove some of the radiation damage for the samples of PEO-b-PMAA/colistin, other than that the rest of the samples were subtracted by using BioXTAS RAW software.

The final step is to analyse the final scattering data qualitatively and quantitatively. For quantitative analysis, the analytical model introduced in Section 1.5.4 was programmed using C++ in the QtiKWS software developed by Vitaly Pipich. Typically, the Nelder-Mead simplex algorithm was used as a fitting algorithm, however it is sensitive to local minima, so in these cases it was supplemented with the Levenberg-Marquardt algorithm. The size-polydispersity was calculated with a built-in option which uses Gaussian distribution of the radii.

In addition, we carried out Indirect Fourier Transform calculations and fittings of the small angle scattering data using the PRIMUS software package, which utilizes the GNOM program. For this analysis, we employed the "arbitrary monodisperse" system, which covered the full q-range and utilized around 200 splines. If the automatically chosen parameters failed to yield a satisfactory fit to the data, we manually varied the D_{max} parameter until an acceptable fitting was achieved.

3.3 Drug release study

In order to investigate the results of colloidal stability study, the in-vitro release of Colistin from their corresponding complexes was studied at pH level of 7.4 For this experiment we could also evaluate the coacervate micelles ability to disassemble at acidic pH (endosomal pH) in order to release the entrapped drug. The micelles prepared according to the previously described protocol were assessed in buffer solution with different pH . Briefly, freshly prepared polymer/colistin complexes were dispersed in 1 mL of phosphate buffer (pH 7.4, 10 mM), citrate buffer (pH 5.5, 50 mM) or Tris buffer (pH 7.4, 50 mM). The micelles were transferred into 10 mL dialysis bags (MWCO 3500 kDa) in 1L Milli-Q water at 37 ◦C. The polymer solution inside the bag was sampled around at different timepoints (2h, 5h, 10h, 24h etc.) The drug concentration in the nanoparticle was determined using HPLC.

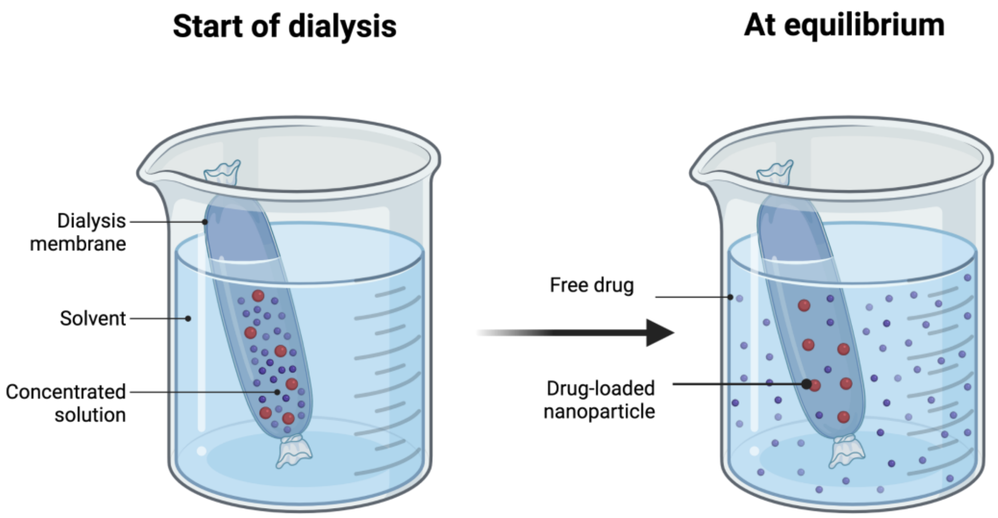

Dialysis is a biochemical method that allows the separation of small molecules from a mix of different size molecules. The sample is added to a dialysis membrane that has a specific pore size, in these studies a membrane of 3.5 kDa was used. Small molecules diffuse through the pores into the solvent and bigger molecules remain in the membrane.

Figure 18. The process for performing dialysis on the complexed sample. This figure is created by the author of this document using BioRender, where information on the Figure is provided by BioRender (included the text below the illustration).

3.4 Antimicrobial activity assay

3.4.1 Spot plating technique

The spot plating technique is a method used to quantify the amount of bacterial numbers of the bacteria, and also the antibacterial activity of the antimicrobial again those pathogens. This is done by the agar overlay technique, which is demonstrated in Figure 19. Where a serial dilution of each bacterial suspension was made with MH broth media for the two-bacteria E. coli and P. aeruginosa. From this overnight culture (ON), the bacterial culture was first diluted at 1:500 to obtain bacterial inoculum ranging between 2 − 8 · 10 cfu/mL. When this was achieved 10 µL of each dilution was spotted on the MH broth agar plates (Figure 20). The agar plates were incubated for 24 h in 37°C.

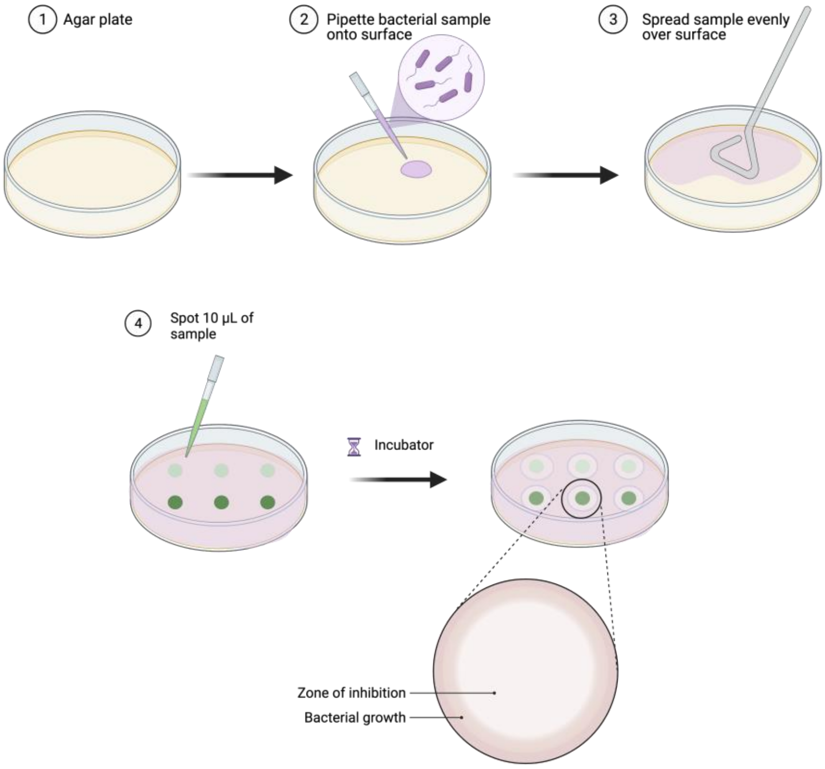

Figure 19. Agar overlay technique demonstrates the antibacterial activity of colistin Sulphate. This figure is created by the author of this document using BioRender.

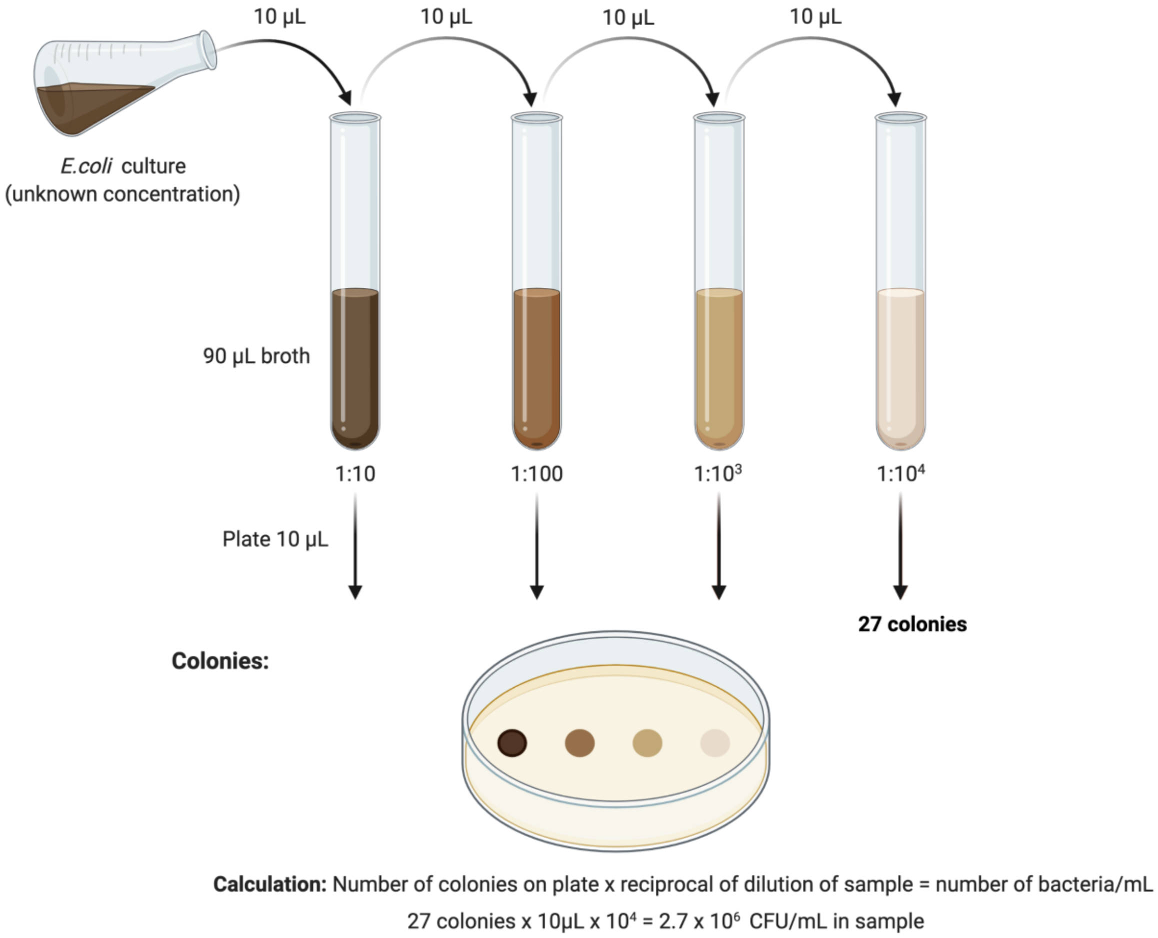

Figure 20. Spot plating technique to quantify bacterial numbers of E.coli. The bacterial culture was diluted at 1:500 to obtain bacterial inoculum ranging between 2 – 8 · 10 cfu/mL. This figure is created by the author of this document using BioRender, where the information on the Figure is provided by BioRender.

3.5 Minimum inhibitory concentration (MIC)

The antimicrobial activity of free colistin and co-assembled colistin was tested using a serial dilution titration method, to determine the peptides minimal inhibitory concentration (MIC) against two different pathogenic bacterial strains: Escherichia coli ATCC 25922, Pseudomonas aeruginosa H102 Canada (wild type). The MIC assay was performed in sterile 96-well polypropylene microtitter plates). Overnight (ON) cultures were prepared by using autoclaved media of Mueller-Hinton (MH) Broth (typically 5 mL) and these were left over at night at 37°C in a water bath with shaking. The next day, the ON culture was diluted 1:50 in fresh MH broth that was usually stored at -4°C , this is depicted in Figure 21.

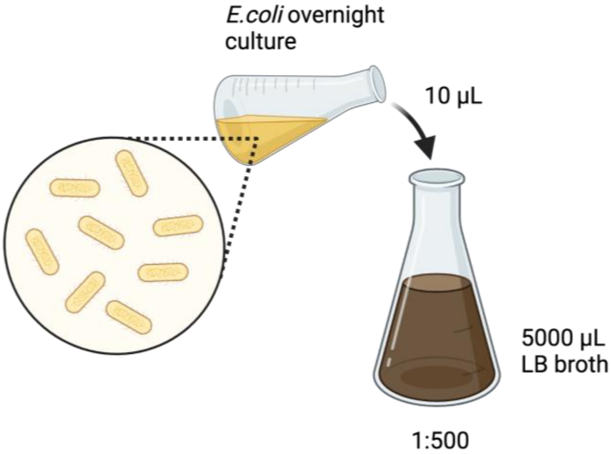

Figure 21: Spot plating technique to quantify bacterial numbers of E.coli. This figure is created by the author of this document using BioRender, where information on the Figure is provided by BioRender

The optical density (OD) of the samples was measured at a wavelength 600 nm on the spectrophotometer. The desired OD was 0.4 nm, the ON culture of E. coli and P. aeruginosa were allowed to grow until they reached an OD of 0.4 (this could take more than 6 h of incubation with 37°C with shaking). The bacterial culture was diluted again at 1:500 to obtain bacterial inoculum (concentration of the bacteria) ranging between 2 − 8 · 10) cfu/mL, see Figure 22 for the description of the process.

For the MIC assay, we tested the activity of free colistin, co-assembled colistin with polymer into nanoparticles, and released colistin from the nanoparticle that was obtained from the drug release study. The plate was prepared by adding 10 µL serial dilution of the compounds and 90 µL of the bacterial suspension. A positive control was the 1:500 bacterial culture and MH broth was used for sterility control (negative control) and growth control was bacterial suspension. The microtitter plate was then sealed and placed at 37°C for 24 hours approximately. The MIC concentration was determined by the lowest concentration with no visible growth after being incubated for 24 hours. For a detailed description, see Figure 22. The MIC results are given as the median value of three experiments.

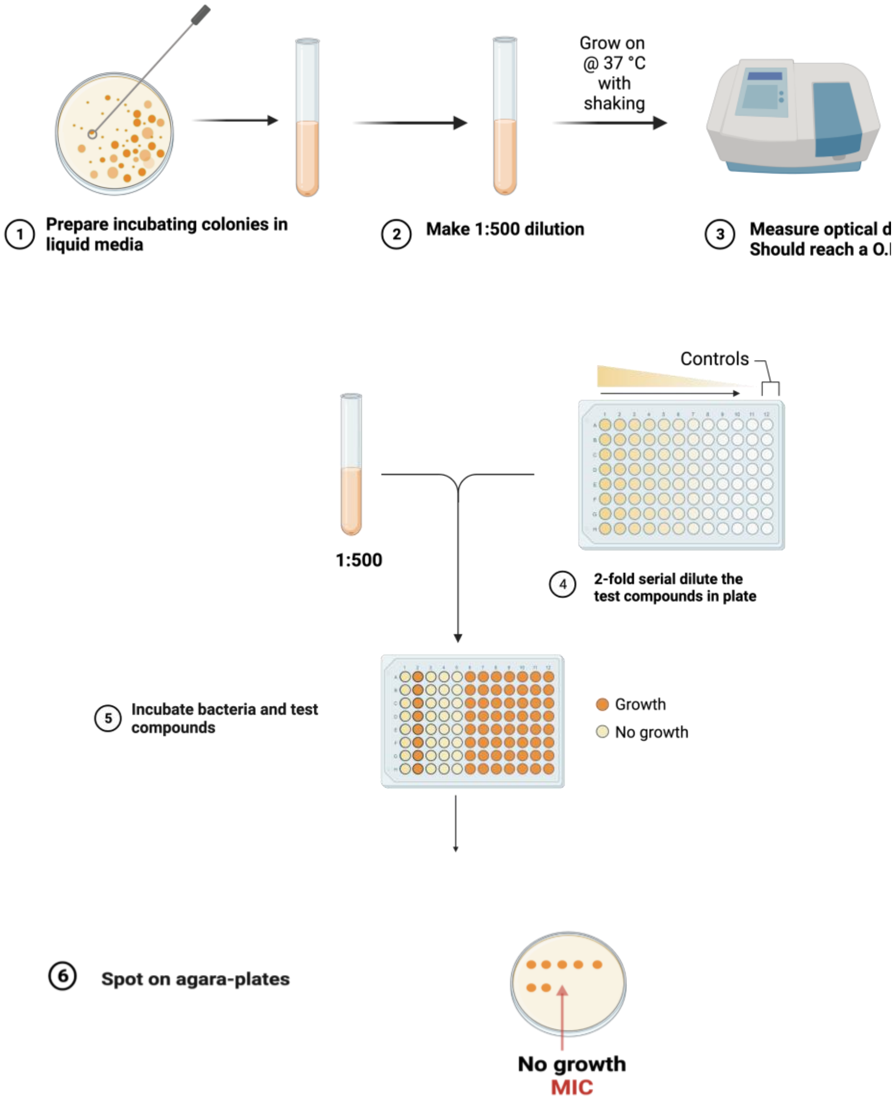

Figure 22. Minimum Inhibitory Concentration (MIC) of colistin against E.coli and Pseudomonas Aeruginosa.

4 Results and discussions

The overall aim of the study was: can we encapsulate colistin in PEO-b-PMAA polymer matrices through coacervation to obtain active colistin nanoparticles. A major part of the study was therefore dedicated to developing methodologies to obtain stable peptide-polymer coacervates and physiochemical characterization of these using scattering methods. Subsequently, to evaluate the performance of PEO-b-PMAA polymer as a drug delivery system for colistin, the antimicrobial properties, drug release kinetics and cytotoxicity of the peptide-loaded nanoparticles have been investigated.

The results are arranged in chronological order, beginning with the structural characterization of pure colistin and polymer in aqueous solution. Following that, an in-depth characterization of colistin-polymer coacervates is presented, as well as the small-angle scattering structural model used to fit the scattering pattern of coacervates micelles. In addition, the findings of drug release studies will be discussed in detail. The final section of this thesis will discuss the preliminary assessment of the antimicrobial activity of the coacervates micelles against a variety of bacterial cultures and compare the results to those obtained with free colistin to determine if there were any differences in antimicrobial activity between free and complexed colistin.

4.1 Structural characterisation of Pure Polymer and Colistin Solutions

The core focus of this thesis lies in the comprehensive structural analysis obtained using SAXS. For the pure diblock copolymer, PEO_{54}-b-$PMAA_{49}$, and colistin the Beaucage model presented in section 1.6.1 was used to fit our experimental SAXS data, this sections that follows a detailed explanation of the fitting process is explained.

The scattering curve shown in Figure 23 indicates which structural features of the micelles contribute to which features of the scattering curve. Typically in the low Q-region (also known as the Guinier region), the scattering is primarily influenced from structures around 10-100 nm. In this area we get an idea about the size and polydispersity in the sample, and is characterised by the radius of gyration (R_g). Moving to the middle Q-region, referred to as the Porod region, we get details on the structure and shape the gradient. Finally, the high Q-region provides information about the radius of the core of the C3Ms (R_{core}).

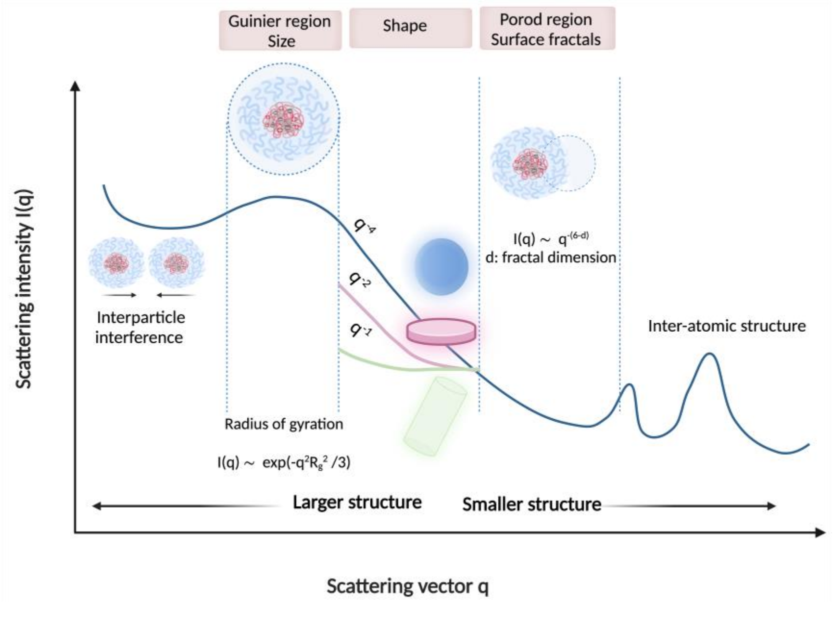

Figure 23. Illustration of the whole scattering curve for two interparticle interaction potentials. The very low q region contains information about interparticle interactions among two particles. When the intensity reaches a plateau (Guinier regime) in the low Q regime, the overall size (R_g) of the particle can be determined. The Porod law describes the relationship between the slope of ln I(q) vs. ln (q) and the fractal dimension of the scattering particle.

4.1.1 Structural characterisation of PEO_{54}-b-$PMAA_{49}$

The Beaucage model was performed to investigate the structural evaluation of the pure diblock copolymer. In Figure 24 a), the scattering curve is shown for the pure PEO_{54}-b-$PMAA_{49}$ diblock copolymer in PBS solution, where the concentration of the diblock copolymer is 0.5 mM. The black line that goes through the scattering data is a representation of the model used to fit the data. In comparison with the generalized polymer-like scattering model, Equation 23 in Section 1.6.2, it is shown that PEO_{54}-b-$PMAA_{49}$ is nicely described with this model. From this model we can extract a number of parameters, which can quantitatively describe the scattering curve. The parameters used to produce the curves can be seen in Table 20 in the Appendix Section 6.3.

All scattering curves exhibited a clear Guinier-liker regime at low Q-values, however, they also had an upturn at lower values ($Q < 0.01$ Å^{-1}) , showing that the polymer solution is not completely homogeneous, which is an indication of the formation of larger clusters. If this was not the case, one would expect a plateau-like behavior at the lowest Q-values which is not observed. However, by diluting the diblock copolymer concentration it was observed that the steep declines with lower concentration. It is probably because at lower concentrations the interactions between the diblock copolymer and solvent are decreased. It is important to note that the clustering might arise from other intramolecular interactions such as hydrogen binding, van der Waals forces or hydrophobic interactions. This can also be seen in Figure 24, where the concentration of the diblock copolymer used where 0.5, 0.4, 0,3 and 0.1 mM. These interparticle interactions were taken into consideration into the fitting model by using a second virial coefficient, A_2, which was adjusted by the fitting algorithm until an optimal fit was found. Moreover, for the high Q-values we observe that the anionic polyelectrolyte has a polymer-like scattering with a smooth decay of Q dependency of Q^{-2}. Also the radius of gyration, R_g, can affect the scattering curve in this region. The extracted Rg values from the model were 18, 20, 22, 21 nm for concentrations of 0.5, 0.4, 0.3 and 0.1 mM respectively. Indicating that R_g values is inverse proportional with the concentration, where a higher concentration gives a lower R_g value.

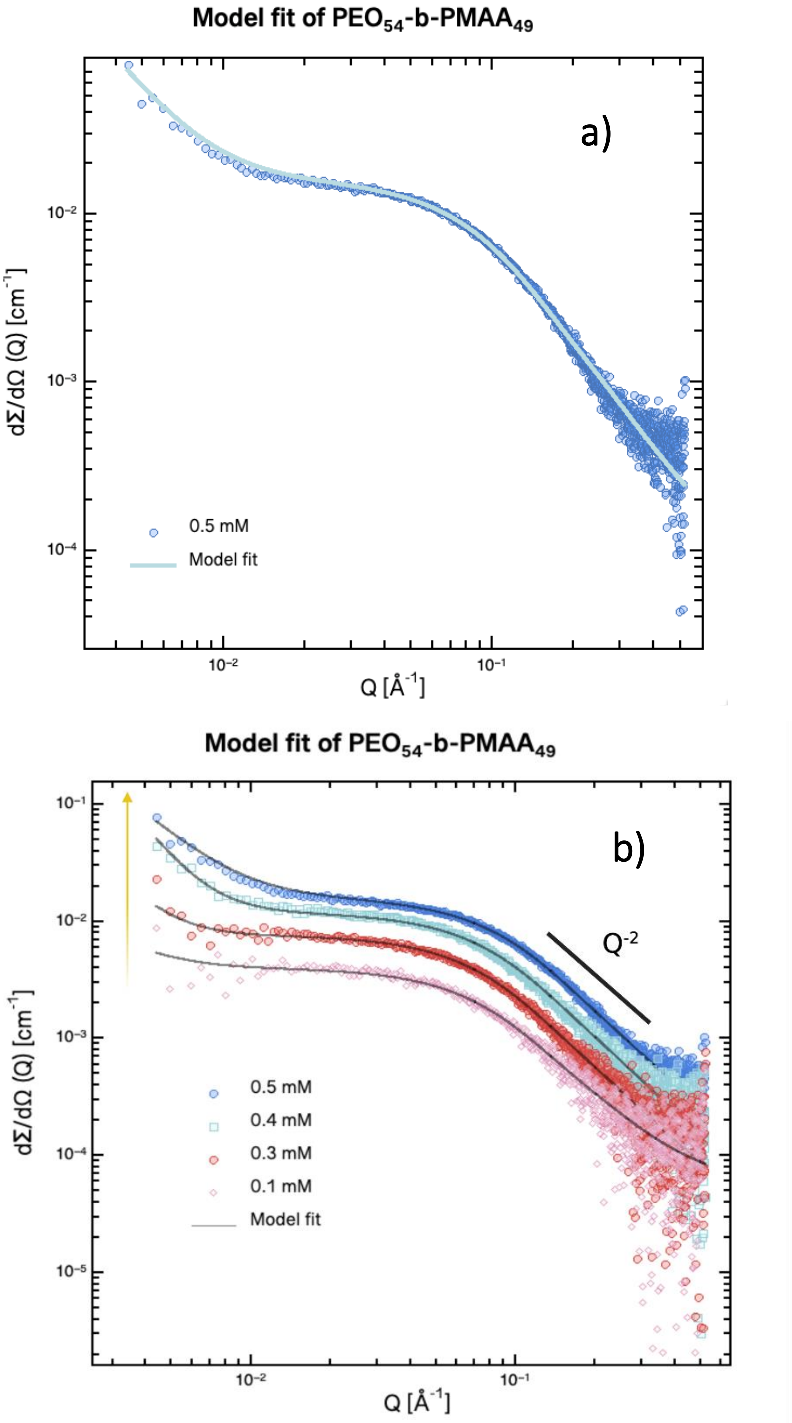

Figure 24. SAXS intensity as a function of the modulus of the scattering curve, Q, of a) PEO_{54}-b-$PMAA_{49}$ diblock copolymer at concentration 0.5 mM (3.3 mg/mL), b) PEO_{54}-b-$PMAA_{49}$ diblock copolymer at concentration of 0.5, 0.4, 0.3, 0.1 mM. The blue and black curve in both a) and b) respectively represents the Beaucage model fit.

4.1.2 Structural analysis of pure colistin

Like PEO_{54}-b-$PMAA_{49}$, Colistin was dissolved in PBS solution and the same model was used to fit the scattering data. The observed scattering curves for Colistin resembled the scattering curve for the diblock copolymer, where at low Q-values it had an increase in the steep of the scattering. Unlike the diblock copolymer, we used a higher concentration for the Colistin samples, and also made sure to dilute them down. *Figure 25* shows the scattering curves with its corresponding fitted model at concentrations of 10, 8 and 2 mM. The corresponding R_g values where found to be 6.22, 6.19 and 5.99 nm. Meaning that the concentration did not have any effect on the R_g values as it did for the diblock copolymer. The parameters used to produce the curves can be seen in Table 6 in the Appendix.

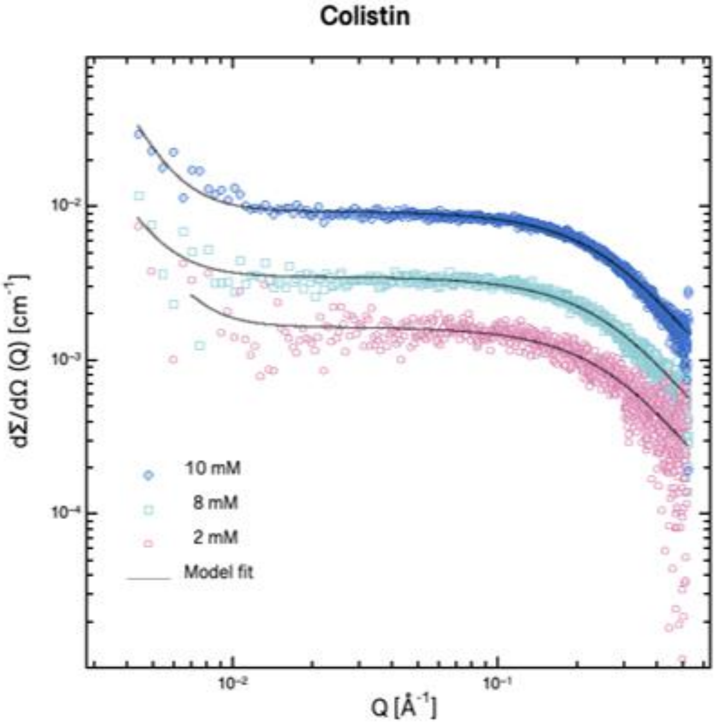

Figure 25. SAXS intensity as a function of the modulus of the scattering curve, Q, of Colistin at concentration 10, 8 and 2 mM. The black curve represents the Beaucage model fit.

4.2 Analysis of the scattering curves for the formation of C3Ms by complexation between PEO-b-PMAA and Colistin

The investigation of the formation of core-shell coacervates formed by the anionic block-copolymer, PEO_{54}-b-$PMAA_{49}$, and the cationic polyelectrolyte, Colistin, was one of the most important aspects of this thesis. The core of these coacervates consist of interpolymer electrostatic coacervates of Colistin and the PMAA block and the outer shell is composed of the PEO blocks. It is this PEO block that stabilises the coacervates against aggregation and macroscopic phase separation by steric repulsion. From the study done by Atman et al. [48], they found that typically coacervates aggregate to clusters, which subsequently redistribute into stable spherical core-shell particles. In this study and many other studies on nanostructures that were formed by self-assembly of oppositely charged polyelectrolyte it was used spherical core-shell model. With the theoretical knowledge we had, we attempted to use the same model for the data we obtained for our samples given that we did form coacervates. Interestingly, the core-shell model was not able to produce fits which overlapped satisfyingly to the experimental data. An attempt was to vary the parameters manually and perform the fit procedure using a different code to rule out potential sources of error, but this also failed to describe the data. It was suspected that Colistin might not be as stable as once thought, despite this not being reported in the most published articles on Colistin. A deep look at this gave surprising results that Colistin was neither stable at low temperatures nor inert against surfaces. However, the scattering pattern that we obtained throughout the work in thesis showed to be reproducible and stable over time. This hypothesis had to be ruled out, but was taken considerably into consideration during the rest of the work. While micelles or clustered structures might be present, the failure of the core-shell model to explain the data can be explained by the presence of other large structures in the solution which dominate in the scattering signal.

Unfortunately, it was not until the final month of my thesis that we arrived at the implementation of a generalized model to accommodate a portion of our data. For us the most important aspect was that we could present and documentate the formation of nanocomplexes arising from colistin and PEO_{54}-b-$PMAA_{49}$. Moving further in the subsequent analysis, we will present the scattering curve for a mixed solution along with the corresponding fitted parameters. However, we cannot present the fitted model for the remaining scattering curves collected during this thesis. Nevertheless, it is noteworthy that the majority of these curves exhibited reproducibility, and we can deliberate on the observed changes in the data through comparative analysis.

In general, for this model the intensity for the particles can be written as:

$$I_0 = c/dp \cdot 10^{-3} \cdot M_w \cdot (\rho_{NP} - \rho_0)^2 / N_{avo} \tag{34}$$

where M_w is the molecular weight of the nanoparticle, c is the concentration of the solution containing both Colistin and PEO-b-PMAA, dp is the density of the polymer, N_{avo} is Avogadro's number, and ρ_{NP} and ρ_0 is the scattering length density of the polymer and solvent respectively.

Figure 26 illustrates the scattering patterns of pure Colistin and pure PEO_{54}-b-$PMAA_{49}$, each at concentrations of 2.8 mg/mL and 3.3 mg/mL, respectively. Additionally, the scattering pattern of the mixture of these two components, which forms polyelectrolyte coacervate micelles, is also presented. Before delving into the analysis of the coacervate micelles, it is worthwhile to briefly compare the scattering curves obtained in Sections 4.1.1 and 4.1.2 with those of the pure Colistin and pure polymer blocks. The scattering curve in Figure 26 for Colistin, a more plateau-like behavior is observed at lower Q-values, in contrast to the upward trend seen in Figure 25. This discrepancy suggests the absence of aggregation in this particular sample, but rather the presence of free Colistin chains. On the other hand, for PEO_{54}-b-$PMAA_{49}$, although some upturn of scattering at lower Q-values is still observed, it is not as pronounced as depicted in Figure 24.

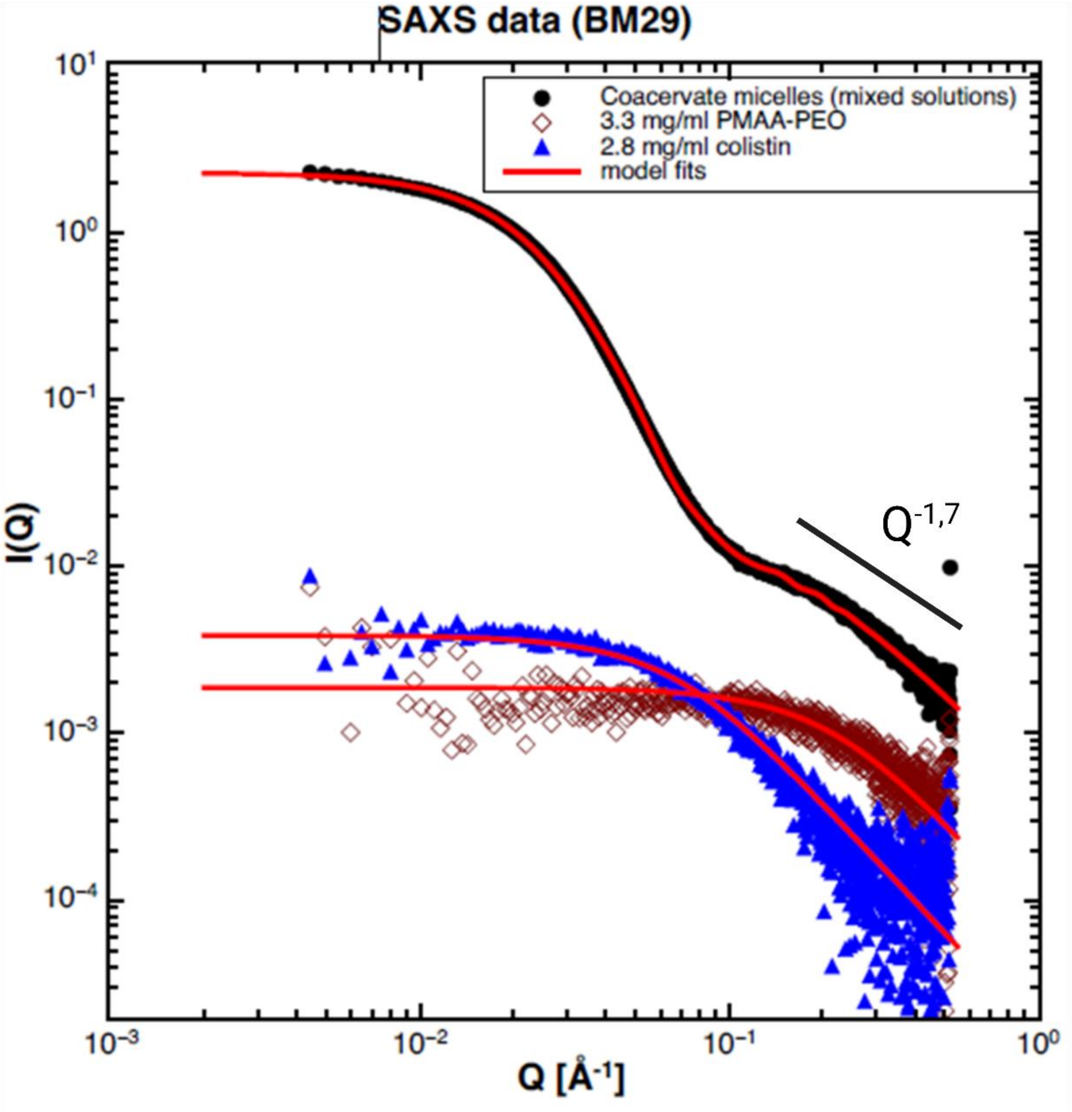

Figure 26. Black curve indicates SAXS profile of polyelectrolyte coacervate formed by Colistin and PEO-b-PMAA, whit a concentration of 2.8 mg/mL and 3.3 mg/mL respectively. The blue curve is the SAXS profile for pure Colistin at 2.8 mg/mL, and the brown cure is the SAXS profile for pure PEO-b-PMAA at 3.3 mg/mL. The red line is the Model fit that was used to fit to our scattering data.

Moving to the analysis of the coacervate micelle depicted in Figure 26, the shape of the scattering curve display typical features of spherical aggregates. Notably, a significant enhancement in scattering intensity is observed at lower Q-values when compared to the scattering profiles of the individual polyelectrolytes. Conversely, at higher Q-values, the scattering intensity follows a power law decay with an exponent of $Q^{-1,7}$, indicative of polymer chain scattering behavior in both the coacervate core and corona. This behavior aligns with the anticipated scattering patterns in a good solvent environment. In the subsequent section, we will investigate the impact of stoichiometric variations on the scattering profile of the coacervate micelles, as depicted in Figure 26.

4.3 The effect of stochiometric charges

Various trends can be observed when different amounts of Colistin and PEO54-b-PMAA49 are combined. In Table 3 we have kept the PEO_{54}-b-$PMAA_{49}$ concentration constant at 3.3 mg/mL, while increasing the Colistin concentration with 2.8, 6.9 and 13.8 mg/mL. For sample 1 it is considered that the final coacervate has a net charge of zero, meaning that all charges on the polyelectrolyte chains are neutralized by the oppositely charged polyelectrolyte. While for sample 2 and 3, the net charge will be negative and positive respectively. Than the total aggregation number N_{agg} is simply the sum of positively and negatively charged polyelectrolyte chains forming the coacervates.

Figure 27 shows the SAXS profiles from coacervates by the variation of Colistin concentration, where $Z < 1$ (pink graph) describes the system at excess of negative charges on these aggregates. It is said that C3Ms is formed during the so-called preferred micellar composition (PMC), which corresponds to mixing ratio of 1:1 where there is an equal amount of positive and negative charges. This is shown for the grey graph, where $Z = 1$. Further by increasing the excess of positively charged species, $Z > 1$ (blue graph) it is believed that C3Ms dissociate into singular polyelectrolytes again. However, we can observe this phenomena for our samples. This believed is because the difference in negative charges are not large enough, in this case we have to have larger difference between Colistin and PEO-b-PMAA.

Table 3. Concentrations of pure Colistin and PEO_{54}-b-$PMAA_{49}$ for the scattered curved shown in Figure 27, and sample 1 describes also the black curve in Figure 26.

	Concentration Polymer mg/mL	Concentration Colistin mg/mL	Total concentration mg/mL
Sample 1	3.3	2.8	6.2
Sample 2	3.3	6.89	10.19
Sample 3	3.3	13.78	17.08

Table 4. Fit Parameters of Polyelectrolyte Coacervates for the Generalised Core-shell model

	N_{agg} Polymer	N_{agg} Colistin	N_{agg} Total	R_g nm
Sample 1	9.55E+00	2.67E+02	2.76E+02	7.89+01
Sample 2	3.46E+00	2.38E+02	2.41E+02	111.7
Sample 3	7.87E-01	1.08E+02	1.096E+02	84.63

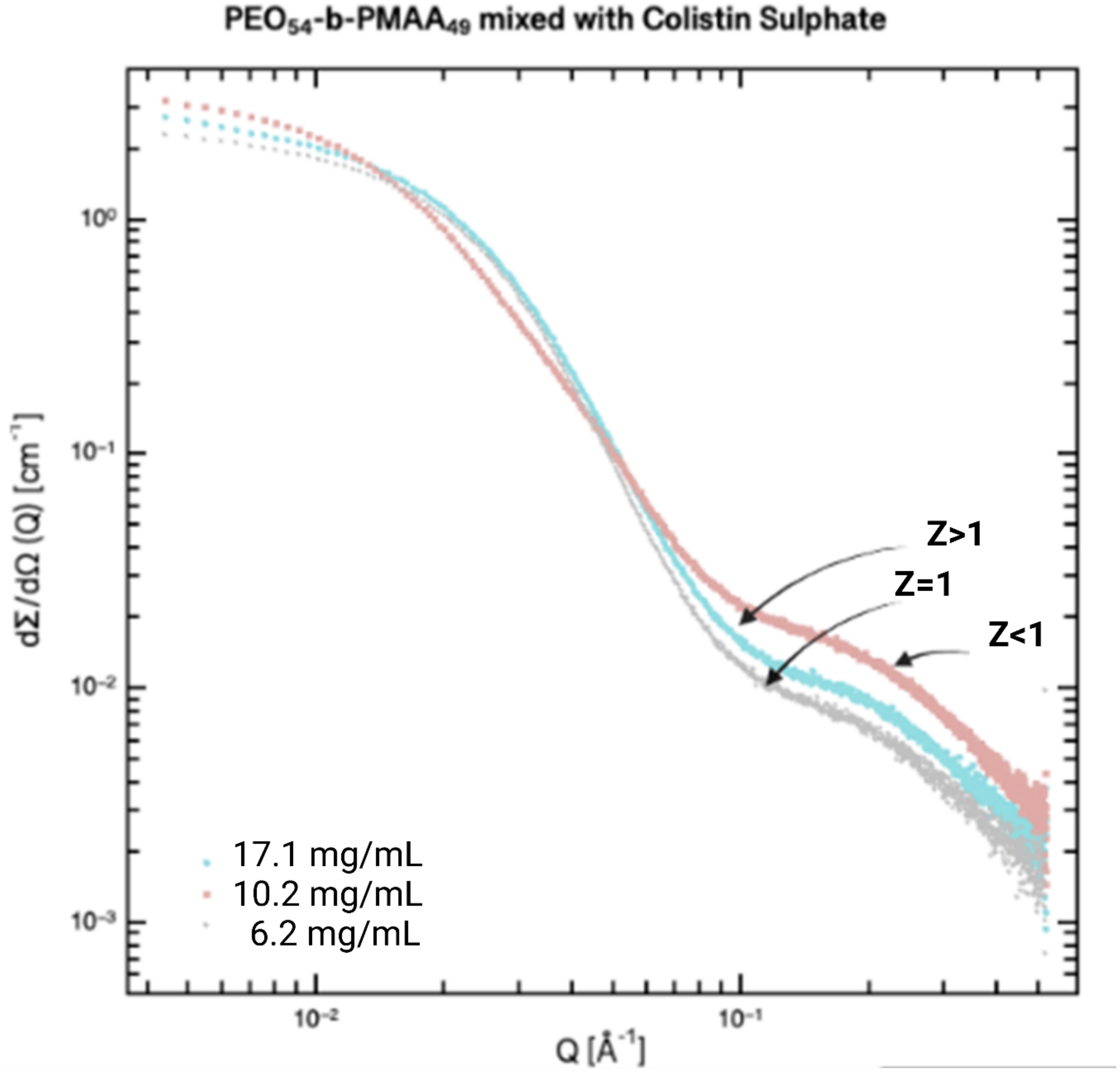

Figure 27. The scattering curve for mixture of Colistin with PEO-b-PMAA, where PEO-b-PMAA had a constant concentration of 3.3 mg/mL and the Colistin concentration was 2.8, 6.9 and 13.8 mg/mL. The Z ratio is an indication of the charge balance in the sample, where Z=1 indicates that the positive charges are equal to the negative charges presents. While Z<1 indicates that there is an excess of positive charges, and Z>1 has an excess of negative charges.

To gain insights into the charging behavior and the concentration range at which Colistin-Polymer Coacervate Micelles (C3Ms) form, we conducted experiments using various polymer-to-colistin ratios. The calculations behind the ratios are given in Appendix 6. Figure 28 illustrates the results, demonstrating a distinct change in scattering intensity at low Q values. In the cases of ratios 10:1, 5:1, 2:1, and 1:1, the polymer component greatly surpasses the colistin component in abundance. Notably, it is only when reaching a ratio of 1:1 that the formation of C3Ms becomes evident. This observation confirms the theoretical prediction that C3Ms exhibit a relatively narrow composition window, predominantly near a mixing fraction of 1:1. Furthermore, as we approach a charge balance, i.e., closer to the 1:1 ratio, an increase in scattering intensity is observed at low Q values. This suggests the presence of clusters formed during the complexation process, with the size of these clusters growing as more C3Ms are formed, particularly when nearing the 1:1 ratio.

In contrast, for the mixing ratios of 1:2, 1:5, 1:10, 1:20, and 1:35, colistin is present in excess compared to the diblock copolymer. For all of these ratios, the scattering curves show the formation of core-shell coacervates with large-scale aggregations occurring in the low Q-region.

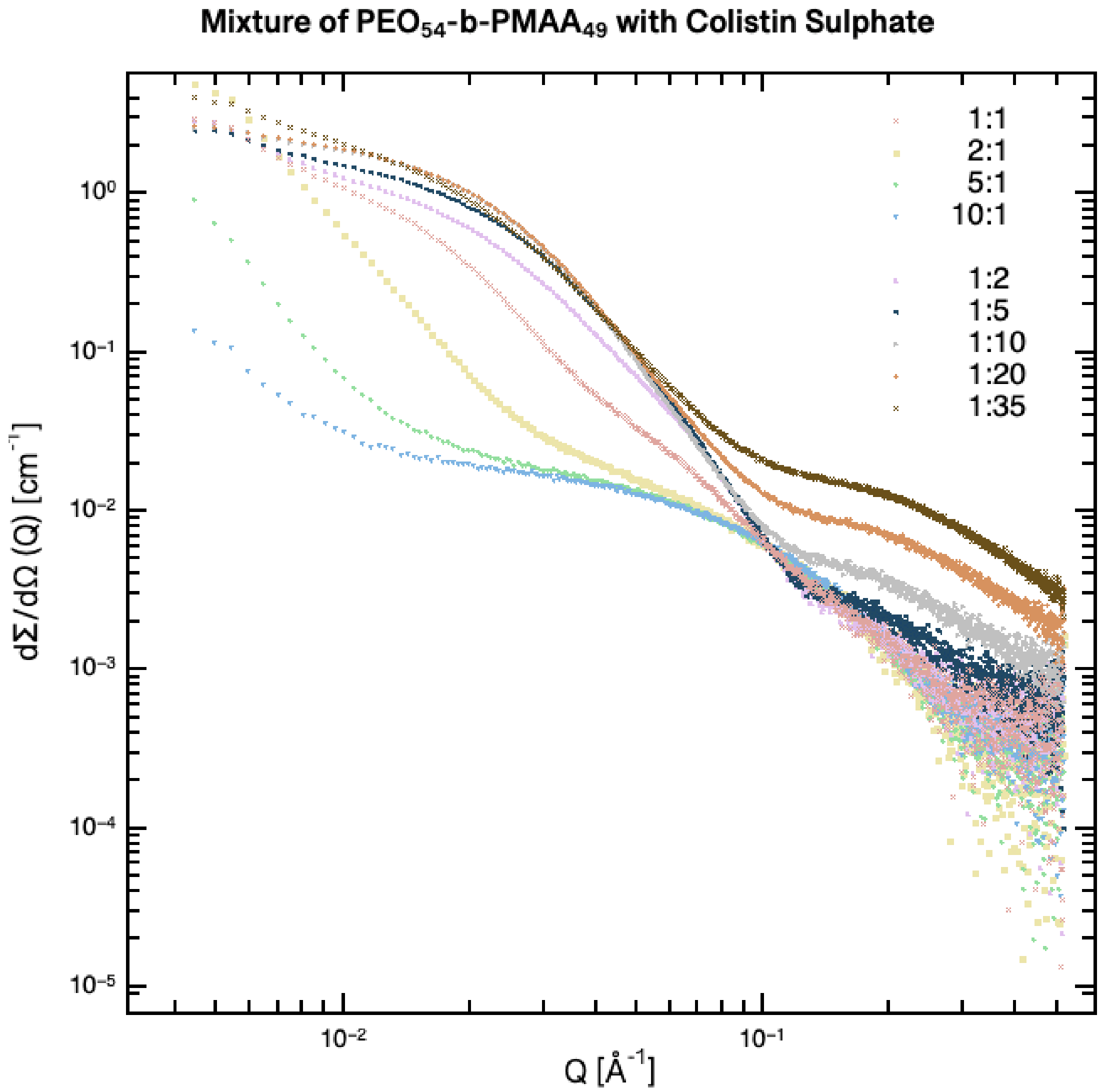

Figure 28. SAXS profiles of mixture between Colistin and PEO-b-PMAA at different polymer : colistin compositions.

4.4 Drug release studies of the formed nanocomplexes

In order to examine the pH-dependent drug release of Colistin and the colloidal stability of the coacervate micelles, it was intended to investigate buffer solutions with varying pH levels. Initially, citrate buffer (pH 5.5, 50 mM) and Tris buffer (pH 7.4, 50 mM) were prepared for this purpose. However, due to time constraints, drug release studies using these buffer solutions could not be conducted. Throughout this study, only PBS (pH 7.4, 10 mM) was utilized to assess the stability of the micelles.

Based on the analysis performed on the scattering curves obtained from the Colistin-PEO-b-PMAA complexation, a specific mixing ratio of 1:1 was chosen for further investigations. Section 4.3 demonstrated that this particular ratio could generate coacervate micelles encapsulating Colistin, as well as larger aggregations of these micelles. To assess the physical stability of the complexes dissolved in PBS, a 48-hour testing period was conducted (Figure 29). The initial sample, taken prior to the drug release studies, is represented by the blue scattering curve, reflecting the observations presented in Section 4.3 regarding the Colistin-PEO-b-PMAA complexation. Excellent stability of the complexes was observed for up to 5 hours, with no noticeable changes in the scattering curve. However, changes in the scattering curves were observed in samples taken at 12 hours, 24 hours, and 34 hours. At lower Q-values, these scattering curves resembled those obtained from pure polymer and pure Colistin, while minimal alterations were observed at higher Q-values. These data indicate that something occurred between the 5-hour and 12-hour sampling intervals, where it is evident that Colistin has been released and the complexes have disassembled into free chains. For future investigations, it would be of interest to collect additional samples within this timeframe to gain a more comprehensive understanding of the release kinetics.

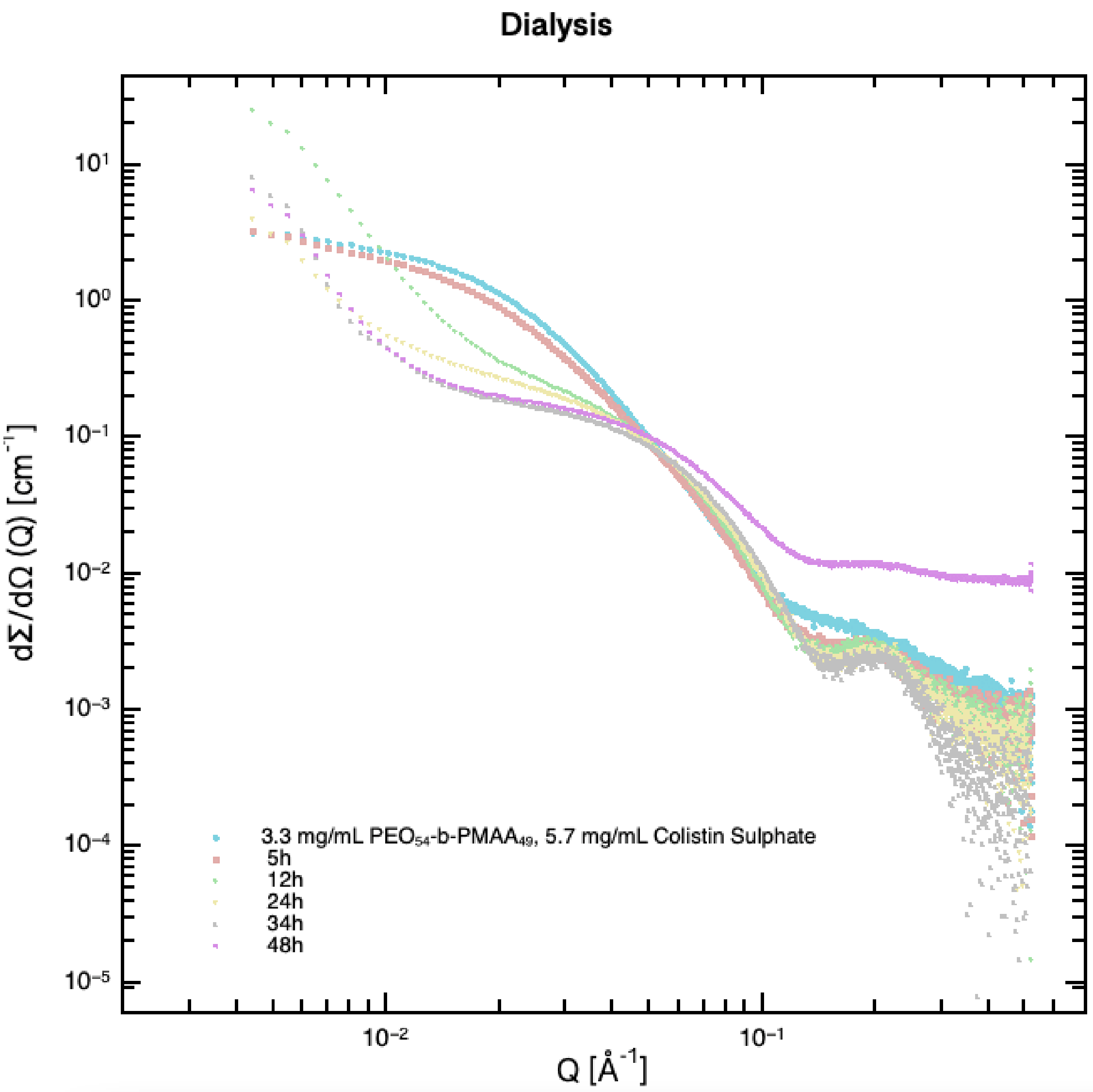

Figure 29. SAXS profile of a 1:1 mixing ratio of polymer to colistin, with concentrations of 3.3 mg/mL and 5.7 mg/mL, respectively. This graph serves to illustrate the physical stability of the coacervate complexes following incubation in phosphate-buffered saline (PBS). Samples were extracted at various time points, specifically after 5 hours, 12 hours, 24 hours, 34 hours, and 48 hours, enabling an examination of the temporal evolution of the coacervate complexes.

4.5 In vitro antimicrobial activity of nanocomplexes against *E. Coli* and *P. Aeruginosa*

As mentioned early in the thesis, Colistin has demonstrated rapid bactericidal activity in vitro against various Gram-negative multidrug-resistant (MDR) isolates, including Klebsiella Pneumoniae, Acinetobacter baumannii, and Pseudomonas aeruginosa. Despite its efficacy in clinical settings, subsequent studies reported severe toxicity associated with the use of Colistin as a therapeutic option. The reduction of toxicity and the fact that Colistin serves as a last-resort antibiotic motivated the focus of this thesis, which aimed to encapsulate Colistin in order to reduce its positive charges and, consequently, its toxicity.

Moving forward in this section, we aim to present the bacterial killing effect of Colistin against two different pathogenic bacterial strains: Escherichia coli ATCC 25922 and Pseudomonas aeruginosa H102 Canada (wild type). By demonstrating that the antimicrobial effect of Colistin remains intact even after encapsulation, we provide evidence supporting the potential of nanocomplexes to mitigate its toxicity. To assess the in vitro antimicrobial activity of the nanocomplexes, we employed the spot plating technique previously described in Section 3.4.1.

First, we conducted a simple investigation to determine the antimicrobial activity of the nanocomplexes. Figure 30 displays the agar plating results for various nanocomplexes prepared at concentrations of 2.8, 5.7, and 11.3 mg/mL, along with pure colistin and pure polymer at concentrations of 2.8 mg/mL and 3.3 mg/mL, respectively. In Figure 30, we also did a test on the Gram-positive bacteria *Staph. Aureus* to show that Colistin has no antimicrobial activity against Gram-positive bacteria. It was evident that the pure polymer did not exhibit any antimicrobial activity. However, both pure colistin and the nanocomplexes demonstrated a pronounced killing effect on both *E. Coli* and *P. aeruginosa*.

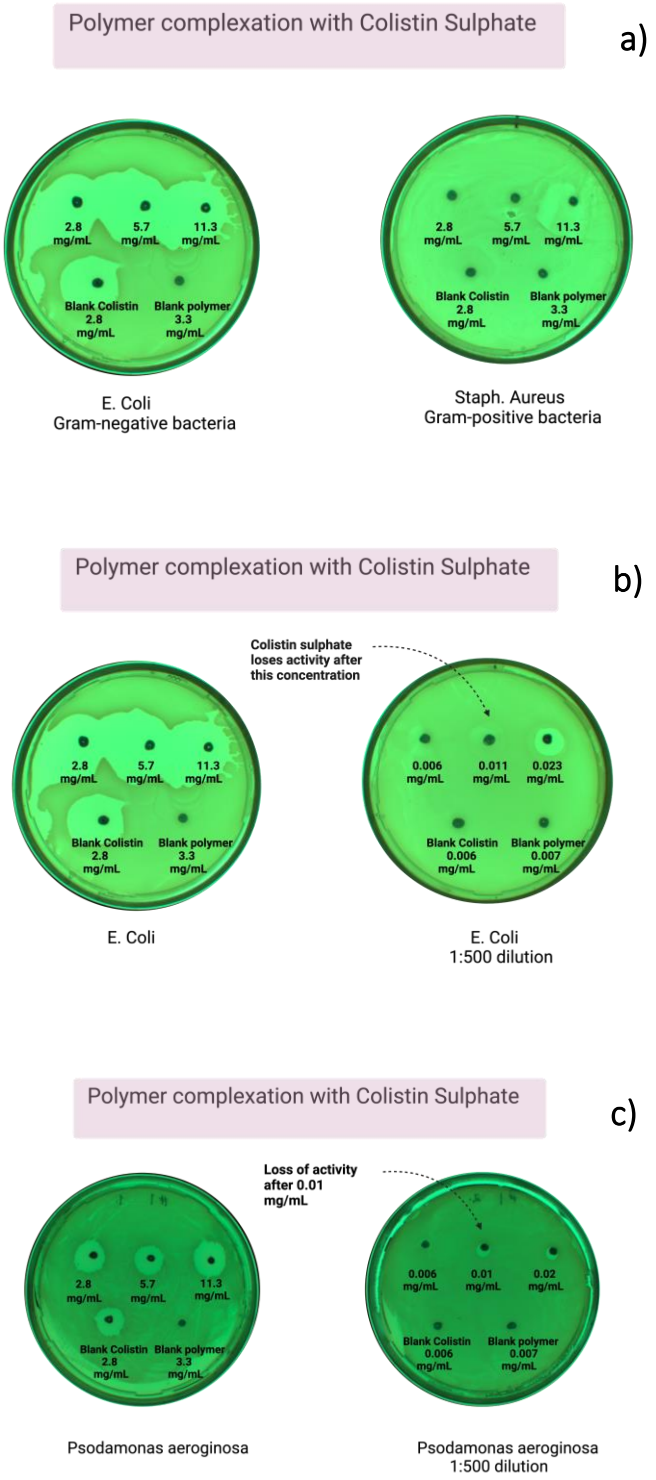

Figure 30. nanocomplexes of colistin and PEO-b-PMAA were evaluated against E. coli and P. aeruginosa at concentrations of 11.3, 5.7, and 2.8 mg/mL. Condition a) represented the bacterial strain E. coli, including the Gram-positive bacteria Staph. aureus, demonstrating the absence of antimicrobial effect of colistin on gram-positive bacteria. Dilutions (conditions b) and c)) revealed that the nanocomplexes lost their activity at 0.1 mg/mL for both E. coli and P. aeruginosa.

In order to obtain more precise results, we decided to further dilute the samples. Upon dilution, we observed that the nanocomplex at a concentration of 0.11 mg/mL lost its antimicrobial activity against the E. Coli bacterial strain. Similarly, for P. aeruginosa, the antimicrobial activity was lost at a concentration of 0.1 mg/mL. These findings are visually represented in Figure 30.

4.6 Minimum inhibitory concentration

To evaluate the antibacterial efficacy of the colistin nanoparticles, we measured the minimum inhibitory concentration (MIC) of the nanoparticles against the two isolates of E. coli and P. aeruginosa. Figure 31 illustrates the number of bacterial colonies counted for E. coli and P. aeruginosa, as determined using the method described in Section 3.4.1. In the MIC assay, we compared the activity of free colistin with that of co-assembled colistin with a polymer into nanocomplexes. To assess any solvent-related effects, the bacterial culture was diluted with both water and PBS.

The MIC concentration was determined as the lowest concentration at which no visible growth was observed after 24 hours of incubation. The nanocomplexes containing colistin exhibited MIC values of 0.009 mg/mL for E. coli and 0.018 mg/mL for P. aeruginosa, as depicted in Figure 2. Additionally, for E. coli, this finding was confirmed by spotting the samples of the MIC on agar plates, which revealed a matching MIC value of 0.009 mg/mL. We compared these results to the result that we found in Section 4.5 by just spotting the nanocomplexes samples at the agar plating with the bacterial strains.

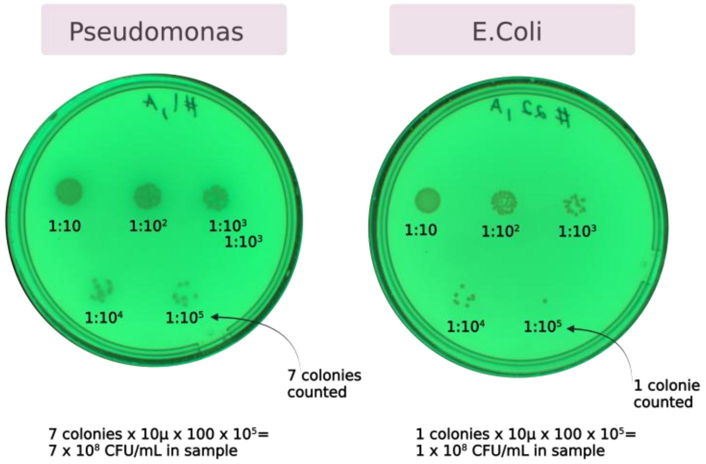

Figure 31. The amount of bacterial numbers were calculated by 1:500 dilution to reach the bacterial inculum ranging between $2 - 8 \cdot 10\, cfu\ /mL$*. For Pseudomonas and E. Coli it was shown to have bacterial number of n* $7 \cdot 10^8\, cfu\ /mL$ *and n* $1 \cdot 10^8\, cfu\ /mL$ *in the sample respectively.*

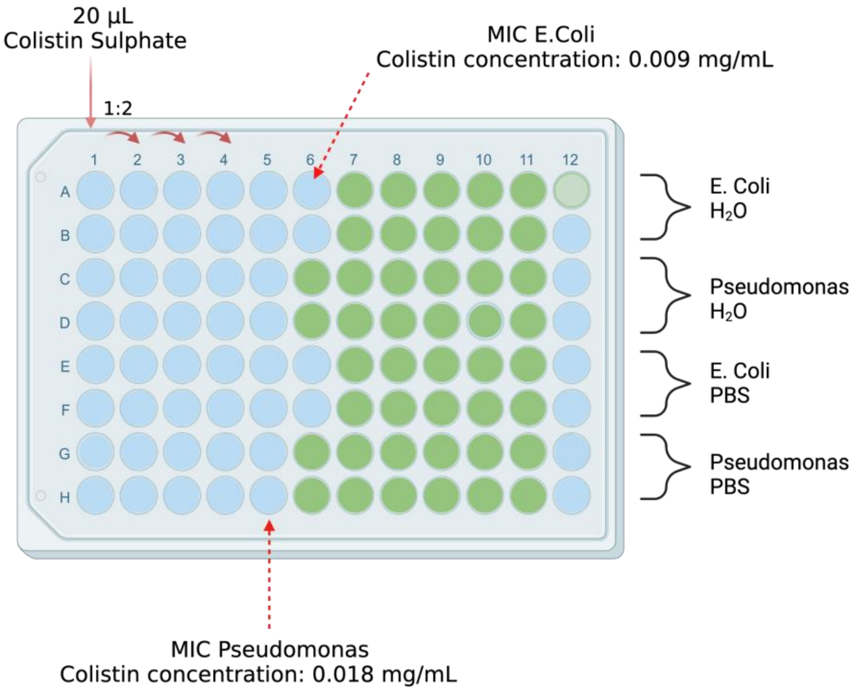

Figure 32. The figure shows that the minimum inhibitory concentration (MIC) of the nanocomplexes against E. coli was 0.009 mg/mL, while for P. aeruginosa it was 0.018 mg/mL. We examined the MIC using both water and PBS as dilution solvents, but observed no significant difference in their effects.

.As discussed in the preceding section, the experimental results clearly indicate that the nanocomplex exhibited a loss of activity at a concentration of 0.011 mg/mL for the E. Coli strain, as illustrated in Figure 30. This finding is further supported by the determination of the minimum inhibitory concentration (MIC), which yields a value of 0.009 mg/mL, which can be approximated to 0.01 mg/mL. Similarly, for P. Aeruginosa, the data presented in Figure 30(c) indicates a loss of antimicrobial activity at 0.01 mg/mL, while Figure 32 demonstrates that it loses its antimicrobial effectiveness at a slightly higher concentration of 0.018 mg/mL, which can be rounded up to 0.02 mg/mL. Although there exist slight variations, these differences are considered to be minor. The difference is shown in Figure 33.

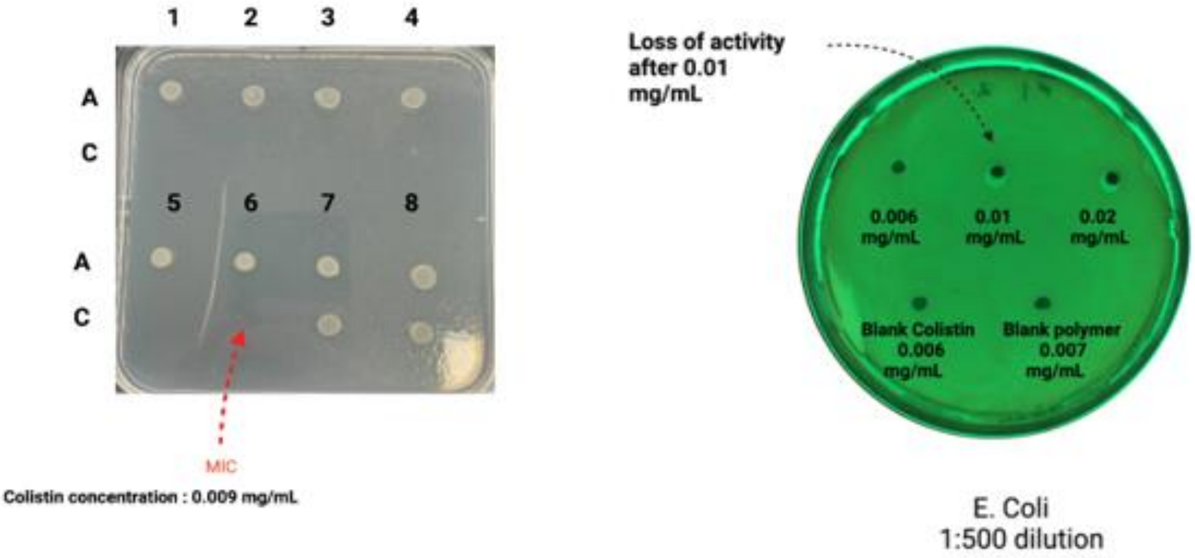

Figure 33. This figure presents a comparison between the spotting techniques used for determining the minimum inhibitory concentration (MIC) and the direct spotting of nanocomplexes onto the bacterial strain of E. Coli. Notably, both approaches reveal that the antimicrobial activity of the nanocomplexes ceases at a concentration of 0.01 mg/mL.

5 Conclusion and outlook

The failure of conventional antibiotics to effectively treat infected patients is a growing concern due to the emergence of antibiotic-resistant bacteria worldwide. Consequently, there is an urgent need for the development and testing of new approaches. Among the various drug delivery systems explored, complex coacervate core micelles have garnered significant interest. Additionally, due to its polycationic nature, Colistin can readily form complexes with oppositely charged polyanions. In our study, we employed a pH-sensitive double-hydrophilic block copolymer (PEO-b-PMAA), where the PEO shell acts as a protective corona around the core, safeguarding it from enzymatic degradation.

The primary objective of this thesis was to create innovative nanomedicines based on the peptide colistin. This involved a comprehensive investigation of the phase diagram of colistin/PEO-b-PMAA mixtures, considering variables such as pH, charge ratio, and total concentration. Specifically, our aim was to identify optimal conditions that would lead to the formation of stable core-shell colistin-polymer complexes. While several parameters were not examined in this research, two particular factors were taken into consideration: the charge ratio and the total concentration. The structural properties were characterized using SAXS, and two analytical models were employed to extract information from the scattering data obtained for pure polymer, pure colistin, and their nanocomplexes. The analysis revealed that the pure samples existed mainly as free chains, albeit with some evidence of aggregation. Furthermore, we closely monitored the formation process of polyelectrolyte coacervates by varying the concentration and charge ratio of colistin and PEO-b-PMAA. Our findings demonstrated that a 1:1 mixing ratio yielded coacervate micelles.

The other objective of this study was to evaluate the antimicrobial activity of the nanocomplexes, which was successfully demonstrated against both E. coli and P. aeruginosa. It was observed that the complexation of colistin inhibited its activity, yet it effectively screened the charges, thereby reducing toxicity. Naturally, further investigations are required to explore the particle shape and other crucial parameters that can influence the complexation process.

6 Bibliography

1. Mahlapuu M, Håkansson J, Ringstad L, Björn C. Antimicrobial peptides: An emerging category of therapeutic agents. Front Cell Infect Microbiol. 2016;6(DEC):194-.

2. Moravej H, Moravej Z, Yazdanparast M, Heiat M, Mirhosseini A, Moosazadeh Moghaddam M, et al. Antimicrobial Peptides: Features, Action, and Their Resistance Mechanisms in Bacteria. Microb Drug Resist. 2018;24(6):747-67.

3. Falagas ME, Kyriakidou M, Voulgaris GL, Vokos F, Politi S, Kechagias KS. Clinical use of intravenous polymyxin B for the treatment of patients with multidrug-resistant Gram-negative bacterial infections: An evaluation of the current evidence. J Glob Antimicrob Resist. 2021;24:342-59.

4. Koch-Weser J, Sidel VW, Federman EB, Kanarek P, Finer DC, Eaton AE. Adverse effects of sodium colistimethate. Manifestations and specific reaction rates during 317 courses of therapy. Ann Intern Med. 1970;72(6):857.

5. Nang SC, Azad MAK, Velkov T, Zhou QT, Li J. Rescuing the Last-Line Polymyxins: Achievements and Challenges. Pharmacol Rev. 2021;73(2):679-728.

6. Tran TB, Wang J, Doi Y, Velkov T, Bergen PJ, Li J. Novel Polymyxin Combination With Antineoplastic Mitotane Improved the Bacterial Killing Against Polymyxin-Resistant Multidrug-Resistant Gram-Negative Pathogens. Front Microbiol. 2018;9:721-.

7. Zhao M, Cao Y-R, Guo B-N, Wu X-J, Li J, Zhang J. LC-MS/MS determination of colistin in Mueller-Hinton broth for in vitro pharmacodynamic studies. J Antibiot (Tokyo). 2014;67(12):825-9.

8. Terreni M, Taccani M, Pregnolato M. New antibiotics for multidrug-resistant bacterial strains: Latest research developments and future perspectives. Molecules (Basel, Switzerland). 2021;26(9):2671.

9. Lewis K. Platforms for antibiotic discovery. Nat Rev Drug Discov. 2013;12(5):371-87.

10. Antibiotics Currently in Global Clinical Development [Internet]. 2020 [cited March 9, 2021]. Available from: https://www.pewtrusts.org/en/research-and-analysis/data-visualizations/2014/antibiotics-currently-in-clinical-development.

11. Iudin D, Zashikhina N, Demyanova E, Korzhikov-Vlakh V, Shcherbakova E, Boroznjak R, et al. Polypeptide Self-Assembled Nanoparticles as Delivery Systems for Polymyxins B and E. Pharmaceutics. 2020;12(9):868.

12. Weerakoon D, Petrov K, Pedebos C, Khalid S. Polymyxin B1 within the E. coli cell envelope: insights from molecular dynamics simulations. Biophysical reviews. 2021.

13. Velkov T, Roberts KD, Nation RL, Thompson PE, Li J. Pharmacology of polymyxins: new insights into an 'old class of antibiotics. Future Microbiol. 2013;8(6):711-24.

14. Qi B, Gijsen M, Van Brantegem P, De Vocht T, Deferm N, Abza GB, et al. Quantitative determination of colistin A/B and colistin methanesulfonate in biological samples using hydrophilic interaction chromatography tandem mass spectrometry. Drug Test Anal. 2020;12(8):1183-95.

15. Zabidi MS, Abu Bakar R, Musa N, Mustafa S, Wan Yusuf WN. Population Pharmacokinetics of Colistin Methanesulfonate Sodium and Colistin in Critically Ill Patients: A Systematic Review. Pharmaceuticals (Basel, Switzerland). 2021;14(9):903.

16. Biswas S, Brunel J-M, Dubus J-C, Reynaud-Gaubert M, Rolain J-M. Colistin: an update on the antibiotic of the 21st century. Expert Rev Anti Infect Ther. 2012;10(8):917-34.

17. Michalopoulos AS, Falagas ME. Colistin: recent data on pharmacodynamics properties and clinical efficacy in critically ill patients. Ann Intensive Care. 2011;1(1):1-6.

18. Bruslind L. General Microbiology. 2019:178.

19. Epand RM, Walker C, Epand RF, Magarvey NA. Molecular mechanisms of membrane targeting antibiotics. Biochimica et biophysica acta Biomembranes. 2016;1858(5):980-7.

20. Sabnis A, Hagart KL, Klöckner A, Becce M, Evans LE, Furniss RCD, et al. Colistin kills bacteria by targeting lipopolysaccharide in the cytoplasmic membrane. Elife. 2021;10.

21. Abouelmagd SA, Abd Ellah NH, Amen O, Abdelmoez A, Mohamed NG. Self-assembled tannic acid complexes for pH-responsive delivery of antibiotics: Role of drug-carrier interactions. Int J Pharm. 2019;562:76-85.

22. Moubareck CA. Polymyxins and Bacterial Membranes: A Review of Antibacterial Activity and Mechanisms of Resistance. Membranes (Basel). 2020;10(8):181.

23. Liu Y-H, Kuo S-C, Yao B-Y, Fang Z-S, Lee Y-T, Chang Y-C, et al. Colistin nanoparticle assembly by coacervate complexation with polyanionic peptides for treating drug-resistant gram-negative bacteria. Acta Biomater. 2018;82:133-42.

24. Lim LM, Ly N, Anderson D, Yang JC, Macander L, Jarkowski Iii A, et al. Resurgence of Colistin: A Review of Resistance, Toxicity, Pharmacodynamics, and Dosing. Pharmacotherapy. 2010;30(12):1279-91.

25. Wagenlehner F, Lucenteforte E, Pea F, Soriano A, Tavoschi L, Steele VR, et al. Systematic review on estimated rates of nephrotoxicity and neurotoxicity in patients treated with polymyxins. Clin Microbiol Infect. 2021;27(5):671-86.

26. Dubashynskaya NV, Skorik YA. Polymyxin Delivery Systems: Recent Advances and Challenges. Pharmaceuticals (Basel). 2020;13(5):83.

27. Sanchez A, Mejia SP, Orozco J. Recent Advances in Polymeric Nanoparticle-Encapsulated Drugs against Intracellular Infections. Molecules. 2020;25(16):3760.

28. Zhu C, Schneider EK, Wang J, Kempe K, Wilson P, Velkov T, et al. A traceless reversible polymeric colistin prodrug to combat multidrug-resistant (MDR) gram-negative bacteria. J Control Release. 2017;259:83-91.

29. Dubashynskaya N, Raik S, Dubrovskii YA, Demyanova E, Shcherbakova ES, Poshina DN, et al. Hyaluronan/Diethylaminoethyl Chitosan Polyelectrolyte Complexes as Carriers for Improved Colistin Delivery. International journal of molecular sciences. 2021;22(16):8381.

30. Le H, Karakasyan C, Jouenne T, Le Cerf D, De E. Application of Polymeric Nanocarriers for Enhancing the Bioavailability of Antibiotics at the Target Site and Overcoming Antimicrobial Resistance. Applied sciences. 2021;11(22):10695.

31. Zhang L, Chan JM, Gu FX, Rhee J-W, Wang AZ, Radovic-Moreno AF, et al. Self-Assembled Lipid−Polymer Hybrid Nanoparticles: A Robust Drug Delivery Platform. ACS Nano. 2008;2(8):1696-702.

32. Karayianni M, Pispas S. Block copolymer solution self-assembly: Recent advances, emerging trends, and applications. Journal of polymer science (2020). 2021;59(17):1874-98.

33. Rikken RSM, Engelkamp H, Nolte RJM, Maan JC, van Hest JCM, Wilson DA, et al. Shaping polymersomes into predictable morphologies via out-of-equilibrium self-assembly. Nat Commun. 2016;7(1):12606-.

34. Reboul J, Nugay T, Anik N, Cottet H, Ponsinet V, In M, et al. Synthesis of double hydrophilic block copolymers and induced assembly with oligochitosan for the preparation of polyion complex micelles. Soft matter. 2011;7(12):5836-46.

35. Boudier A, Aubert-Pouëssel A, Gérardin C, Devoisselle J-M, Bégu S. pH-sensitive double-hydrophilic block copolymer micelles for biological applications. Int J Pharm. 2009;379(2):212-7.

36. El Jundi A, Buwalda SJ, Bakkour Y, Garric X, Nottelet B. Double hydrophilic block copolymers self-assemblies in biomedical applications. Advances in colloid and interface science. 2020;283:102213-.

37. Harada A, Kataoka K. Formation of Polyion Complex Micelles in an Aqueous Milieu from a Pair of Oppositely-Charged Block Copolymers with Poly(ethylene glycol) Segments. Macromolecules. 1995;28(15):5294-9.

38. Neitzel AE, De Hoe GX, Tirrell MV. Expanding the structural diversity of polyelectrolyte complexes and polyzwitterions. Current opinion in solid state & materials science. 2021;25(2):100897.

39. Herzog-Arbeitman A. Polyelectrolyte Complexation: Entropy, Medicine, and the Beginning of Life. Reinvention: an International Journal of Undergraduate Research. 2019;12(2).

40. Zhou L, Shi H, Li Z, He C. Recent Advances in Complex Coacervation Design from Macromolecular Assemblies and Emerging Applications. Macromol Rapid Commun. 2020;41(21):e2000149-n/a.

41. Abbas M, Lipinski WP, Wang J, Spruijt E. Peptide-based coacervates as biomimetic protocells. Chem Soc Rev. 2021;50(6):3690-705.

42. van der Burgh S, de Keizer A, Cohen Stuart MA. Complex Coacervation Core Micelles. Colloidal Stability and Aggregation Mechanism. Langmuir. 2004;20(4):1073-84.

43. Voets IK, van der Burgh S, Farago B, Fokkink R, Kovacevic D, Hellweg T, et al. Electrostatically Driven Coassembly of a Diblock Copolymer and an Oppositely Charged Homopolymer in Aqueous Solutions. Macromolecules. 2007;40(23):8476-82.

44. van der Kooij HM, Spruijt E, Voets IK, Fokkink R, Cohen Stuart MA, van der Gucht J. On the Stability and Morphology of Complex Coacervate Core Micelles: From Spherical to Wormlike Micelles. Langmuir. 2012;28(40):14180-91.

45. Luo Y-L, Yu W, Xu F. pH-responsive PMAA-b-PEG-b-PMAA triblock copolymer micelles for prednisone drug release and release kinetics. Polymer bulletin (Berlin, Germany). 2012;69(5):597-620.

46. Molina E, Warnant Jrm, Mathonnat Ml, Bathfield Ml, In M, Laurencin D, et al. Drug–Polymer Electrostatic Complexes as New Structuring Agents for the Formation of Drug-Loaded Ordered Mesoporous Silica. Langmuir. 2015;31(47):12839-44.

47. Aloi A, Guibert C, Olijve LLC, Voets IK. Morphological evolution of complex coacervate core micelles revealed by iPAINT microscopy. Polymer (Guilford). 2016;107:450-5.

48. Amann M, Diget JS, Lyngsø J, Pedersen JS, Narayanan T, Lund R. Kinetic Pathways for Polyelectrolyte Coacervate Micelle Formation Revealed by Time-Resolved Synchrotron SAXS. Macromolecules. 2019;52(21):8227-37.

49. Marras AE, Ting JM, Stevens KC, Tirrell MV. Advances in the Structural Design of Polyelectrolyte Complex Micelles. J Phys Chem B. 2021;125(26):7076-89.

50. Mitchell MJ, Billingsley MM, Haley RM, Wechsler ME, Peppas NA, Langer R. Engineering precision nanoparticles for drug delivery. Nat Rev Drug Discov. 2021;20(2):101-24.

51. Sui Z, Jaber JA, Schlenoff JB. Polyelectrolyte Complexes with pH-Tunable Solubility. Macromolecules. 2006;39(23):8145-52.

52. Chen S, Zhang P, Wang Z-G. Complexation between Oppositely Charged Polyelectrolytes in Dilute Solution: Effects of Charge Asymmetry. Macromolecules. 2022;55(10):3898-909.

53. Marras AE, Vieregg JR, Tirrell MV. Assembly and Characterization of Polyelectrolyte Complex Micelles. J Vis Exp. 2020;157(157).

54. Marras AE, Campagna TR, Vieregg JR, Tirrell MV. Physical Property Scaling Relationships for Polyelectrolyte Complex Micelles. Macromolecules. 2021;54(13):6585-94.

55. Mebarek N, Aubert-Pouëssel A, Gérardin C, Vicente R, Devoisselle J-M, Bégu S. Polymeric micelles based on poly(methacrylic acid) block-containing copolymers with different membrane destabilizing properties for cellular drug delivery. Int J Pharm. 2013;454(2):611-20.

56. Uchman M, Štěpánek M, Prévost S, Angelov B, Bednár J, Appavou M-S, et al. Coassembly of Poly(ethylene oxide)-block-poly(methacrylic acid) and N-Dodecylpyridinium Chloride in Aqueous Solutions Leading to Ordered Micellar Assemblies within Copolymer Aggregates. Macromolecules. 2012;45(16):6471-80.

57. Insua I, Zizmare L, Peacock AFA, Krachler AM, Fernandez-Trillo F. Polymyxin B containing polyion complex (PIC) nanoparticles: Improving the antimicrobial activity by tailoring the degree of polymerisation of the inert component. Sci Rep. 2017;7(1):9396-10.

58. Zueva OS, Rukhlov VS, Zuev YF. Morphology of Ionic Micelles as Studied by Numerical Solution of the Poisson Equation. ACS Omega. 2022;7(7):6174-83.

59. Ouyang W, Han J, Wang W. Enabling electrical biomolecular detection in high ionic concentrations and enhancement of the detection limit thereof by coupling a nanofluidic crystal with reconfigurable ion concentration polarization. Lab Chip. 2017;17(22):3772-84.

60. Marciel AB, Srivastava S, Ting JM, Tirrell MV. SAXS methods for investigating macromolecular and self-assembled polyelectrolyte complexes. Methods Enzymol. 2021;646:223-59.

61. Singh HSY. The SAXS Guide. Austria: Anton Paar GmbH; 2013. 121 p.

62. Li Y, Jin M, Shao S, Huang W, Yang F, Chen W, et al. Small-sized polymeric micelles incorporating docetaxel suppress distant metastases in the clinically-relevant 4T1 mouse breast cancer model. BMC Cancer. 2014;14(1):329-.

63. Brumberger H. Modern aspects of small-angle scattering. Dordrecht: Kluwer; 1995.

64. Stensgaard Diget J, Lund R, Nyström B, Wintgens V, Amiel C, Wimmer R, et al. Self-assembled nanoparticles based on cyclodextrin-modified pullulan: Synthesis, and structural characterization using SAXS. Carbohydr Polym. 2019;213:403-10.

65. Sing CE. Recent progress in the science of complex coacervations. Soft matter. 2020(12):33.

7 Appendix

Table 5. Definitions and units of parameters used in analytical models describing coacervate micelles.

Parameter	Definition
Mp	Molecular weight [g/mol]
Rg	Radius of Gyration [Å]
dp	Density polymer [g/cm^2]
RhoP0	Scattering length density solvent [cm^{-2}]
RhoP	Scattering length density polymer [cm^{-2}]
RhoCol	Scattering length density Colistin [cm^{-2}]
df	Fractal dimension
C	Cluster prefactor
xi	Fractal cluster size
fpfree	Fraction of free chains that is BCP: 1 or 0
fcfree	Fraction of free chains that of colistin
expo	Exponent cluster 2 default
xiC	Cluster size
f0	Fraction of solvent
f0ped	Fraction of solvent
Sigma	Outer roughness
Mcol	MW Colistin
Rp	Radius of particles [Å]
P	Aggregration number

7.1 Structural characterisation of PEO_{54}-b-$PMAA_{49}$

Table 6. *All parameters used for the Beaucage model to fit the scattering data at different concentrations.*

	0.5 mM	0.4 mM	0.3 mM	0.1 mM
Mp	6600	6600	6600	6600
Rg	17.981262	20.0192599	21.8051162	21.4103863
dp	1.33	1.33	1.33	1.33
RhoP0	1.096e+11	1.096e+11	1.096e+11	1.096e+11
RhoSolv	9.39e+10	9.39e+10	9.39e+10	9.39e+10
A2	0	0	0.009	0
xi	500	550	500	500
expo	1.3	1.9	2	1.5
bcg	5e-05	3e-05	2e-05	5.2e-05
C	0.55	1.5	0.2	0.02
dsol	1	1	1	1

7.2 Structural characterisation of Colistin

Table 7. All parameters used for the Beaucage model to fit the scattering data at different concentrations.

	10 mM	8 mM	2 mM
Mp	1155	1155	1155
Rg	6.22031231	6.19215429	5.98903258
df	2.1	2.1	2.1
dp	1.33	1.33	1.33
RhoP0	1.096e+11	1.096e+11	1.096e+11
RhoSolv	9.39e+10	9.39e+10	9.39e+10
A2	0	0.0019	0
xi	1000	1000	1000
expo	2	1.9	2
bcg	0	0	0
C	10	1.5	2.5
dsol	1	1	1

7.3 Calculation for Mixture of PEO$_{54}$-b-PMAA$_{49}$ with Colistin

Table 8. Calculations for the charge ratio. Different polymer : colistin compositions were used, and these are only calculation for the scattering curve shown in Figure 28, Section 4.3.

Polymer konsentrasjon (mg/mL)	Masse (g)	MW (g/mol)	n (mol)	Number of molecules (48,8)	Number of charges
3,3	0,0033	6600	5,00E-07	3,01E+17	1,47E+19
Colistin (mg/mL)	MW (g/mol)	Mass (g)	n(mol)		
3,3	1155	0,0033	2,85714E-06		
1.					
	Mass (g)	Mass (mg)	Buffer (mL)	Consentrasjon (mg/mL)	
Standard polymer	0,0297	23,1	7	3,3	
Polymer : Colistin	n_colistin (mol)	m_colistin (g)	m_colistin (mg)	consentrasjon colistin (mg/mL)	
1:1	5,00E-07	0,000578	0,5775	0,58	
2:1	2,50E-07	0,000289	0,2888	0,29	
5:1	1,00E-07	0,000116	0,1155	0,12	
10:1	5,00E-08	0,000058	0,0578	0,06	
1:2	1,00E-06	0,001155	1,1550	1,16	
1:5	2,50E-06	0,002888	2,8875	2,89	
1:10	5,00E-06	0,005775	5,7750	5,78	
1:20	1,00E-05	0,011550	11,5500	11,55	
1:35	1,75E-05	0,020213	20,2125	20,2125	